GDAŃSK UNIVERSITY OF TECHNOLOGY
FACULTY OF CHEMISTRY

The author of the PhD dissertation: Sapajan Ibragimov
Scientific discipline: Chemical Sciences

DOCTORAL DISSERTATION

Title of PhD dissertation: “Isomers of iron(III) oxides and their application in the catalytic synthesis of hydrogen from ammonia. Studies using quantum chemical methods”.

Title of PhD dissertation (in Polish): “Izomery tlenków żelaza (III) i ich zastosowanie w katalityczcznej syntezie wodoru z amoniaku. Badania metodami chemii kwantowej”.

Supervisor *signature*
Dr hab. Maciej Bobrowski

Gdańsk, 2026

GDAŃSK UNIVERSITY OF TECHNOLOGY
FACULTY OF CHEMISTRY

STATEMENT

The author of the PhD dissertation: Sapajan Ibragimov

I, the undersigned, agree/~~do not agree~~* that my PhD dissertation entitled: "Isomers of iron(III) oxides and their application in the catalytic synthesis of hydrogen from ammonia. Studies using quantum chemical methods" may be used for scientific or didactic purposes.[1]

Gdańsk,..... .....

signature of the PhD student

Aware of criminal liability for violations of the Act of 4th February 1994 on Copyright and Related Rights (Journal of Laws 2006, No. 90, item 631) and disciplinary actions set out in the Law on Higher Education (Journal of Laws 2012, item 572 with later amendments),[2] as well as civil liability, I declare, that the submitted PhD dissertation is my own work.

I declare, that the submitted PhD dissertation is my own work performed under and in cooperation with the supervision of dr hab. Maciej Bobrowski, ~~the second supervision of <name of the second supervisor>, the auxiliary supervision of <name of the auxiliary supervisor>, the cosupervision of <name of the cosupervisor>~~*.

This submitted PhD dissertation has never before been the basis of an official procedure associated with the awarding of a PhD degree.

All the information contained in the above thesis which is derived from written and electronic sources is documented in a list of relevant literature in accordance with art. 34 of the Copyright and Related Rights Act.

I confirm that this PhD dissertation is identical to the attached electronic version.

Gdańsk,..... .....

signature of the PhD student

I, the undersigned, agree/~~do not agree~~* to include an electronic version of the above PhD dissertation in the open, institutional, digital repository of Gdańsk University of Technology, Pomeranian Digital Library, and for it to be submitted to the processes of verification and protection against misappropriation of authorship.

Gdańsk,..... .....

signature of the PhD student

*) delete where appropriate.

[1] Decree of Rector of Gdansk University of Technology No. 34/2009 of 9th November 2009, TUG archive instruction addendum No. 8.

[2] Act of 27th July 2005, Law on Higher Education: Chapter 7, Criminal responsibility of PhD students, Article 226.

GDAŃSK UNIVERSITY OF TECHNOLOGY
FACULTY OF CHEMISTRY

DESCRIPTION OF DOCTORAL DISSERTATION

The Author of the PhD dissertation: Sapajan Ibragimov

Title of PhD dissertation: “Isomers of iron(III) oxides and their application in the catalytic synthesis of hydrogen from ammonia. Studies using quantum chemical methods”

Title of PhD dissertation in Polish: “Izomery tlenków żelaza (III) i ich zastosowanie w katalityczcznej syntezie wodoru z amoniaku. Badania metodami chemii kwantowej”

Language of PhD dissertation: English

Supervision: dr hab. Maciej Bobrowski

~~**Second supervision***: <first name, surname >~~

~~**Auxiliary supervision***: <first name, surname >~~

~~**Cosupervision***: <first name, surname >~~

Date of doctoral defense:

Keywords of PhD dissertation in Polish: Teoria funkcjonału gęstości, tlenek żelaza, potencjał redoks, chemia kwantowa, dehydrogenacja, mechanizmy reakcji, katalizatory i kataliza

Keywords of PhD dissertation in English: Density Functional Theory, Iron oxide, Redox potential, Quantum chemistry, Dehydrogenation, Reaction mechanisms, Catalysts and Catalysis

Summary of PhD dissertation in Polish: Moja rozprawa doktorska koncentrowała się na systematycznych badaniach teoretycznych struktur (Fe2O3)n, gdzie n = 1–10, z wykorzystaniem metod chemii obliczeniowej. W tym kontekście, kompleksowa eksploracja strukturalna miała na celu identyfikację i charakterystykę izomerów niskoenergetycznych oraz ilościowe określenie zależnych od rozmiaru trendów stabilności; rygorystyczna analiza struktury elektronowej i właściwości magnetycznych, ze szczególnym uwzględnieniem roli stanu spinowego w określaniu konfiguracji stanu podstawowego i dostępnych rozmaitości reakcji; oraz badanie zachowania katalitycznego wybranych struktur tlenku Fe(III) (n = 1–4) w reakcji dehydrogenacji NH3.

Summary of PhD dissertation in English: My PhD dissertation focused on the systematic theoretical investigation of $(Fe_2O_3)_n$ structures where n=1-10, employing computational chemistry methods. In this context, comprehensive structural exploration aimed at identifying and characterising low-energy isomers and quantifying size-dependent trends in stability; a rigorous analysis of electronic structure and magnetic properties, with particular emphasis on the role of spin state in determining ground-state configurations and accessible reaction manifolds; and an investigation of the catalytic behaviour of selected Fe(III) oxide structures (n = 1–4) in the NH_3 dehydrogenation reaction were studied.

~~**Summary of PhD dissertation in language, in which it was written****: <summary, up to 1400 characters >~~

~~**Keywords of PhD dissertation in language, in which it was written****: <keywords>*~~

*) delete where appropriate.

**) applies to doctoral dissertations written in other languages, than Polish or English.

Abstract

This monograph investigates the spatial structure, electronic structure, and magnetic properties of iron(III) oxide molecules, together with their catalytic role in hydrogen production from ammonia decomposition for sustainable energy applications.

The first part of this work is concerned with the spin and spatial configurations of $(Fe_2O_3)_1$ and their redox properties. Iron(III) oxide is known to exist in multiple geometric configurations namely kite, spindle, and linear, each of which can, in principle, adopt a range of electronic arrangements, from ferromagnetic high-spin states to antiferromagnetic open-shell singlets. The present calculations reveal that highly open-shell configurations are energetically competitive, and that one-electron reduction or oxidation can alter both the spin state and the molecular geometry, in some cases inducing transformations between isomers. The standard one-electron reduction potentials computed against the Standard Hydrogen Electrode (SHE) were found to span the range −0.37 to −0.72V, depending on the isomer geometry, spin state, and level of theory. These values should be regarded as estimates obtained for the specific isomers and spin states examined; they do not represent a complete survey of all possible configurations of iron(III) oxide.

A principal conclusion emerging from the electronic structure study is that the spatial and electronic structure of iron(III) oxide is considerably more complex than has generally been assumed in the literature. The number of energetically plausible spatial configurations grows rapidly with increasing n in $(Fe_2O_3)_n$, and for each configuration there exist multiple spin states, including antiferromagnetic open-shell arrangements that are distinct from both the non-magnetic singlet and the

ferromagnetic high-spin states. It was not possible within the scope of this work to obtain a complete set of optimized structures for all configurations and all spin states at every value of n; the present results therefore represent a systematic but necessarily partial exploration. Also, computationally cheaper methods were found to lead to qualitatively incorrect conclusions about the relative stability of isomers, which indicates that reliable conclusions in this area require high-level quantum-chemical treatment, benchmark computations are needed. It must be noted that multi-configurational methods have not yet been applied to these systems, and it cannot be excluded that some states are strongly multi-configurational in character; this remains an open question for future work.

Given these limitations, the lowest-energy isomers identified for the most stable structures of $(Fe_2O_3)_n$ where n=1-4 obtained during my PhD study, were adopted as catalyst models for an exploratory study of ammonia decomposition. All catalytic calculations were carried out on high-spin ferromagnetic states of $(Fe_2O_3)_n$, since these emerged as low-energy configurations in the electronic structure part of the work, though it is acknowledged that other spin states may also be relevant. The reaction pathways and energetics were investigated using the SC-AFIR and DS-AFIR methods within the Global Reaction Route Mapping (GRRM) strategy, employing the B3LYP exchange-correlation functional.

For the $(Fe_2O_3)_n$ (n=1-4) models studied, NH_3 adsorption was found to occur at two-coordinated Fe sites for n = 1 and at three-coordinated Fe sites for n = 2–4, reflecting the coordination geometry of the specific isomers examined. The thermodynamic analysis indicates that NH_3 adsorption is favourable across the temperature range 0–1200K for the $(Fe_2O_3)_1$ model, while for the $(Fe_2O_3)_2$, $(Fe_2O_3)_3$, and $(Fe_2O_3)_4$ models it becomes thermodynamically unfavourable above

approximately 1140K, 940K, and 989K, respectively. These observations pertain to the specific molecular structure models investigated and cannot be generalised to iron(III) oxide nanoparticles of corresponding sizes, for which the true ground-state structures remain unknown.

The thermodynamic analysis of the dehydrogenation pathways shows that NH_3 dehydrogenation can be thermodynamically favourable on each of the four Fe(III) oxide structures, though the favourability depends on the particular elementary step and on the Fe(III) oxide molecules examined. Molecular hydrogen formation was found to be thermodynamically non-spontaneous at all temperatures on all four models; however, the reaction may still proceed if sufficient energy is available to overcome the activation barrier. The rate-determining step in NH_3 dehydrogenation was found to be $NH^* \rightarrow N^* + H^*$ for the n = 1–3 models and $NH_2^* \rightarrow NH^* + H^*$ for the n = 4 model (* represents adsorption). On all four models, the final H_2 formation step exhibits the highest overall energy barrier in the catalytic cycle.

Taken together, these results provide a first systematic, if incomplete, account of the interplay between electronic structure, spin state, and catalytic reactivity in small iron(III) oxide molecular structures. The findings suggest that an accurate description of the catalytic properties of iron oxide nanosystems will ultimately require a comprehensive treatment of all relevant spatial and spin configurations the task that remains computationally challenging and that is expected to benefit from advances in both multi-configurational methods and global structure search algorithms.

Streszczenie

W mojej pracy szczegółowo zbadałem strukturę przestrzenną, strukturę elektronową i wydajność katalityczną cząsteczek tlenku żelaza(III) w procesie produkcji wodoru poprzez rozkład amoniaku – reakcji istotnej dla zrównoważonych zastosowań energetycznych. Początkowo badałem konfiguracje spinowe i przestrzenne tlenku Fe(III), a także właściwości redoks. Badania geometrii latawca, wrzeciona i liniowej sprzyjają konfiguracjom o wysokiej otwartej powłoce z konfiguracjami ferromagnetycznymi lub antyferromagnetycznymi, a zaobserwowano, że redukcja i utlenianie wpływają na strukturę i stany spinowe, prowadząc do przemian izomerycznych. Obliczony przeze mnie standardowy potencjał redukcyjny względem standardowej elektrody wodorowej (SHE) mieści się w zakresie od -0,37 do -0,72 V, w zależności od geometrii stanu spinowego i metod zastosowanych do obliczeń. Aby zbadać proces rozkładu amoniaku, wykorzystałem metodę reakcji indukowanej siłą sztuczną (AFIR) w połączeniu z obliczeniami teorii funkcjonału gęstości (DFT) z wykorzystaniem hybrydowego funkcjonału wymiany i korelacji (B3LYP), aby systematycznie zbadać mechanizmy i energetykę reakcji. Moje obliczenia pokazują, że swobodna energia adsorpcji cząsteczek amoniaku na cząsteczkach (Fe2O3)n (gdzie n = 10-4) wykazuje tendencję zależną od rozmiaru, stopniowo malejąc wraz ze wzrostem rozmiaru (Fe2O3)n od form monomerycznych do trimerycznych (n = 1 do 3), a następnie nieznacznie wzrastając w przypadku tetramerycznych (Fe2O3)4. To niemonotoniczne zachowanie sugeruje optymalny rozmiar (Fe2O3)n dla aktywacji amoniaku. Najkorzystniejsza adsorpcja amoniaku, charakteryzująca się energią wiązania 28,55 kcal/mol, zachodzi na dimerycznych

cząsteczkach Fe2O3, gdzie cząsteczka amoniaku koordynuje się z nisko skoordynowanym (dwukoordynacyjnym) centrum żelaza, tworząc wiązanie Fe-N o długości 2,11 Å. Taka geometria ułatwia efektywny transfer ładunku i nakładanie się orbitali między wolną parą azotową a wolnymi orbitalami d żelaza. Dzięki kompleksowej analizie sekwencyjnych ścieżek dehydrogenacji i mechanizmów tworzenia wodoru cząsteczkowego w różnych rozmiarach cząsteczek tlenku żelaza(III), zidentyfikowałem etapy determinujące szybkość reakcji, rządzące każdym cyklem katalitycznym. Moje wyniki ujawniają, że kinetyczne wąskie gardło dla całkowitej dehydrogenacji amoniaku na (Fe2O3)n jest z natury zależne od rozmiaru. W szczególności, dla mniejszych tlenku Fe(III) (n = 1–3), etap elementarny $NH* \rightarrow N* + H*$ stanowi proces ograniczający szybkość reakcji, wymagający najwyższej energii aktywacji wzdłuż współrzędnej reakcji. Etap ten obejmuje rozerwanie silnego wiązania N−H przy jednoczesnym utworzeniu związanych z powierzchnią form azotu i wodoru. Ponadto, moja analiza termodynamiczna i kinetyczna wskazuje, że tworzenie wodoru cząsteczkowego jest energetycznie i kinetycznie faworyzowane po częściowym, a nie całkowitym rozkładzie amoniaku na tych powierzchniach tlenku żelaza(III). Ta preferencyjna ścieżka sugeruje, że pośrednie formy NHx (gdzie x = 1 lub 2) służą jako optymalne prekursory do generowania H2, ponieważ utrzymują wystarczającą ruchliwość powierzchniową, jednocześnie unikając nadmiernej stabilizacji całkowicie odwodornionych atomów azotu. Te mechanistyczne spostrzeżenia dostarczają cennych wskazówek do projektowania bardziej wydajnych katalizatorów na bazie żelaza do rozkładu amoniaku i podkreślają kluczową rolę tlenku Fe(III) o różnej wielkości cząstek w dostosowaniu aktywności katalitycznej i selektywności dla zrównoważonej technologii produkcji wodoru.

Acknowledgments

First and foremost, I would like to express my deepest gratitude to my supervisor, Maciej Bobrowski, for his continuous support, guidance, and encouragement throughout the doctoral journey. His expertise, insightful feedback, and constructive criticism and delivered with care and understanding have been instrumental in shaping both the direction and quality of this PhD dissertation.

I am also thankful to the members of the Prof. Taketsugu's Quantum chemistry group in Hokkaido University, whose valuable discussions and collaborative spirit contributed to many of the ideas developed in this study. Special thanks to Prof. Andey Lyalin, Prof. Tetsuya Taketsugu for their assistance and helpful suggestions with computational and theoretical analyses during my stay at the Hokkaido University. I am truly grateful for the opportunity to work with you, and I am deeply thankful for the knowledge and perception you have imparted to me.

I gratefully acknowledge the CI-TASK for providing access to high-performance computing resources, without which the extensive quantum chemical simulations presented in this thesis would not have been possible. I would also like to to express my deepest gratitude to Prof. Anna Lisowska's group at Gdansk University of Technology and Prof. Piotr Skurski's group at the University of Gdansk. Our collaboration and discussions have enriched my research experience. The stimulating scientific environment we shared has fostered my growth and provided invaluable insights and perspectives. On a personal note, I extend my heartfelt thanks to my family and friends for their unwavering love, patience, and emotional

support throughout doctoral journey. Their belief in me helped me persevere through the most challenging phases of this work.

Finally, I am thankful to all those who, in one way or another, contributed to the successful completion of this thesis.

Contents

1 Introduction **8**

1.1 Fe_2O_3 nanoparticles . . . 12

1.2 Use of Fe_2O_3 as catalyst for H_2 production from ammonia . . . 18

2 Research Gap and Hypothesis **20**

2.1 Identification of Research Gap . . . 20

2.2 Research Hypothesis . . . 21

3 Scope and objectives **1**

4 Electronic structure methods **4**

4.1 Basic concepts and the Schrödinger equation . . . 5

4.1.1 Restricted and unrestricted Hartree-Fock approximations . . . 6

4.2 Post-Hartree-Fock methods: Correlated methods . . . 8

4.2.1 Configuration Interaction . . . 9

4.2.2 Multi-Configurational Self-consistent field (MCSCF) . . . 10

4.2.3 Second order Møller-Plesset Perturation theory . . . 11

4.3 Density Functional Theory methods . . . 12

4.4 Atomic centered basis functions . . . 13

5 Theoretical approaches for chemical reactivity **15**

5.1 Transition state theory . . . 15

5.2 Artificial Force Induced Reaction path search for exploring potential energy surface . . . 16

5.3 Born-Haber cycle and derivation of standard redox potential . . . 18

6 Results **21**

6.1 Electronic structures of Fe(III) oxide . . . 21

6.1.1 $(Fe_2O_3)_1$ . . . 22

6.1.2 $(Fe_2O_3)_2$ . . . 37

6.1.3 $(Fe_2O_3)_{3,4}$ . . . 39

6.1.4 Charges . . . 42

6.1.5 HOMO-LUMO gap . . . 47

6.2 NH_3 decomposition reaction on $(Fe_2O_3)_n$, n=1-4 . . . 50

6.2.1 **Structure of $(Fe_2O_3)_n$ molecules with** $n = 1 - 4$ . . . 51

6.2.2 **Ammonia adsorption on $(Fe_2O_3)_n$ molecules** 52
6.2.3 **NH_3 decomposition on Fe_2O_3** 55
6.2.4 **NH_3 decomposition on Fe_4O_6** 61
6.2.5 **NH_3 decomposition on Fe_6O_9** 63
6.2.6 **NH_3 decomposition on Fe_8O_{12}** 65

7 Comparison and conclusion **67**

Appendices **71**

A Supporting Information **71**

B Participation another research projects **73**

C Scientific Achievements **74**

8 Bibliography **76**

List of Figures

1 Molecular coordinate system 6
2 Construction of CASSCF configurations. 10
3 Adiabatic and AFIR Potential energy surfaces 17
4 AFIR reaction path search for NH_3 decomposition on Fe_2O_3 18
5 Born-Haber cycle adapted for 2 kind of one-electron reduction reactions. 19
6 Molecular structures of UB3LYP/aug−cc−pVTZ optimized lowest-energy states of iron trioxides and the corresponding cations and anions. Total spins (S) are shown for each optimized state. No symmetry was imposed on the geometry. The structures were optimized in vacuum. Mulliken (M) and Hirshfeld (H) partial charges are shown in parentheses for the iron atom. Spin density values are shown in blue. If a given lowest-energy state among all those considered was characterized by an antiferromagnetic arrangement of spins, this is indicated in the drawing. 24

7 Molecular structures of UB3LYP/aug−cc−pVTZ optimized lowest-energy states of cobalt trioxides and the corresponding cations and anions. Total spins (S) are shown for each optimized state. No symmetry was imposed on the geometry. The structures were optimized in a vacuum. Mulliken (M) and Hirshfeld (H) partial charges are shown in parentheses for the cobalt atom. Spin density values are shown in blue. If a given lowest-energy state among all those considered was characterized by an antiferromagnetic arrangement of spins, this is indicated in the drawing. 25

8 Bond lengths (Å) of the lowest-energy configurations of iron(III) and cobalt(III) oxides found at the UB3LYP/aug−cc−pVTZ level of theory. . 26

9 UB3LYP/aug−cc−pVTZ relative energies [kcal/mol] calculated with respect to the lowest-energy state of kite iron trioxide ($S = 4$) and linear cobalt trioxide ($S = 0$; antiferromagnetic conf.), respectively. The energies of both singlet states with non-magnetic (non-magn.) and antiferromagnetic configurations were taken into account. The lowest energy is marked with a circle. 26

10 UMP2/aug−cc−pVTZ relative energies [kcal/mol] calculated with respect to the lowest-energy anti-ferromagnetic singlet ($S = 0$) state of the linear iron and cobalt trioxide, respectively. Non-magnetic singlet states are marked in a lighter color. The lowest energy is marked with a circle. 27

11 DFT UB3LYP/aug−cc−pVTZ relative energies [kcal/mol] calculated with respect to the lowest-energy state of ferromagnetic cation ($S = 4.5$) or anion ($S = 1/2$, including antiferromagnetic conf.) of a kite iron trioxide, respectively. The energies of both doublet states—with ferromagnetic (ferromagn.) and antiferromagnetic configurations—were taken into account. The lowest energy is marked with a circle. 30

12 DFT UB3LYP/aug−cc−pVTZ relative energies [kcal/mol] calculated with respect to the lowest-energy doublet state ($S = 1/2$, including antiferromagnetic conf.) of the cation and anion of a kite cobalt trioxide, respectively. The energies of both doublet states—with ferromagnetic (ferromagn.) and antiferromagnetic configurations—were taken into account. The lowest energy is marked with a circle. 30

13 UMP2/aug−cc−pVTZ relative energies [kcal/mol] calculated with respect to the lowest-energy anti-ferromagnetic doublet ($S = 1/2$) state of the kite iron trioxide. Ferromagnetic (ferromagn.) doublet states are marked in lighter color. The lowest energy is marked with a circle. 31

14 UMP2/aug−cc−pVTZ relative energies [kcal/mol] calculated with respect to the lowest-energy anti-ferromagnetic quartet ($S = 3/2$; cation) and anti-ferromagnetic doublet ($S = 1/2$; anion) states of the linear cobalt trioxide. Ferromagnetic doublet states are marked in lighter color. The lowest energy is marked with a circle. 31

15 Bond lengths (Å) of the lowest-energy configurations of iron(III) and cobalt(III) oxides found at the UMP2/aug−cc−pVTZ level of theory. Antiferromagnetic states were not taken into account at this level of theory. 32

16 Lowest-energy structures. n=2. B3lyp/aug-cc-pVTZ 37

17 DFT B3LYP relative energies [kcal/mol] (calculated against the energies of D3 structure (S=10)) revealed for all 6 identified structures of the $(Fe_2O_3)_2$ Each subfigure was captioned by the basis set used during the computations. 39

18 Lowest-energy structures of $(Fe_2O_3)_{3,4}$. B3lyp/lanl2dz 41

19 B3LYP/LANL2DZ relative energies [kcal/mol] (calculated against the energies of T1 structure (S=15) for n=3 and Q2 structure (S=20) revealed for 4 identified structures of the $(Fe_2O_3)_n$ where n=3,4 respectively 42

20 Mulliken partial charges for n=1. 44

21 Mulliken partial charges for n=2. 45

22 Mulliken partial charges for n=3 and n=4. 45

23 Average Mulliken partial charges found for the lowest-energy structures of $(Fe_2O_3)_n$ (points connected with dashed lines) for respective n. 46

24 Depiction of larger-size iron trioxide particle. Surface positive partial charges of iron atoms were ilustrated along with the interaction of the surface with negative ions of liquids. 47

25 HOMO LUMO gap 50

26 The most stable structures of $(Fe_2O_3)_n$ molecules with $n = 1-4$. The total spin S and the binding energy E_b, of the molecules are shown in inserts. 52

27 Optimized geometries of NH_3 adsorbed on $(Fe_2O_3)_n$ molecules for $n = 1$–4. N−Fe distances (Å) are shown in parentheses, along with the partial atomic charges on neighboring atoms. The total spin S of the molecules is shown in the insets. 54

28 Temperature dependence of the adsorption free energy for NH_3 adsorption on $(Fe_2O_3)_n$ molecules with $n = 1$–4 at 1 atm. 55

29 (a) The energy profile for $NH_3^* \rightarrow NH_2^*$ + H^* $\rightarrow$ NH^* + $2H^*$ $\rightarrow$ N^* + $3H^*$ reaction path on the kite-like isomer of Fe_2O_3 at T=298.15 K. (b) Geometries of the optimized equilibrium and transition states along the reaction path. 58

30 (a) The energy profile for $NH_3^* \rightarrow NH_2^*$ + H^* $\rightarrow$ NH^* + $2H^*$ $\rightarrow$ N^* + $3H^*$ reaction path on the linear-type isomet of Fe_2O_3 at T=298.15 K. (b) Geometries of the optimized equilibrium and transition states along the reaction path. 59

31 (a) The energy profile for H_2 formation on the kite-like Fe_2O_3 structure at T=298.15 K. (b) Geometries of the optimized equilibrium and transition states along the reaction path. 60

32 (a) The energy profile for H_2 formation on the linear isomer of the Fe_2O_3 at T=298.15 K. (b) Geometries of the optimized equilibrium and transition states along the reaction path. 61

33 (a) The energy profile for $NH_3^* \rightarrow NH_2^*$ + H^* $\rightarrow$ NH^* + $2H^*$ $\rightarrow$ N^* + $3H^*$ and H_2 formation reaction paths on the $(Fe_2O_3)_2$ at T=298.15 K. (b) Geometries of the optimized equilibrium and transition states along the reaction path. 63

34 (a) The energy profile for $NH_3^* \rightarrow NH_2^*$ + H^* $\rightarrow$ NH^* + $2H^*$ $\rightarrow$ N^* + $3H^*$ and H_2 formation reaction paths on the $(Fe_2O_3)_3$ at T=298.15 K. (b) Geometries of the optimized equilibrium and transition states along the reaction path. 65

35 (a) The energy profile for $NH_3^* \rightarrow NH_2^*$ + H^* $\rightarrow$ NH^* + $2H^*$ $\rightarrow$ N^* + $3H^*$ and H_2 formation reaction path on the $(Fe_2O_3)_4$ at T=298.15 K. (b) Geometries of the optimized equilibrium and transition states along the reaction path. 66

36 Reaction barrier ($\Delta G^{\ddagger}$) for NH_3 dehydrogenation and H_2 formation reactions on $(Fe_2O_3)_n$ ($n = 1 - 4$). 70

37 Structures and Fe-O bond lengths of Fe_2O_3 with total spins $S = 0, 4$, and 5. The bond lengths are given in Å. (a) B3LYP/6-31+G*, (b) M06/6-31+G*, and (c) wB97XD/6-31+G*. 71
38 The lowest energy isomers of Fe_2O_3 with total spin S=4. The binding energies, E_b, are shown in inserts. 72
39 The lowest energy isomers of $(Fe_2O_3)_2$ with total spin S=10. The binding energies, E_b, are shown in inserts. 72
40 The lowest energy isomers of $(Fe_2O_3)_3$ with total spin S=15. The binding energies, E_b, are shown in inserts. 72
41 The lowest energy isomers of $(Fe_2O_3)_4$ with total spin S=20. The binding energies, E_b, are shown in inserts. 72
42 Variation of Gibbs free energy (ΔG) with temperature for each dehydrogenation step of NH_3 on $(Fe_2O_3)_n$ (n=1−4) molecules, along with the H_2 formation reaction $NH^* + 2H^* \rightarrow NH^* + H_2$. For simplicity, the temperature dependence of entropy, $S(T)$, was neglected. 73

List of Tables

1 MP2/aug−cc−pVTZ and B3LYP/aug−cc−pVTZ values of vertical Ionization Potential (vIP), adiabatic Ionization Potential (aIP), vertical Electron Affinity (vEA), and adiabatic Electron Affinity (aEA) for Fe_2O_3 and Co_2O_3. The values are given in eV. The left-side superscript m in ^{m}calc represents the values calculated at the spin state m. The right-side superscripts refer to the literature data. 33
2 UMP2/aug−cc−pVTZ and UB3LYP/aug−cc−pVTZ values of absolute standard reduction potentials (E°) and standard reduction potentials calculated against the SHE (E°_{SHE}) for the lowest-energy states of Fe_2O_3 and Co_2O_3. The temperature was 298.15 K and the pressure was 1013 hPa (1 atm). Relative water permittivity $\epsilon_r = 80$. The notation $(+1/0)$ corresponds to the reduction of the cation to the neutral molecule, and $(0/-1)$ corresponds to the reduction of a neutral molecule to an anion. The values are given in V. 34
3 Average partial atomic charges Fe ions in lowest energy state of $(Fe_2O_3)_1$ 43
4 NH_3 adsorption free energy ΔG_{ads} and d(Fe – N) bond length in various size of $(Fe_2O_3)_n$ where $n = 1 - 4$. 54

5 Relative energies (ΔE, kcal/mol) calculated using 6-31+G* and aug-cc-pVTZ basis sets with respect to the lowest energy state of kite-like Fe_2O_3 across three different DFT functionals. 71

1 Introduction

The global energy system stands at a critical juncture as worldwide energy consumption continues its relentless upward trajectory, driven by population growth, economic development, and increasing industrialization, particularly in emerging economies. According to the International Energy Agency (IEA), global energy demand is projected to increase by 50% between 2020 and 2050, presenting unprecedented challenges for energy security, environmental sustainability, and climate stability. This exponential growth in energy demand has intensified the urgency to identify and deploy alternative, environmentally sustainable energy sources that can meet the growing needs while mitigating the adverse environmental impacts associated with traditional energy systems.

Despite remarkable advances in renewable energy technologies and their rapidly declining costs, the global energy mix remains heavily skewed toward fossil fuels. Coal, oil, and natural gas collectively account for approximately 80% of global primary energy consumption, a proportion that has remained stubbornly persistent over the past several decades. This continued dominance of fossil fuels can be attributed to several interconnected factors: the extensive existing infrastructure that represents trillions of dollars in sunk investments, the high energy density and reliability of conventional fuels, established supply chains and market mechanisms, and the relatively low short-term marginal costs that fail to account for externalized environmental and social costs.

The renewable energy sector, while experiencing unprecedented growth rates with solar and wind technologies achieving grid parity in many markets, still faces significant challenges in achieving the scale and speed of deployment necessary for deep decarbonization. Solar photovoltaic capacity has grown by over 20% annually in the past decade, and wind power has similarly expanded, yet these technologies collectively represent less than 12% of global electricity generation and an even smaller fraction of total energy consumption when including transportation, heating, and industrial

processes.

The environmental ramifications of sustained fossil fuel dependence extend far beyond immediate local pollution, encompassing global climate disruption that threatens the fundamental stability of Earth's systems. Greenhouse gas emissions from fossil fuel combustion, primarily carbon dioxide (CO_2), methane (CH_4), and nitrous oxide (N_2O), constitute approximately 75% of total anthropogenic emissions. These emissions have driven atmospheric CO_2 concentrations from pre-industrial levels of 280 parts per million to over 420 ppm in 2023, the highest levels in over 3 million years.

The cascading effects of this greenhouse gas accumulation manifest in multiple interconnected ways. Rising global average temperatures, currently 1.2 °C above pre-industrial baselines, are accelerating ice sheet collapse, sea-level rise, and thermal expansion of oceans. Extreme weather events, including unprecedented heatwaves, intensified hurricanes, prolonged droughts, and catastrophic flooding, are becoming more frequent and severe, causing substantial economic damages estimated at hundreds of billions of dollars annually and disproportionately affecting vulnerable populations.

Long-term ecological disruption includes ocean acidification, which threatens marine ecosystems and food security; biodiversity loss accelerated by habitat destruction and changing climatic conditions; and disruption of hydrological cycles affecting freshwater availability for billions of people. The Intergovernmental Panel on Climate Change (IPCC) has emphasized that limiting global warming to 1.5°C requires rapid, far-reaching, and unprecedented changes in all aspects of society, including achieving net-zero CO_2 emissions by 2050.

Beyond climate impacts, the environmental and health consequences of fossil fuel extraction, processing, and combustion create additional urgent concerns. Air pollution from fossil fuel combustion is responsible for an estimated 8.7 million premature deaths annually, with particulate matter ($PM_{2.5}$) nitrogen oxides, and sulfur compounds causing respiratory and cardiovascular diseases. Water contamination from oil spills, coal mining, and hydraulic fracturing threatens freshwater resources and aquatic ecosystems. Land degradation from mining operations, pipeline construction, and waste disposal further compounds environmental damage.

In response to these mounting challenges, countries worldwide are implementing increasingly ambitious climate policies and clean energy targets. The Paris Agreement, ratified by 196 countries, established a framework for limiting global temperature rise and achieving carbon neutrality in the second half of this century. More than 70 countries, representing over 75% of global emissions, have committed to achieving net-zero

emissions by 2050 or shortly thereafter.

National renewable energy targets have become increasingly aggressive, with many countries aiming for 50-100% renewable electricity by 2030-2050. The European Union's Green Deal aims for climate neutrality by 2050 and a 55% reduction in greenhouse gas emissions by 2030. China, the world's largest emitter, has committed to carbon neutrality by 2060 and peak emissions before 2030. The United States has rejoined international climate efforts with a commitment to reduce emissions by 50-52% below 2005 levels by 2030.

These policy commitments are increasingly supported by economic incentives, including carbon pricing mechanisms covering over 20% of global emissions, renewable energy subsidies, and fossil fuel subsidy reforms. Investment in clean energy infrastructure has exceeded 1.7 trillion annually, though this must more than double to meet climate targets according to the IEA.

Achieving a sustainable energy transition requires not only the deployment of individual renewable technologies but comprehensive system transformation encompassing generation, storage, transmission, and demand-side management. The intermittent nature of solar and wind resources necessitates complementary technologies including energy storage systems, demand response mechanisms, smart grid infrastructure, and flexible backup generation.

Battery storage costs have declined by over 85% in the past decade, making grid-scale storage increasingly viable for managing renewable energy intermittency. However, storage requirements for deep decarbonization, particularly for seasonal energy storage and long-duration applications, remain technologically and economically challenging with current lithium-ion battery technology.

Power system flexibility must also be enhanced through improved transmission infrastructure enabling regional energy balancing, electrification of transportation and heating systems to create more responsive demand profiles, and industrial process modifications to accommodate variable renewable energy supply.

Energy efficiency improvements across all sectors represent perhaps the most cost-effective approach to reducing energy demand and facilitating renewable energy integration. Building retrofits, industrial process optimization, and transportation electrification can significantly reduce total energy requirements while improving economic competitiveness.

Among emerging clean energy technologies, hydrogen represents a particularly promising solution for addressing several critical challenges in the energy transition. As

the most abundant element in the universe, hydrogen offers virtually unlimited resource potential when produced from renewable sources. Its unique properties as an energy carrier enable applications across multiple sectors that are difficult to electrify directly, including heavy industry, long-distance transportation, seasonal energy storage, and chemical feedstock production.

Hydrogen's high energy density by mass (120 MJ/kg) makes it particularly suitable for applications requiring high energy-to-weight ratios, such as aviation and marine transport. Its ability to be stored for extended periods without degradation offers potential solutions for long-term energy storage needs that complement shorter-duration battery systems. Furthermore, hydrogen can be transported through existing pipeline infrastructure with modifications, potentially enabling large-scale energy transport and international energy trade.

The hydrogen economy encompasses multiple production pathways, each with distinct environmental and economic implications. Electrolytic hydrogen production, using renewable electricity to split water molecules

$$H_2O \rightarrow H_2 + \frac{1}{2}O_2, \tag{1.1}$$

offers a pathway to completely carbon-free hydrogen when powered by renewable energy sources. This process, while currently energy-intensive with efficiencies around 70-80%, provides a means of converting excess renewable electricity into storable chemical energy.

Alternative production routes include steam methane reforming (SMR) with carbon capture and storage (CCS), which can significantly reduce but not eliminate CO_2 emissions from natural gas feedstock. Ammonia decomposition represents another promising approach, as ammonia (NH_3) can serve as a hydrogen carrier that can be more easily stored and transported than gaseous hydrogen. The catalytic decomposition of ammonia

$$(NH_3 \rightarrow \frac{1}{2}N_2 + 1.5H_2) \tag{1.2}$$

using appropriately designed catalysts offers high-purity hydrogen production with only nitrogen as a byproduct.

This dissertation addresses critical technological and economic barriers to large-scale hydrogen deployment, with particular focus on advanced electrolytic production methods and efficient ammonia decomposition catalysts. The research aims to:

1. Design and characterize novel catalyst systems for ammonia decomposition that achieve high conversion rates at reduced temperatures 2. Conduct comprehensive

techno-economic analyses of integrated hydrogen production systems 3. Evaluate the environmental lifecycle impacts of hydrogen production pathways 4. Assess the potential for hydrogen technologies to contribute to deep decarbonization scenarios

This research contributes to the urgent need for technological solutions that can accelerate the deployment of clean hydrogen production systems. By addressing key bottlenecks in electrolytic hydrogen production and ammonia-based hydrogen storage and release, this work aims to reduce costs, improve efficiency, and enhance the viability of hydrogen as a clean energy vector.

The expected contributions include novel catalyst formulations, improved understanding of reaction mechanisms, optimized process conditions, and comprehensive economic and environmental assessments that can inform policy decisions and industrial deployment strategies. These advances are essential for realizing hydrogen's potential as a cornerstone technology in the global transition to sustainable energy systems.

The transformation of global energy systems represents one of the most significant technological and societal challenges of the 21st century. Success in this endeavor requires not only continued innovation in renewable energy technologies but also the development of complementary systems that can address the limitations of variable renewable resources. Hydrogen technologies, particularly when integrated with renewable energy systems, offer pathways to deep decarbonization that are technically feasible and potentially economically competitive. This dissertation aims to contribute to that critical transformation through focused research on key enabling technologies.

1.1 Fe_2O_3 nanoparticles

Iron (III) oxide, also known as red iron oxide, can be formed under various conditions. One of the most common process is the rusting of iron. In laboratory settings, it can also be synthesized through the electrolysis of aqueous sodium chloride or baking soda, using an iron anode submerged in the solution. Under these conditions, the anode undergoes oxidation, forming iron (III) ions. The intermediate product, hydrated iron (III) oxide—commonly known as rust and often denoted as Fe(O)OH—undergoes dehydration at elevated temperatures, resulting in the formation of red-brown ferric oxide.

However, the anodization of iron and steel is generally not beneficial, as the rust layer produced is porous and hygroscopic, making it ineffective at preventing further corrosion. This contrasts with the anodization of metals like aluminum or titanium,

which form protective, adherent oxide layers [1].

Nevertheless, highly ordered iron oxide nanotubes with smooth and homogeneous walls have been successfully synthesized via potentiostatic anodization of iron foil in ethylene glycol [2]. High-quality iron trioxide films have also been produced using LPCVD and PVD techniques to provide corrosion protection [3; 4].

Iron trioxide can also be obtained by reacting an iron (II) salt, such as ferric chloride, with a strong hydroxide. This reaction yields iron (III) hydroxide, a brownish gelatinous precipitate, which can be calcined to form Fe_2O_3. The compound can also form readily by oxidation of iron (II) hydroxide when exposed to air or oxidizing agents such as hydrogen peroxide. However, these methods typically produce chemically pure compounds with irregular structures or particle sizes.

In the case of nano- and microparticles of iron oxide, a wide variety of synthesis methods have been explored, including physical, chemical, and even microbiological approaches [5; 6; 7; 8]. Physical methods usually involve the physical vapor deposition (PVD) of pure iron, followed by inevitable thermal oxidation or calcination [3; 8; 9].

The most common and efficient chemical pathway for synthesizing iron oxides is wet (co)precipitation of iron salts, typically resulting in black ferrimagnetic Fe_3O_4 (magnetite) and/or reddish ferromagnetic Fe_2O_3 [6; 10]. In this process, ferrous and/or ferric salts are dissolved in aqueous media under controlled pH conditions. Magnetite can subsequently undergo oxidation to form iron (III) oxide.

In aqueous solution, both ferrous and ferric iron ions form hexacoordinated aquo complexes, $[Fe(H_2O)_6]^{h+}$, with the ferric complex being more acidic in accordance with the Lewis definition of acids. Most synthesis routes proceed via a rapid increase in pH, leading to the precipitation of ferrous and ferric hydroxides, $Fe(OH)_2$ and $Fe(OH)_3$, respectively. These precipitates typically adopt more complex forms, including aquohydroxo complexes of the type $[Fe(OH)_h(H_2O)_{6-h}]^{(z-h)+}$ and oxohydroxo complexes of the form $[FeO_a(OH)_b]^{(z-2a-b)+}$ [11].

Once hydrolysis has occurred, resulting complexes are thermodynamically unstable and readily condense further. The following the process obtained by Henry, Jolivet and Livage[12], this condensation proceeds by one of two routes, each made possible by the nucleophilic character of the coordinated hydroxo groups. Where the precursor is an aquohydroxo complex, a coordinated water is displaced and a hydroxo group bridges two metal centres, giving an M−OH−M linkage. Where the precursor is an oxohydroxo complex, there is no aquo group available to leave, so bridging instead follows a two-step associative pathway that expels water and creates an M−O−M (oxo) bridge where

M represents metal, termed oxolation. Which pathway dominates, and the structure of the condensed product that results, is governed largely by the degree of hydroxylation h, a dependence that has been documented not only for iron but across a range of metal cations[12].

It has been reported that hydroxylation of ferric ions in aqueous solution by the addition of a base at room temperature leads to the formation of ferrihydrite—an amorphous, thermodynamically unstable intermediate phase. Ferrihydrite is a poorly crystalline iron oxyhydroxide with the general formula $Fe_{10}O_{14}(OH)_2$, and is believed to originate from Keggin-type molecules [13; 14].

Depending on solution acidity, ferrihydrite can transform into nanocrystalline domains of hematite, goethite, or α-Fe_2O_3, although the transformation pathways differ [15]. As nucleation proceeds, ferrihydrite molecules grow and can reach several nanometers in size. However, it is well-established that iron (III) oxides remain largely amorphous or poorly crystalline up to a certain particle size and often incorporate water or other chemical groups, depending on the synthesis route [15].

Furthermore, evidence suggests that the growth of both synthetic and natural phases of iron (III) oxides does not follow a classical molecule-by-molecule mechanism. Instead, it occurs via the aggregation of prenucleation molecules [13; 14].

Moreover, the crystallization process can be delayed or even inhibited by certain complexing ligands, such as silicate or phosphate. The entire process—from the initial iron precursor salts to the formation of ferrous and ferric oxides—is only moderately reproducible, primarily due to the presence of intermediate phases in the final product. Furthermore, when ferric oxide nanoparticles produced by wet chemical synthesis are to be used, one must account for the presence of residual water and other by-products in the final material.

Scheck et al. investigated the mechanism of solid-phase formation of iron (oxyhydr)oxides from solution [16]. They employed potentiometric titration, gradually adding an iron(III) solution into hydrochloric acid while maintaining a nearly constant pH using automatic counter-titration with sodium hydroxide. According to their experiments, in the initial stages, the condensation of iron (oxyhydr)oxides proceeds via elimination of water molecules and the formation of hydroxo bridges—characteristic of the *olation* mechanism. Subsequently, the *oxolation* mechanism is activated, wherein the formation of a water-leaving group directly results in an oxo bridge between two iron atoms. This mechanism was previously proposed by Jolivet et al. [17].

The formation of numerous small and poorly crystalline particles was also observed

when only iron(III) salt ($FeCl_3 \cdot 6H_2O$) was used as the precursor [18]. LaGrow et al. proposed the use of sodium carbonate—a weaker base in aqueous media—instead of stronger bases, due to its direct influence on the growth rate of iron trioxide [18].

To date, comprehensive reports detailing the full chemical pathways from precursors to iron oxide nanostructures—including aspects like spin states, geometries, and influencing factors—remain largely unpublished. Despite this, wet chemical synthesis remains a relatively straightforward and energy-efficient method for nanoparticle production.

Among other synthesis techniques reported in the literature are microemulsion methods, sonochemical reactions, electrochemical deposition, hydrothermal synthesis, flow injection methods, electrospray, and flame synthesis [19; 20]. Some of these are also considered wet-chemical methods, as they use iron salts or alkoxides as precursors.

In the so-called *green synthesis* approach, biological organisms such as plants, bacteria, fungi, and algae are employed to produce iron oxide nanoparticles, resulting in a diverse range of shapes and sizes typically within the 1–100 nm range [21]. These methods involve hydrated iron salts or iron complexes that undergo chemical transformations via biochemical pathways. Cell-wall-associated and soluble enzymes are believed to participate in the synthesis, although the precise chemical mechanisms are not yet fully understood.

A significant advantage of green synthesis is that it typically requires lower temperatures than conventional chemical or physical methods. During synthesis, positively charged metal ions can aggregate on the surfaces of microbial cells, which are usually negatively charged due to the presence of carboxyl and phosphate groups [21]. Additionally, ferric oxide nanoparticles have been shown to exhibit antibacterial properties [22].

Many of these synthesis approaches enable the production of well-defined particle shapes and controlled size distributions.

Iron oxides play a significant role in industry, biology, medicine, and geology, and have attracted considerable interest [23; 24]. These compounds are well known for their magnetic properties, which are strongly correlated with high-spin configurations and long-range spatial ordering. In addition to their magnetism, iron oxides also exhibit redox activity, which is primarily associated with the oxidation state of the iron atoms. This redox activity is likely to influence magnetic behavior, as changes in oxidation state alter the electronic structure and spin configurations.

Sun et al. synthesized electrodes tightly coated with Fe_2O_3 nanoparticles and ap-

plied them in battery systems [25]. The Fe_2O_3-based electrode, used with 1-ethyl-3-methylimidazolium tetrafluoroborate ($EMIMBF_4$) ionic liquid as the electrolyte, demonstrated fully reversible operation across a voltage range of 0–4 V and achieved a notably high energy density of 177 W h kg^{-1}. This pseudocapacitive behavior was closely linked to redox transitions between Fe^{3+} and Fe^{2+} at the surface of the Fe_2O_3 nanoparticle layer [25].

The electrochemical properties of α-Fe_2O_3 (hematite) films have also been studied, especially in their roles as photoanodes or catalysts for water splitting reactions [26]. Beyond electrochemical applications, iron oxides are widely utilized in metallurgy, colored pigments, magnetic materials, and catalysis [23; 27].

Porous hematite nanoparticles have been employed as nanocarriers for the efficient delivery of the anticancer drug doxorubicin [28]. Iron oxide particles dispersed in a carrier fluid can form magnetic colloids, known as ferrofluids. The stability of such suspensions has been extensively studied, as even well-prepared nano- and microparticles of iron oxide can lose magnetic properties when suspended, or may not remain dispersed due to aggregation.

To ensure colloidal stability, surfactants are commonly used. In many cases, neat iron oxide particles are not inherently suspendable, and effective dispersion requires chemical agents that modify surface charge [29]. Suitable surfactants include isobutanol, citrate ions, proteins, starches, nonionic detergents, and polyelectrolytes [5; 29; 30]. These molecules contain functional groups that adsorb to the particle surface and enhance suspension stability through steric or electrostatic effects.

Although local minima alone may not reliably represent the stable structures of iron trioxides along their specific synthetic reaction pathways—especially for molecules of finite size—some computational studies of this type have already been conducted. Erlebach et al. employed the classical Born–Mayer potential, originally developed for ionic solids, with parameters fitted using a least-squares method based on a training dataset comprising DFT-calculated structures and energies of bulk Fe_2O_3 polymorphs [31].

In their work, all DFT computations for bulk structures were carried out under periodic boundary conditions using the Vienna Ab initio Simulation Package (VASP) with the Perdew–Burke–Ernzerhof (PBE) exchange–correlation functional. For smaller molecules, specifically $(Fe_2O_3)_n$ with $n = 1$–10, the local minima were identified using the Turbomole package, employing the B3LYP hybrid functional and a triple-zeta valence plus polarization (TZVP) basis set for all atoms [31].

However, their structural searches were limited to highly symmetric configura-

tions—for example, only a kite-like geometry was considered for the smallest iron trioxide molecule and they imposed a restricted set of spin states arbitrarily. Despite this, the authors claimed to have located global minima and concluded that the lowest-energy configuration for iron trioxide was a C_{2v} kite-shaped structure with spin $S = 0$. Non-alternating or less symmetric structures were not considered.

Similarly, in an earlier study by the same group [32], the search space for $(Fe_2O_3)_n$ structures with $n = 1 - 5$ was also restricted to a limited set of geometries. Nonetheless, the authors again reported having identified global minimum structures for these neutral molecules.

In contrast, Xun-Lei et al. used the DFT/B3LYP approach along with both LANL2DZ and 6-311+G(d) basis sets (the former in most cases) to explore a broader array of possible configurations for iron trioxide molecules [33]. Their results showed that while cage-like structures were generally stable, non-cage geometries were typically found to be the global minima. However, their analysis for the smallest iron trioxide molecules also considered only a single spatial configuration and a limited range of spin states.

The classical empirical potential energy function approach has been applied to a variety of metal (M) oxides (O) with general formulas of the type $(MO)_n$, $(M_3O_4)_n$, $(M_2O_3)_n$, $(MO_2)_n$, $(M_2O_5)_n$, and $(MO_3)_n$, for values of n ranging from 1 to 60, depending on the stoichiometry [34]. The potential used by the authors was based on Lennard-Jones and Born–Mayer interaction terms, and it primarily considered the formal charge of the metal ion. However, the spin states of the molecules were entirely neglected. Additionally, only highly symmetric structures were considered in their study.

Interestingly, the authors referred to the optimized structures as global minima, despite evaluating only a single type of configuration for each stoichiometric oxide at a given n. They concluded that their method predicts metal oxides to form exclusively compact, highly symmetric structures. For instance, in the case of the smallest M_2O_3 molecule, a spindle-like structure was identified as the most stable, although alternative configurations were not examined. For M_4O_6, the adamantane-like structure was reported as the lowest-energy configuration. Moreover, the study did not specify the metal element being modeled, and no distinctions were made between, for example, cobalt and iron oxides.

In a different approach, Mejia-Olvera et al. investigated neutral, cationic, and anionic $(Fe_3O_4)_{1-5}^{0/\pm1}$ structures—presumably corresponding to $(Fe_2^{3+}Fe^{2+}O_4)_{1-5}^{0/\pm1}$—using density functional theory (DFT) [35]. The initial candidate structures were obtained from trajectory data generated via scaled Born–Oppenheimer molecular dynamics simulations

performed at 1800 K. Optimized geometries were then selected from these trajectories. However, the study considered only a limited number of spin states for the Fe_3O_4 molecules, and the rationale behind this choice was not discussed.

1.2 Use of Fe_2O_3 as catalyst for H_2 production from ammonia

The ammonia decomposition reaction has recently received extensive attention due to its potential use as an alternative green energy source.[36; 37; 38; 39; 40] This reaction typically requires a catalyst and consists of two major steps. The first is ammonia dehydrogenation on the catalytic surface, leading to the formation of adsorbed nitrogen and hydrogen species. This is followed by nitrogen coupling, resulting in the formation of molecular nitrogen.[41] One of the key advantages of ammonia as a green energy source is its ability to be liquified at low pressure and a relatively low temperature of 20 °C, making it an attractive candidate for hydrogen storage and transportation. As with many other chemical processes, catalysts play a crucial role in ammonia decomposition to achieve fast and efficient H_2 production. Experimental and theoretical studies have demonstrated that Ru-based catalysts are the most active for ammonia decomposition.[41; 42; 43] However, ruthenium's high cost and limited availability pose challenges for its large-scale industrial application. Therefore, developing new types of cost-effective catalysts for NH_3 decomposition, based on non-noble metals or metal oxides, has become a significant area of research for effective hydrogen generation.[44] Numerous studies have focused on the activity of catalysts involving various metals and alloys.[45] Among the most studied non-noble metals, iron (Fe) stands out as a leading catalyst due to its low cost and availability. While the reactivity of Fe is lower compared to other transition metals, it can be enhanced by using nanoparticles instead of extended surfaces. Indeed, it is well known that the reactivity of small-size molecules can be finely tuned by adjusting their size, geometry, and electronic structure, making them promising catalysts in various catalytic processes.[46; 47; 48; 49; 50] For example, Nishimaki, *et al.*[51] experimentally studied ammonia decomposition on Fe nanoparticles of various grain sizes (20 nm to 1 μm) in an ammonia steam environment. Their findings indicated that the highly reactive surface of nanoparticles enhances NH_3 dissociation without increasing the nitrogen content in the gas phase, resulting in nitride phases that depend on the grain size and morphology.

As an alternative approach, ammonia decomposition reactions on small nanosized Fe structures are frequently investigated using density functional theory (DFT) methods. Theoretical studies suggest that the mechanisms of ammonia decomposition involve

stepwise dehydrogenation, where the rate-limiting step can vary depending on the size, type, and shape of the catalysts. Thus, Lanzani and Laasonen employed spin-polarized DFT to examine the adsorption and dissociation of NH_3 on a single nanosized icosahedral Fe_{55} structure.[52] Their research indicated that the overall reaction barrier for stepwise dehydrogenation was 1.48 eV, with different active sites on the Fe_{55} molecule (facets and vertices), where the rate-limiting step was the initial hydrogen dissociation. Similarly, Otero *et al.*[53] conducted a comprehensive comparative study on various sizes of Fe structures (Fe_{16}, Fe_{22}, Fe_{32}, Fe_{59}, Fe_{80}, Fe_{113}, Fe_{190}) and Fe(111) surfaces with additional adatoms. Their findings indicated that the reaction kinetics were influenced more by the strength of NH_3 adsorption rather than the activation energy barrier. Stronger NH_3 adsorption led to enhanced dissociation compared to desorption. The studies mentioned above primarily focus on the catalytic activities of large Fe packed structures and Fe surfaces in the ammonia decomposition reaction. However, Zhang *et al.*[54] specifically investigated the activities of relatively small Fe assemblies, ranging from single Fe atoms to four Fe atom assenblies Fe_4. They found that the highest catalytic activity for stepwise NH_3 dehydrogenation was observed with nonatomic iron assemblies. Interestingly, they observed that the rate-limiting steps differed: co-absorbate NH dissociation for Fe and Fe_3, and co-absorbate NH_2 dissociation for Fe_2 and Fe_4.

The NH_3 decomposition reaction can be enhanced in the presence of oxygen, where it can proceed through various pathways, including ammonia oxidation and hydrogen evolution reactions. Moreover, metal oxides are commonly employed as catalyst supports in ammonia decomposition to enhance dispersion and catalytic stability. Among these supports, widely used materials include Al_2O_3, TiO_2, as well as carbon nanotubes and nanofibers.[42; 55; 56; 57; 58; 59] However, metal oxides not only serve as support but also play a crucial role in hydrogen evolution reactions in electrocatalysis, where the oxidation state of metals significantly influences the catalytic activity of ammonia decomposition. In particular, iron-based oxides, such as Fe_2O_3, are extensively studied forms of iron oxide due to their low cost and abundance, although their activity and stability can vary depending on their structure and size.[60; 61; 62; 63; 64; 65; 66]

In this research, I elucidate the role of the size- and structural effects on the catalytic activity of iron-oxide-based nano-catalysts toward the efficient ammonia dehydrogenation process, which is the first step in the full ammonia decomposition reaction. In particular, I investigated the theoretical mechanisms of stepwise ammonia dehydrogenation on $(Fe_2O_3)_n$ structures with $n = 1 - 4$ to compare the reactivity of different-sized Fe(III) oxides using the Artificial Force Induced Reaction (AFIR) method.[67; 68]

Additionally, we examined the NH_3 adsorption and various energy barriers for NH_3 dehydrogenation on different active sites of Fe(III) oxides. My investigation aims to contribute to the design of nanocatalysts based on Fe_2O_3 by exploring the activity of small-sized Fe(III) oxides.

2 Research Gap and Hypothesis

2.1 Identification of Research Gap

Despite substantial advances in the field of electrocatalysis over the past two decades, several fundamental challenges continue to impede the design and deployment of efficient, cost-effective catalysts for sustainable hydrogen production. Although iron-based materials have emerged as structurally promising and economically viable alternatives to noble metal catalysts, their catalytic behaviour at the nanoscale remains insufficiently understood, and a rigorous theoretical framework for rationalising their performance is still absent from the literature.

A well-established body of work demonstrates that the catalytic activity of transition metal oxides are highly sensitive to size , geometric configuration, and electronic structure. Nevertheless, for iron oxide nanoparticles specifically, a systematic and comprehensive understanding of the interrelationship among structure size, spin state, and catalytic performance has not yet been established. The majority of existing investigations focus either on bulk-phase iron oxide materials or on a narrow selection of iron oxide onfigurations, thereby failing to provide an adequate exploration of the broader structural and energetic landscape accessible to these systems. This constitutes a significant gap, as size-dependent phenomena at the nanoscale can give rise to properties that diverge markedly from bulk behaviour.

A further, critical gap concerns the role of spin multiplicity in governing both the stability and the reactivity of transition metal oxides. Iron-containing systems are particularly complex in this regard, as the presence of multiple accessible spin states—

arising from the partially filled $3d$ shell of iron—can profoundly influence reaction pathways and associated energy barriers. Although the importance of spin-state effects in iron chemistry is broadly recognised, a quantitative and systematic treatment of their influence on the catalytic properties of $(Fe_2O_3)_n$ assemblies across a representative range of sizes remains an open question.

Moreover, it became evident that the number of possible spatial configurations of the isomers are exceptionally large, far exceeding initial expectations and predictions in the existing literature. This unexpected structural diversity significantly complicated the analysis, as each isomer required careful consideration of its geometry, stability, and possible spin states. As a result, the increased complexity introduced substantial challenges in both the systematic analysis of the isomers and the computational evaluation of their properties, leading to considerable delays in my research.

Last but not least and equally important limitation in the current literature is the incomplete mechanistic understanding of ammonia (NH_3) dehydrogenation on iron-based nanocatalysts. Experimental investigations, while valuable for establishing macroscopic trends, cannot readily resolve the atomistic details of reaction intermediates, transition states, and rate-determining steps. The application of automated reaction-pathway search methodologies—which are capable of systematically exploring complex potential energy surfaces without relying on chemically intuitive initial guesses—to iron oxide molecule systems remains largely unexplored. This methodological gap limits the reliability and completeness of mechanistic descriptions derived from conventional, manually guided approaches.

Taken together, these gaps highlight the pressing need for a rigorous, integrated theoretical investigation that combines systematic structural exploration, multi-spin-state electronic structure analysis, and automated reaction mechanism studies for iron oxide nanoparticle. The present dissertation is designed to address this need directly.

2.2 Research Hypothesis

The primary hypothesis of my dissertation was that iron(III) oxides can exhibit redox-active behavior at the molecular level, and I was able to calculate redox potentials for $(Fe_2O_3)_1$ systems. It is further hypothesized that these minimal iron oxide units are capable of undergoing measurable redox processes that can be theoretically characterized and quantified.

A central assumption of this work was that redox properties can serve as a reliable and self-consistent descriptor for comparing the spatial and electronic structures of

metal oxide systems. In particular, it is proposed that calculated standard redox potentials can be used as meaningful parameters to evaluate and compare different iron oxide configurations, providing direct insight into their electronic structure and reactivity.

Another central hypothesis of my dissertation was that the catalytic performance of $(Fe_2O_3)_n$ structures is fundamentally governed by their size-dependent structural and electronic properties, including spin configuration, and that these properties can be systematically characterised and correlated with catalytic efficiency for hydrogen production via NH_3 dehydrogenation. It is further proposed that a comprehensive theoretical treatment, integrating global structural optimisation, multi-spin-state electronic structure calculations, and automated reaction-pathway search techniques, will provide the mechanistic insight necessary to establish predictive structure–activity relationships.

In support of this overarching hypothesis, the following specific sub-hypotheses are advanced:

- Distinct molecular sizes and geometric configurations give rise to characteristically different stability patterns and reactive surface sites, which directly modulate catalytic activity. In particular, the most stable isomers at each structures are expected to display unique active-site geometries that determine their interaction with NH_3 and its dehydrogenation intermediates.

- Spin state is a critical determinant of both the ground-state electronic structure and the relative energetics of reaction intermediates and transition states for small iron oxides. Spin-state crossings may occur along the reaction coordinate, potentially providing low-energy pathways that would not be accessible within a single-spin-state description.

- Automated reaction-pathway search techniques can reliably and systematically identify key reaction intermediates and transition states in NH_3 dehydrogenation on $(Fe_2O_3)_n$ non-nanosized structures, yielding a more complete and unbiased mechanistic picture that is attainable through conventional, manually guided approaches.

- The identification and analysis of rate-determining steps and activation energy barriers will enable the establishment of quantitative structure–activity relationships that provide actionable design principles for the rational development of efficient, earth-abundant iron-based nanocatalysts.

By rigorously testing these hypotheses through high-level quantum chemical calculations and systematic reaction-pathway analysis, this dissertation aims to bridge the current gap between fundamental theoretical understanding and the practical, knowledge-driven design of earth-abundant catalysts for sustainable hydrogen production.

3 Scope and objectives

The accelerating growth of global energy demand, in conjunction with the mounting environmental consequences of continued reliance on fossil fuels, has rendered the development of clean, sustainable energy technologies an urgent scientific and societal priority. Molecular hydrogen (H_2) occupies a central position in this landscape as a versatile energy carrier, owing to its exceptionally high gravimetric energy density and the fact that its combustion yields only water as a by-product, thereby circumventing the generation of greenhouse gas emissions at the point of use. Nevertheless, the practical realisation of a hydrogen-based energy economy is contingent upon the development of efficient, scalable, and economically viable hydrogen production pathways—a challenge that remains a defining problem in contemporary catalysis and materials science.

Electrocatalytic processes, most notably water splitting and ammonia (NH_3) decomposition, represent among the most promising routes to green hydrogen production. The overall efficiency and selectivity of these processes are critically dependent on the catalytic performance of the electrode materials employed. Noble metal-based catalysts—including platinum (Pt), palladium (Pd), and rhodium (Rh)—exhibit exceptional intrinsic activity; however, their global scarcity and prohibitive cost render large-scale deployment economically impractical. This constraint has motivated extensive research efforts directed toward the identification of earth-abundant alternatives capable of delivering competitive catalytic performance.

In this context, iron represents a particularly attractive candidate element: it is among the most abundant constituents of the Earth's crust, it is inexpensive, and its oxide phases exhibit intrinsically tunable structural and electronic properties. At the nanoscale, iron oxide molecules manifest emergent properties that differ qualitatively from those of the corresponding bulk phases. Catalytic activity in these systems is exquisitely sensitive to factors including molecule nuclearity, local atomic coordination environment, and spin state—parameters that are not independently controllable in

bulk materials but are, in principle, accessible as design variables in nanoparticle-based catalysts. Despite meaningful progress in the experimental characterisation of iron oxide nanostructures, a quantitative, atomistic-level understanding of how these variables collectively govern catalytic function remains lacking.

My dissertation is devoted to a systematic theoretical investigation of $(Fe_2O_3)_n$ structures spanning $n = 1$–10, employing a suite of computational chemistry methods. The work encompasses three interconnected themes: (I) a comprehensive structural exploration aimed at identifying and characterising low-energy isomers and quantifying size-dependent trends in stability; (II) a rigorous analysis of electronic structure and magnetic properties, with particular emphasis on the role of spin state in determining ground-state configurations and accessible reaction manifolds; and (III) an investigation of the catalytic behaviour of selected Fe(III) oxide structures ($n = 1$–4) in the NH_3 dehydrogenation reaction.

The catalytic studies employ state-of-the-art automated reaction-pathway search techniques to map the potential energy surfaces relevant to NH_3 dehydrogenation without reliance on manually proposed reaction mechanisms. This approach enables the unbiased identification of reaction intermediates, transition states, and competing reaction channels. Kinetic analysis, including the determination of activation energy barriers and rate-determining steps, is subsequently carried out to provide quantitative insight into reaction efficiency and selectivity. The overarching aim is to develop an integrated, atomistic-level picture of iron oxide nanoparticle chemistry that can inform the rational design of next-generation, earth-abundant catalysts for sustainable hydrogen production.

The main objectives of this dissertation are outlined as follows:

1. **Systematic Investigation of Structural Isomerism.**
   To identify and rigorously characterise the low-energy isomeric structures of $(Fe_2O_3)_n$ structures ($n = 1$–10) by combining conventional quantum chemical optimisation methods with automated global structure-search algorithms. This objective encompasses the analysis of how small molecular systems nuclearity and geometry influence thermodynamic stability and the nature of potentially reactive surface sites.

2. **Determination of Spin States and Electronic Structure.**
   To systematically determine the accessible spin states—encompassing low-spin, intermediate-spin, and high-spin configurations—of $(Fe_2O_3)_n$ moleculs for each

molecule size, and to establish the corresponding ground-state electronic structures. This analysis will quantitatively evaluate the extent to which spin state determines molecular stability and modulates reactivity.

3. **Benchmarking and Assessment of Computational Methodologies.**
   To perform structural optimisations and total energy calculations employing a range of density functional approximations and basis-set combinations, with the aim of rigorously benchmarking the consistency and reliability of the obtained results and identifying the most appropriate level of theory for each class of property investigated.

4. **Mechanistic Exploration of the NH_3 Dehydrogenation Reaction.**
   To investigate the detailed reaction mechanism of NH_3 dehydrogenation on representative $(Fe_2O_3)_n$ structures ($n = 1$–4) through the application of automated potential energy surface exploration techniques. This objective entails the systematic identification of all relevant reaction intermediates, transition states, and branching points, yielding a comprehensive mechanistic description that transcends what is accessible through conventional, hypothesis-driven approaches.

5. **Kinetic Analysis of Reaction Pathways.**
   To construct complete energy profiles for NH_3 dehydrogenation on each investigated size of Fe(III) oxide and to identify the rate-determining step(s) and associated activation barriers. This kinetic analysis will provide mechanistic insight into the factors that control the overall reaction rate and will enable a direct comparison of catalytic efficiency across different sizes of Fe(III) oxide.

6. **Establishment of Structure–Activity Relationships.**
   To establish quantitative correlations between structural features, electronic configuration, and spin state on the one hand, and catalytic performance on the other. The resulting structure–activity relationships are intended to provide general design principles for the rational development of efficient, earth-abundant iron oxide nanocatalysts for sustainable hydrogen production.

4 Electronic structure methods

The development of electronic structure theory has enabled us to fully understand the motion of electrons in atoms and molecules by applying quantum mechanical postulates. This revolutionary theoretical framework emerged in the early 20th century, fundamentally transforming my comprehension of matter at the atomic and molecular level. Nowadays, electronic structure theory methods are widely used among chemists and physicists to analyze the structures of chemical compounds and atoms with unprecedented accuracy and detail. These computational approaches have become indispensable tools for predicting molecular properties, reaction mechanisms, and thermodynamic parameters that would be difficult or impossible to measure experimentally. Moreover, electronic structure methods extend far beyond simple molecules and are extensively used to study crystal structures, surfaces, and solid-state materials. They provide crucial insights into electronic band structures, magnetic properties, and phase transitions in condensed matter systems. Modern applications include the design of new materials for energy storage, catalysis, and electronic devices. The field has evolved from simple approximations to highly sophisticated methods that can handle systems containing thousands of atoms. Key developments include density functional theory (DFT), coupled cluster methods, and multireference approaches, each offering different levels of accuracy and computational efficiency depending on the system under investigation. This chapter provides brief outlines of the early development and recent progress in electronic structure theory, tracing the journey from the initial quantum mechanical foundations laid by Schrödinger, Heisenberg, and others, to the cutting-edge computational methods that enable researchers today to model complex biological systems, design novel materials, and understand fundamental chemical processes at the quantum level.

4.1 Basic concepts and the Schrödinger equation

The starting point of electronic-structure theory is the time-independent Schrödinger equation, which for a stationary state takes the eigenvalue form

$$\hat{H}\psi = E\psi \tag{4.1}$$

The Hamiltonian operator $\hat{H}$ encodes the kinetic and potential energy contributions of a system, while its eigenfunctions ψ and eigenvalues E determine, respectively, the stationary states and their energies. Once $\hat{H}$ is specified and the eigenvalue problem is solved, the quantum-mechanical behaviour of the system is fully determined.

Analytical solutions of this equation exist only for a limited set of model systems, such as the hydrogen atom, the harmonic oscillator and the particle in a box. For many-electron systems no closed-form solution is available, and approximate, numerically tractable schemes must be introduced. The methods applied throughout this work are approximate solutions of the Schrödinger equation, and their accuracy, together with the situations in which they break down, follows directly from the approximations described in the following sections.

For a system of N electrons and M nuclei, the non-relativistic Hamiltonian is

$$\hat{H} = -\sum_{i=1}^{N} \frac{\hbar^2}{2m_e}\nabla_i^2 - \sum_{A=1}^{M} \frac{\hbar^2}{2M_A}\nabla_A^2 - \sum_{i=1}^{N}\sum_{A=1}^{M} \frac{Z_A e^2}{4\pi\epsilon_0 r_{iA}} + \sum_{i<j}^{N} \frac{e^2}{4\pi\epsilon_0 r_{ij}} + \sum_{A<B}^{M} \frac{Z_A Z_B e^2}{4\pi\epsilon_0 r_{AB}} \tag{4.2}$$

The individual terms have the following physical meaning:

- **Electronic kinetic energy**: $-\sum_{i=1}^{N} \frac{\hbar^2}{2m_e}\nabla_i^2$. This term is evaluated exactly.
- **Nuclear kinetic energy**: $-\sum_{A=1}^{M} \frac{\hbar^2}{2M_A}\nabla_A^2$. This term is removed under the Born-Oppenheimer approximation (Sec. **??**).
- **Electron-nuclear attraction**: $-\sum_{i=1}^{N}\sum_{A=1}^{M} \frac{Z_A e^2}{4\pi\epsilon_0 r_{iA}}$. This term is evaluated exactly and binds the electrons to the nuclei, driving chemical bonding.
- **Electron-electron repulsion**: $\sum_{i<j}^{N} \frac{e^2}{4\pi\epsilon_0 r_{ij}}$. This term couples the electronic coordinates and gives rise to electron correlation, and it constitutes the principal obstacle to an exact solution.
- **Nuclear-nuclear repulsion**: $\sum_{A<B}^{M} \frac{Z_A Z_B e^2}{4\pi\epsilon_0 r_{AB}}$. This term is constant for a fixed nuclear geometry.

The geometry of a diatomic molecule is fully specified once a coordinate origin is chosen and the positions of all particles, namely the two nuclei and the N electrons, are expressed as vectors from that origin. Figure 1 shows the standard set of coordinate vectors used in quantum-chemical treatments of diatomic systems.

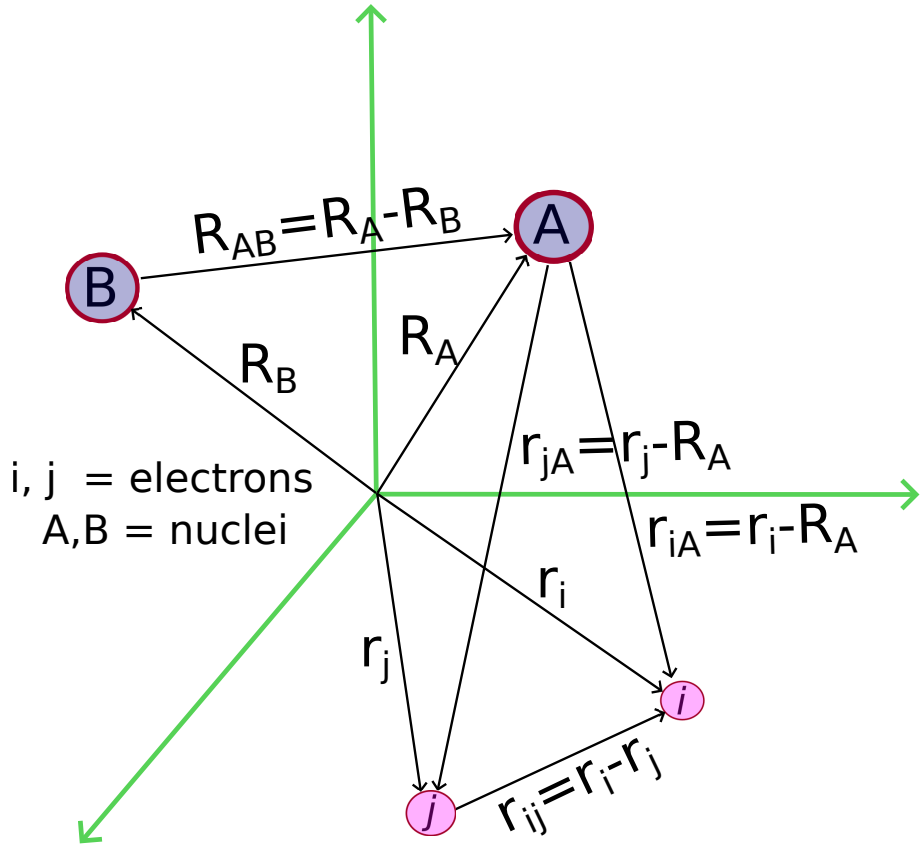


Figure 1. Molecular coordinate system for a diatomic molecule.

4.1.1 Restricted and unrestricted Hartree-Fock approximations

The Hartree–Fock (HF) method is the cornerstone of *ab initio* quantum chemistry. It approximates the many-electron wavefunction as a single Slater determinant and determines the optimal set of spin-orbitals by minimising the total electronic energy subject to the orthonormality constraint, leading to the canonical HF equations [69; 70]

$$\hat{f}(i)\,\chi_k(\mathbf{x}_i) \;=\; \varepsilon_k\,\chi_k(\mathbf{x}_i), \tag{4.3}$$

where $\hat{f}(i)$ is the one-electron Fock operator, χ_k are spin-orbitals, and ε_k are the corresponding orbital energies. In practice, the spin-orbitals are expanded in a finite atom-

centred basis set $\{\phi_\mu\}$, transforming Eq. (4.3) into the Roothaan–Hall matrix equations [71; 72]

$$\mathbf{F}\,\mathbf{C} \;=\; \mathbf{S}\,\mathbf{C}\,\boldsymbol{\varepsilon}, \tag{4.4}$$

where $\mathbf{F}$ is the Fock matrix, $\mathbf{C}$ the matrix of molecular orbital (MO) coefficients, $\mathbf{S}$ the overlap matrix, and $\boldsymbol{\varepsilon}$ the diagonal matrix of orbital energies. Two fundamentally different strategies for handling electron spin within this framework give rise to the *Restricted* (RHF) and *Unrestricted* (UHF) formulations.

In the Restricted Hartree–Fock approach, α- and β-spin electrons are forced to occupy *identical* spatial orbitals [71]. For a closed-shell system with N electrons occupying $N/2$ doubly-occupied orbitals ψ_k.

The constraint of equal spatial orbitals for both spins makes RHF the natural choice for closed-shell ground states of singlet multiplicity: atoms and molecules with filled valence shells such as H_2, H_2O, NH_3, and most organic molecules in their electronic ground states [69; 70; 73]. The method is computationally efficient and yields a wavefunction that is a true eigenfunction of the total spin operators $\hat{S}^2$ and $\hat{S}_z$ with $S = 0$.

One of the limitations of RHF is equal-orbital constraint becomes unphysical when bond dissociation is considered. The classic example is H_2: at stretched geometries the RHF wavefunction wrongly places equal probability on ionic (H+H-) and covalent (H.H.) configurations, leading to a well-known overestimate of the dissociation energy and a qualitatively incorrect potential energy surface [74; 75]. More generally, RHF fails whenever near-degeneracy or static correlation effects are important, such as in transition-metal complexes with partially filled d-shells, biradicals, or stretched/broken bonds.

The Unrestricted Hartree–Fock method, introduced by Pople and Nesbet [76], lifts the spatial-orbital constraint and allows α- and β-spin electrons to occupy *different* sets of spatial orbitals, $\{\psi_k^\alpha\}$ and $\{\psi_k^\beta\}$, respectively.

Addition of the orbital flexibility of UHF allows a better description of systems with unequal numbers of α and β electrons (open-shell radicals, triplet states) as well as bond-dissociation processes. For the stretched H_2 molecule, for instance, UHF correctly localises opposite spins on the two centres, recovering the proper homolytic dissociation limit [74; 75].

The principal drawback of UHF is that the wavefunction is no longer a pure eigenstate of $\hat{S}^2$; it is contaminated by higher-spin states. The expectation value

$$\langle \hat{S}^2 \rangle_{\mathrm{UHF}} = \frac{N^\alpha - N^\beta}{2}\left(\frac{N^\alpha - N^\beta}{2} + 1\right) + N^\beta - \sum_{k}^{N^\alpha}\sum_{l}^{N^\beta}\left|\langle \psi_k^\alpha | \psi_l^\beta \rangle\right|^2 \tag{4.5}$$

deviates from the pure-spin value $S(S+1)$ whenever the α and β spatial orbitals differ [69]. Significant spin contamination can corrupt computed properties such as hyperfine coupling constants, spin densities, and subsequent correlated energies obtained from Møller–Plesset perturbation theory or coupled cluster methods [77; 78]. Annihilation of the largest contaminant using the Lowdin projection operator partly restores spin purity and improves results for troublesome cases [75].

It is imortant to note that an alternative for open-shell systems that avoids spin contamination, the Restricted Open-Shell Hartree–Fock (ROHF) approach [79] enforces doubly-occupied closed-shell orbitals for the paired electrons while treating the unpaired electrons in singly-occupied orbitals. The resulting wavefunction is a genuine eigenfunction of $\hat{S}^2$, but the coupling between closed and open shells complicates the SCF equations and typically yields higher variational energies than UHF. ROHF is therefore preferred when a spin-pure reference is required for subsequent multi-reference treatments, for instance in complete active space (CASSCF) or internally contracted multireference CI (MRCI) calculations [80; 81].

The system containg metals like transition metal complexes or metal oxides with partially filled d-shells present one of the most demanding tests for HF-based methods. UHF can qualitatively capture the high-spin preference in mononuclear iron and manganese complexes through differential exchange-stabilisation of majority-spin d-orbitals, in agreement with ligand-field theory [82; 83]. However, the neglect of dynamic correlation in any HF variant leads to systematic errors in spin-state splittings and bond energies of metal–ligand bonds; hybrid DFT or correlated wavefunction methods are generally preferred for quantitative accuracy [84; 85].

4.2 Post-Hartree-Fock methods: Correlated methods

In quantum chemistry, finding an accurate approximate solution to the Schrödinger equation has been a great challenge. In HF approximations electron-electron repulsion is treated in an average way and therefore the total energy calculated from HF methods does not contain correlation energy. The correlation energy is rather small but it plays a crucial role in accurately describing chemical phenomena. The energy difference between energy found by the HF method within a given basis set which reaches the completeness (discussed in Section 4.4) and exact ground state energy is called electron

correlation energy

$$E_{corr} = E_0 - E_{HF}. \tag{4.6}$$

Since HF energy is an upper limit to the exact energy, the correlation energy is negative.

Post-HF methods are used to treat electron correlation. Some electron correlation methods are designed to recover the static part and dynamic part. Static electron correlation is associated with electrons occupying different spatial orbitals that electrons avoid each other. It is also called the near-degeneracy effect. Therefore, it becomes important in the system where energy levels degenerate. For example, in H_2 molecule at dissociation limit, the bonding and antibonding molecular orbitals become degenerate as a result it is absolutely static correlation.

On the other hand, dynamic correlation is associated with electrons occupying the same spatial orbitals. As an example, H_2 molecule at the equilibrium distance is purely dynamic but when the bond stretches further, it gradually changes to static.

4.2.1 Configuration Interaction

Configuration Interaction (CI) is one of the oldest correlated methods. In the CI method, the trial wave function is built based on the linear combination of Slater determinants those made of HF molecular orbitals. These determinants are formed when electrons are Singly, Doubly, Triply and so on excited. When the trail wave function includes all the possible excited determinants, it is called Full CI and it takes the form

$$|\Psi_{CI}\rangle = c_0|\Psi\rangle + \sum_{i}^{occ.}\sum_{r}^{vir.} c_i^r|\Psi_i^r\rangle + \sum_{i<j}^{occ}\sum_{r<s}^{vir.} c_{ij}^{rs}|\Psi_{ij}^{rs}\rangle + ... \tag{4.7}$$

In EQ. 4.7 the first term is the Hartree-Fock wave function used as a reference, and the second term is a singly excited determinant where we take one occupied orbital and replace it with virtual orbital, and the third term is doubly excited determinant where we take two occupied orbitals and replace them with two virtual orbitals and so on. It continues until we use all the occupied orbitals. The coefficient in front of wave functions in EQ. 4.7 is a CI coefficient and applying the variational principle we optimize the CI coefficient. Note that including all the possible excited determinants becomes inadequate because full CI expansion scales factorially. Therefore, in computational chemistry, it is only used for systems containing very few electrons.

There are several of ways to reduce the computational cost of CI calculations by taking only a few excited determinants. It is important to note that improvement in HF calculation can be made only by taking doubly excitation. Another way is instead

of taking all occupied electrons and all possible excitations, we can take the last few occupied orbitals and first few virtual orbitals around Highest Occupied Molecular Orbitals (HOMO) and Lowest Unoccupied Molecular Orbitals (LUMO). The general term for these calculation types is Multiconfiguration Self-Consistent Field (MCSCF).

4.2.2 Multi-Configurational Self-consistent field (MCSCF)

In MCSCF method, we can write wave function in CI form as a linear combination of Slater determinants or using Configuration state functions (CSF).

$$|\Psi_{MCSCF}\rangle = \sum_{i}^{CI} c_i |\Psi_i\rangle \tag{4.8}$$

where Ψ_i are (Singly, Doubly, et al.) excited Slater determinants or or CSFs. IF these determinants are selected based on the fact that all possible determinants within a given set of active orbitals as shown in Figure 2, we use the term Complete Active Space Self-Consistent-filed (CASSCF) wave function[86] or Full-optimized Reaction Space (FORS)[87; 88].

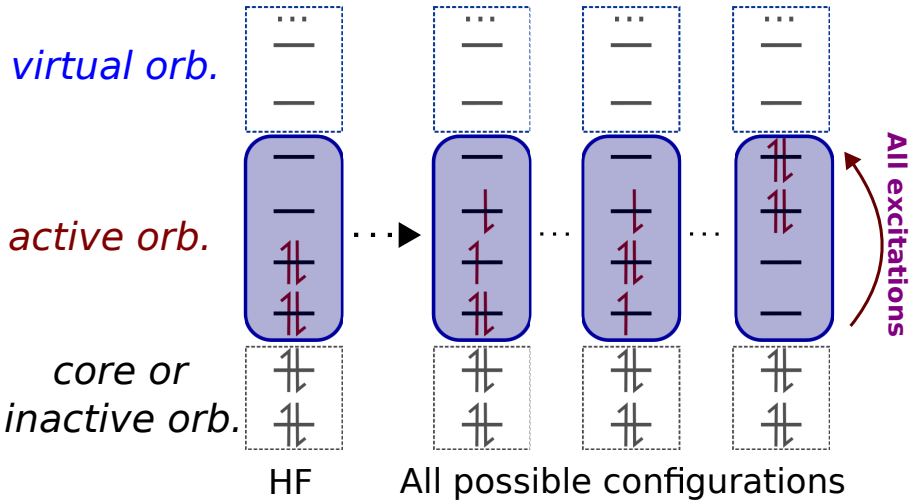


Figure 2. Construction of CASSCF configurations with 4 electrons in 4 orbitals up to all possible excitations.

Another variant of MCSCF method is restricted active space self-consistent field (RASSCF). These two CASSCF and RASSCF are widely used methods in bond breaking reactions. The first time J. Sears and D. Sherrill[89] reported on the choice of active space for the single and multiple bond-beaking reactions in *HF, CH_4,H_2O, N_2*. They had chosen three different active spaces 1:1, minimal min, valence val. For *HF* molecule 1:1 and val active spaces contains 8 electrons in 8 orbitals and 5 orbitals respectively,

min active space contains 2 electrons in the orbital participating bonding and its anti-bonding counterparts in specific symmetries. They have concluded that regadless of the active space choice, CASSCF efficiently captures the strong static correlation effects and gives qualitatively correct potential energy surface for bond-breaking reactions of *HF*, CH_4,H_2O, N_2 molecules.

Another widely used application of CASSCF and RASSCF is conical intersection reactions where single antisymmetric Slater determinant no longer enough to describe two potential energy surface degeneracy[90; 91; 92; 93; 94; 95].

MCSCF variants CASSCF and RASSCF are also widely applied for the systems containing metals or metal oxides[96; 97; 98; 99]. In this case, calculations are often performed by involving d-sell of the metal in the active space. For example, G. Drabek et al. studies spin-state energetics of metallocenes with various methods. CASSCF calculations were performed with different active spaces: 10 electrons in 10 orbitals and 12 orbitals (10,10), (10,12). Full review on the multiconfigurational method is provided by P. Szalay et al.[100].

The CASSCF methods are alo often performed with adding perturbation theory. These types of methods are called Complete Active Space Perturbation Theory CASPT method. Addition of perturbation theory methods captures the dynamic part of the electron correlation.

4.2.3 Second order Møller-Plesset Perturation theory

In the family of correlation methods the second-order Møller-Plesset theory MP2 plays an important role as a wavefunction-based electronic structure method[101]. In fact, it was the first correlated method in quantum chemistry that is computationally inexpensive as well as size-extensive. Generally, in perturbation theory the exact Hamiltonian H operator is approximated to a simpler Hamiltonian H_0 in order to make it soluble. The relation with exact H and approximated H_0 is given $H = H_0 + \lambda V$, where V is the difference between two Hamiltonian, and λ is a parameter between 1 and 0, which makes Hamiltonian exact when λ=1 and λ=0 is normal HF. By imposing this Hamiltonian operator into Schrödinger equation we get,

$$(H_0 + \lambda V)|\Psi\rangle = E|\Psi\rangle \tag{4.9}$$

where, energy and wavefunction considered as a power series in λ:

$$(H_0+\lambda V)(|\Psi^{(0)}\rangle+\lambda|\Psi^{(1)}\rangle+\lambda^2|\Psi^{(2)}\rangle+...) = (E^{(0)}+\lambda E^{(1)}+\lambda^2 E^{(2)}+...)(|\Psi^{(0)}\rangle+\lambda|\Psi^{(1)}\rangle+\lambda^2|\Psi^{(2)}\rangle+...) \tag{4.10}$$

Using EQ 4.10 we can dirive first order equation,

$$H_0|\Psi^{(1)}\rangle + V|\Psi^{(0)}\rangle = E^{(0)}|\Psi^1\rangle + E^{(1)}|\Psi^{(0)}\rangle \tag{4.11}$$

Then energy expression can be wirtten as

$$E^{(1)} = \langle\Psi^{(1)}|V|\Psi^{(1)}\rangle \tag{4.12}$$

and, then second order correction to the energy is given by

$$E^{(2)} = \sum_{n\neq 0} \frac{|\langle\Psi_n^{(0)}|V|\Psi^{(0)}\rangle|^2}{E^{(0)} - E_n^{(0)}} \tag{4.13}$$

Even though, affordable computational cost and popularity of this method, it fails miserably to correctly model strongly correlated systems and metalic systems. For instance, John M. Herbert and Martin Head-Gordon[102] studied accuracy and limitation of second-order many-body perturbation thoery for predicting vertical vertical detachment energy of $(H_2O)_n^-$ and $(HF)_n^-$. They investigated the comparison between the MP2 and other correlated method in particular coupled-cluster theory with nonitterative triples, CCSD(T). Their results shows that error in vertical electron detachment energy calculated by MP2 method, as a fraction of CCSD(T) values, reaches a limit of about -7% for $(H_2O)_n^-$ clusters with vertical detachment energy larger than 0.4 eV. Moreover, it has been found that MP2 method overestimates dispersion-driven interactions in some systems such as π-stacking complexes[103]. Despite these disadvantages of MP2 for some systems, it still plays important role in computational chemistry especially its spin-component-scaled variants for systems with strong spin-spin correlation effects[104].

4.3 Density Functional Theory methods

Among other approximation techniques Density Functional Theory (DFT) follows a fundamentally different and far more economical strategy, in place of the high-dimensional wavefunction it adopts the electron density, a function of only three spatial variables, as the central quantity from which all ground-state properties are to be extracted. This reorientation from wavefunction to density is what renders the theory tractable for systems ranging from small molecules to extended solids, and it underlies the standing of density functional theory as the most widely applied electronic-structure method in contemporary chemistry[105; 106].

Despite its popularity, the approximate character of all practical functionals gives rise to a number of well-documented and systematic deficiencies, the majority of which

can be traced to two related sources of error[107]. The delocalisation, or self-interaction, error arises because the spurious interaction of an electron with itself, introduced through the Hartree term, is not exactly cancelled by approximate exchange functionals. Its consequences include the unphysical spreading of electronic charge, underestimated reaction barriers, the incorrect dissociation of charged species, and systematically too-small band gaps in solids. The complementary static-correlation error compromises the treatment of stretched chemical bonds and of near-degenerate, multireference electronic situations. A further intrinsic limitation of semi-local functionals is their inability to reproduce long-range London dispersion interactions, a shortcoming now routinely mitigated by the addition of empirical or semi-empirical dispersion corrections such as the DFT-D schemes of Grimme and co-workers[108]. A more fundamental difficulty is that, unlike the systematically improvable hierarchy of correlated wavefunction methods, density functional theory offers no convergent sequence of approximations guaranteed to approach the exact result. The choice of functional therefore retains an empirical, application-dependent character, and results are prudently validated against experiment or high-level benchmark data.

4.4 Atomic centered basis functions

Here, I would like to discuss another important approximation in quantum chemistry. Basis sets are an approximation common to almost all quantum-chemical methods. The underlying idea is to expand the unknown functions, namely the molecular orbitals, in a set of known functions. Such an expansion would be exact only for a complete basis, that is, one containing an infinite number of functions. In practice the number of basis functions is finite, so the description of the electronic structure remains approximate. The molecular orbitals are accordingly written as linear combinations of atomic orbitals, which are themselves represented by Slater Type Orbitals (STOs) or Gaussian Type Orbitals (GTOs). The functional form of an STO is

$$\chi_{\zeta,n,l,m}(r,\theta,\phi) = NY_{l,m}(\theta,\phi)r^{n-1}e^{-\zeta r}, \tag{4.14}$$

where N is a normalisation constant and $Y_{l,m}$ are the spherical harmonics. The exponential dependence on the electron-nucleus distance reproduces the form of the exact orbitals of the hydrogen atom. The principal disadvantage of STOs is that the three-centre and four-centre two-electron integrals that arise cannot be evaluated analytically. In addition, a single STO has no radial nodes, so the nodal structure of the radial part must be recovered by taking linear combinations of STOs. STOs can therefore deliver

high accuracy for atomic and diatomic systems, and they are also suited to density-functional methods that omit exact exchange and that evaluate the Coulomb energy by fitting the density to a set of auxiliary functions.

The second type of function is the GTO, which may be written in polar or Cartesian coordinates as

$$\begin{aligned} \chi_{\zeta,n,l,m}((r,\theta,\phi)) &= NY_{l,m}(\theta,\phi)r^{2n-2-l}e^{-\zeta r^2} \\ \chi_{\zeta,l_x,l_y,l_z}(x,y,z) &= Nx^{l_x}y^{l_y}z^{l_z}e^{-\zeta r^2} \end{aligned} \tag{4.15}$$

An important distinction is that an STO possesses a cusp at the nucleus, whereas a GTO does not, so a single Gaussian represents the region close to the nucleus poorly. This deficiency is remedied by describing each atomic orbital as a linear combination of several GTOs.

Very accurate types of basis sets include Dunning-Huzinaga[109; 110; 111], Ahlrichs type[112; 113], atomic natural orbital[114], correlation consistent[115; 116] and polarization consistent[117] basis sets.

To accurately predict the structural properties of compounds, it is often necessary to employ large basis sets that include both diffuse and polarization functions. However, the use of such extensive basis sets can be computationally demanding, particularly for large systems or those containing multiple metal atoms. Therefore, it is important to choose a basis set that provides a good balance between accuracy and computational efficiency. This can be achieved through the use of pseudopotentials (PP) or effective core potentials (ECP), which replace the chemically inert core electrons with effective, nodeless potentials. These potentials are typically derived with scalar relativistic effects incorporated. A widely used example of such a basis set is LANL2DZ[118; 119; 120], which combines ECPs for heavy atoms with a double-zeta basis set for valence electrons.

The performance of various types of basis sets are discussed in results section.

5 Theoretical approaches for chemical reactivity

The broader view of the reactivity of chemical compounds can be perused by having detailed knowledge of the Potential Energy Surface (PES) that constructs the transferring the one chemical compound (reactants) to another chemical compound (product) having the lowest energy along this reaction path on the PES. The highest point along this path is called the transition state as shown in Figure. 3 and energy relative to the reactant determines rate of the chemical reaction within the Transition State Theory. Of course, chemical reactions involving the mass transfer or electron transfer do not occur through a single PES and except for diatomic molecules, PES become complex.

5.1 Transition state theory

Transition state theory is a semi-classical theory which has been widely used theory for calculating rate of the bimolecular chemical reactions occurring in gas phases and in the condensed phase. The assumption in TST is that molecules at transition state are in equilibrium with the reactant, then macroscopic rate constant can be expressed as

$$k_{rate} = \frac{kT}{h} exp[-\frac{\Delta G^{\ddagger}}{RT}] \tag{5.1}$$

where,

$$\Delta G^{\ddagger} = \Delta G_{TS} - \Delta G_{reactant} \tag{5.2}$$

It is important to note that TST expression detains only for molecules undergoing chemical reactions that pass from the reactant over the transition state (top of the hill) and continuous the path to form a product where no re-crossing occurs for a given temperature. Therefore, the calculated rate constant using EQ.5.1 is always the upper limit to the exact rate constant as shown in the black curve in Figure. 3. Of course, not all the chemical reaction follows this assumption, for example, chemical

reactions can take place at the energies below the transition state barrier height through quantum-mechanical tunneling. In this case, transmission coefficient (*k*) is introduced. The transmission coefficient is rather difficult to calculate, but it is usually close to one. For instance, reactions at low temperatures, the tunneling contribution becomes important, leading to (*k>1*). In contrast, re-crossing effect becomes most important at high temperatures, giving (*k<1*) which means error introduced by TST is less than a factor of 2.

In the case of unimolecular reactions, TST is also incorporated into the widely used Rice-Ramsperger-Kassel-Marcus (RRKM) theory. Unlike in TST, the assumption in RRKM theory rate is proportional to the number of ways of distributing the energy among the internal degrees (translation, rotation, and vibrational) of freedom of reactant.

5.2 Artificial Force Induced Reaction path search for exploring potential energy surface

As described in section 4 based upon the solution of Schrödinger equation under the Born-Oppenheier approximation we get a broader picture of chemical reaction as nuclei moving on the potential energy surface from one minima to another minima. However, except for diatomic molecules, the PES is more complex because of high dimensionality and there might be more than one possible pathway through which chemical reactions occur. Manually exploring chemical reactions for such complex reactions with quantum chemical methods is time-concuming, and exhaustive reaction pathway exploration is generally impractical and requires systematic approach. Artificial Force Induced Reaction (AFIR) technique is an automatic approach to exploring all relevant reaction pathways by perturbation of adiabatic PES of chemical reactions [121; 122; 123; 124].

The basic idea in the AFIR strategy (See Figure 3) is to push fragments (reactants) A and B of the whole system together or pull them apart by minimizing the following AFIR function [67]:

$$F(Q) = E(Q) + \alpha \frac{\sum_{i\in A}\sum_{i\in B}\omega_{ij} r_{ij}}{\sum_{i\in A}\sum_{i\in B}\omega_{ij}} \tag{5.3}$$

The external force term in Eq.(5.3) perturbs the given adiabatic Potential Energy Surface (PES), $E(Q)$, with geometrical parameters Q in the AFIR function. Here, α defines the strength of the artificial force which depends on the weighted sum of the interatomic distances r_{ij} between atoms i and j, with the weights ω_{ij} defined as

$$\omega_{ij} = \left[\frac{R_i + R_j}{r_{ij}}\right]^6, \tag{5.4}$$

where R_i and R_j the covalent radii of of atoms i and j, respectively. The force parameter α in Eq. (5.3) can be expressed as follows:

$$\alpha = \frac{\gamma}{\left[2^{-1/6} - (1+\sqrt{1+\gamma/\epsilon})^{-1/6}\right] R_0}, \tag{5.5}$$

where R_0 and ϵ are parameters corresponding to interatomic Lennard-Jones potentials, and parameter γ has a physical meaning of a collision energy.

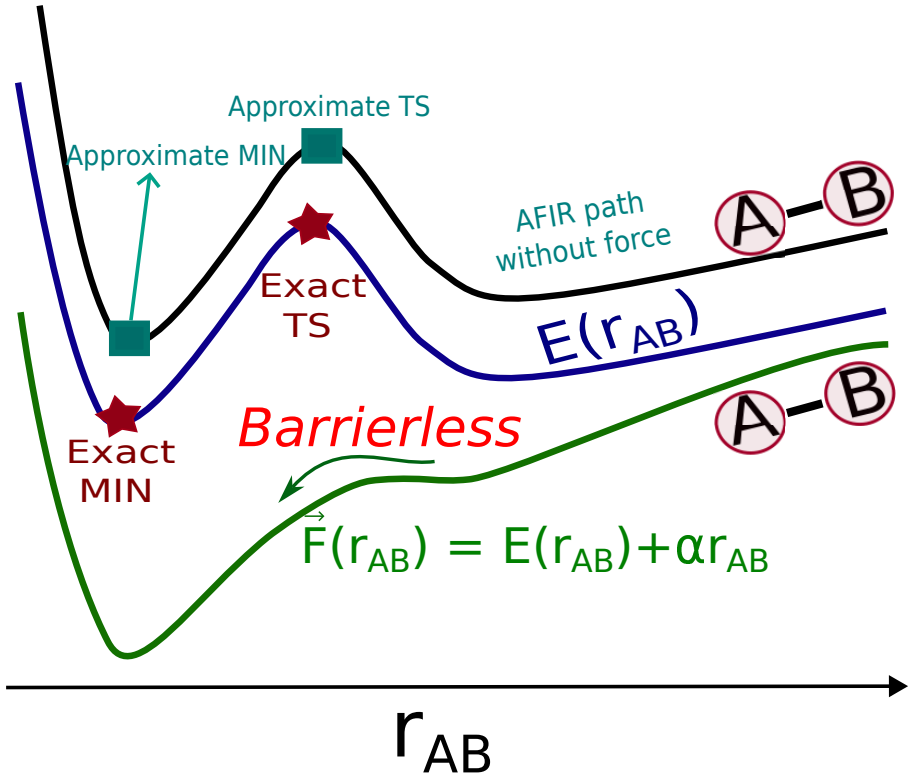


Figure 3. Potential energy surface of diatomic molecule E(r_{AB}). Dark blue true reaction coordinates, green AFIR path with artificial force and black shows AFIR without force. The figure adapted from reference [125]. Copyright © 2016 American Chemical Society

This perturbation of the PES facilitates the exploration of additional approximate transition states and local minima on the surface. The model collision energy parameter γ in Eq. (5.5) serves as an approximate upper limit for the barrier height that the system can be affected by the AFIR function [67]. The model collision energy parameter γ can be estimated based on the experimental conditions such as temperature (T), reaction time (t), rate constant (k) of a reaction from transition state theory expressed as in EQ. 5.1.

AFIR method has been extensively applied for studying full catalytic cycle, reactions involving transition metals, such as iron-catalzed cross-coupling reactions, iron-

catalyzed carbon-carbon bond formation and cobalt-catalyzed hydroformalation in aqueous solution and. In my research, AFIR method was applied for investigation of catalytic activity of Fe(III) oxide in ammonia decomposition for hydrogen production as shown in Figure 4. In this reaction pathway search collision energy parameter γ set to be 300 kJ/mol and artificial force applied whole system NH_3+Fe_2O_3. Then, desired reaction pathway on the PES can be reoptimized without without artificial force, employing the Locally Updated Plane (LUP) method.

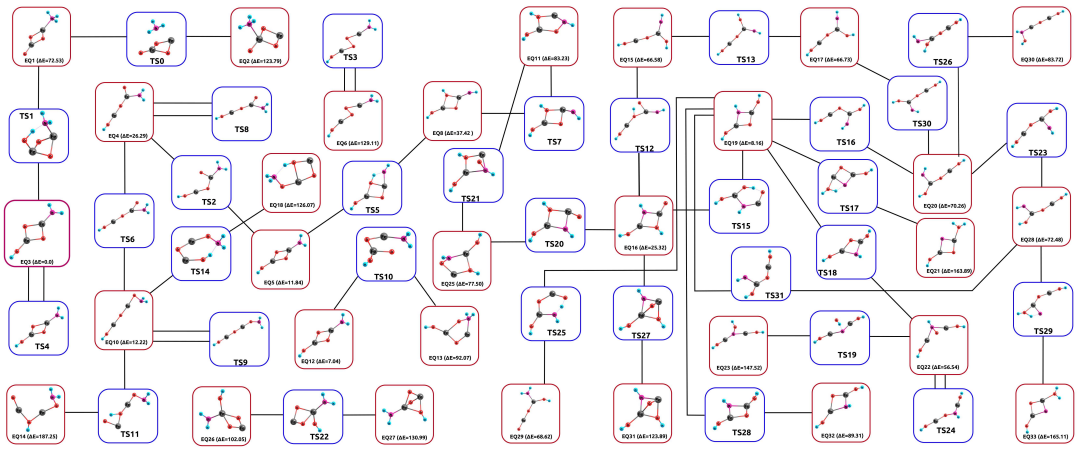


Figure 4. AFIR reaction pathways search for catalytic decomposition of NH_3 on the Fe_2O_3 molecule. Reaction Intermediates are shown in red squares and transition state structures are shown in blue squares.

5.3 Born-Haber cycle and derivation of standard redox potential

The redox reaction, or oxidation-reduction half-reaction, is fundamentally one of the most important reactions in chemistry, biology, materials science, and environmental chemistry. It is important that understanding the key chemical features of molecules that dictate reduction potential helps to tune the redox properties of compounds. Redox reactions can occur when an atom or molecule gains or loses an electron through a chemical reaction. An atom or molecule that loses the electron is called an oxidized or reducing agent. On the other hand, an atom or molecule that gains electrons is called a reduced or oxidizing agent. In this case, they restrain equal information on the free energy changes for electrochemical half-reactions. It is important to note that from a practical point of view, experimental measurement of the reduction potential for highly reactive species, such as radicals taking part in electrochemical reactions can be laborious. Therefore, the most alternative way of measuring reduction potential is to apply

computational chemistry methodologies which can be derived from thermochemical quantities described in Section 5.1. From a computational standpoint, standard reduction potential can be calculated from the thermodynamic cycle where solution-phase reduction Gibbs free energies are computed by taking the difference between gas-phase free energies and solvation free energies of the products and reactants at standard conditions. The theoretical calculation for reduction potentials is commonly performed for half-cell reaction (Figure. 5(A) and (B)) where two types of reduction half-cell reactions are shown. The corresponding reduction potential is

$$E^0 = \frac{\Delta G_{(red,solv)}}{nF} \tag{5.6}$$

Where,

$$\Delta G_{(red,solv)} = \Delta G_{red,(g)} + \Delta G^{III}_{solv} - \Delta G^{III}_{solv} \tag{5.7}$$

Then full-cell potential can be found by subtracting the reduction potential of the reference electrode such as Standard Hydrogen Electrode potential (SHE)[126].

$$E^0_{SHE} = E^0 - E_{SHE} \tag{5.8}$$

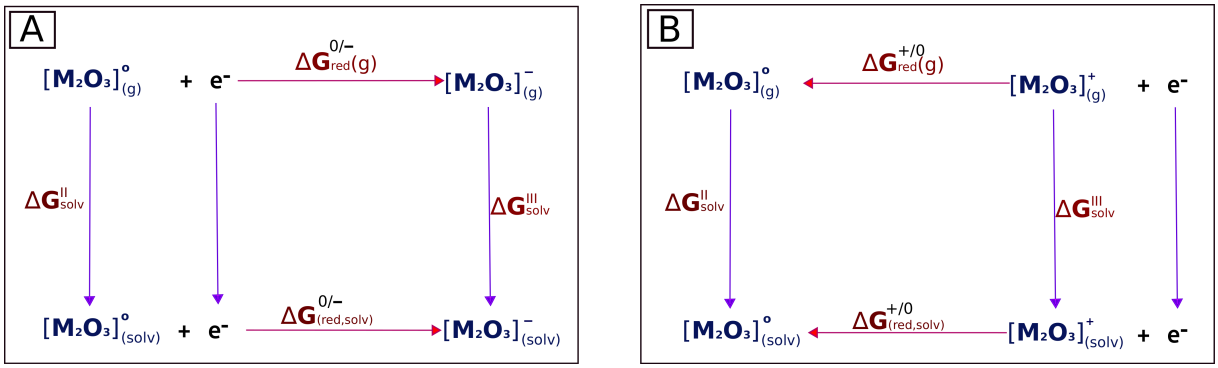


Figure 5. Born-Haber cycle adapted for 2 kind of one-electron reduction reactions.

The Gibbs free energy change of the gas-phase reaction shown in Figure 5 A, and B are adiabatic electron affinities (aEA) of $[M_2O_3]^0$ and $[M_2O_3]^+$, plus thermal contribution to the Gibbs free energy (ΔG_{therm}). The corresponding aEA can be written as:

$$aEA = E([M_2O_3]^0) + ZPE([M_2O_3]^0) - E([M_2O_3]^- - ZPE([M_2O_3]^-) \tag{5.9}$$

where E denotes the electronic energy (Born-Oppenheimer equilibrium potential energy), ZPE denotes the vibrational zero point energy. Electronic energies of the reaction

can be calculated by using chemically accurate methods such as Configuration Interaction, Multi-Configurational Self-Consistent field for smaller molecules only and Kohn-Sham density function theory methods described in section 4. Then the Gibbs free energy change in gas-phase can be expressed as:

$$\Delta G_{red,(g)} = G([M_2O_3]^0) - G([M_2O_3]^-) = aEA + [\Delta G_{therm}([M_2O_3]^0) - \Delta G_{therm}([M_2O_3]^-)] \tag{5.10}$$

where thermal contribution (ΔG_{therm}) includes free energy due to possible rearrangement, vibrational, rotation, an electronic excitations.

The second part of the Born-Haber cycle is to compute the free energy of solvation given in EQ. 5.11.

$$\Delta G_{solv} = G_{solv}([M_2O_3]^0) - E([M_2O_3]^0) \tag{5.11}$$

Accurate prediction of solvation free energies remains a major challenge in computational chemistry, motivating the development of various solvation models. Among these, continuum solvent models[127; 128; 129; 130] are the most widely employed in quantum chemical calculations because they provide an efficient balance between accuracy and computational cost. In these approaches, the solvent is represented as a homogeneous dielectric continuum, while the solute is placed inside a molecular-shaped cavity.

The Polarizable Continuum Model (PCM) is one of the most extensively used implicit solvation approaches and includes both the dielectric PCM (D-PCM) and the conductor-like[131] PCM (C-PCM). Although both methods are computationally efficient, their accuracy depends on the chemical system under investigation. For example, continuum models are generally less reliable for metal complexes with open coordination sites because they cannot explicitly represent the first solvation shell. Compared with D-PCM, C-PCM often provides improved electrostatic descriptions by approximating the solvent as a perfect conductor[127], thereby modifying the electrostatic boundary conditions. In my dissertation, solvation free energies (Figure. 5) were calculated using the PCM approach, and the corresponding results are presented in Section.6.

6 Results

6.1 Electronic structures of Fe(III) oxide

I began my study with the smallest possible stoichiometric structure of $(Fe_2O_3)_n$, namely the case of $n = 1$. Although several authors have asserted that there exists only a single stable state (defined by a specific geometry and spin multiplicity) for ferric oxide molecules [31; 32; 33; 34; 132], I initiated my exploration by considering multiple hypothetically plausible spin states, as previously explained, and by constructing geometries of diverse forms

During this process, I quickly encountered an important issue: at certain levels of theory, some configurations were simply not accessible and outcome that was neither systematic nor predictable. This observation compelled me to approach the investigation more analytically, which significantly increased the complexity of the study. As a result, my aim extended beyond merely identifying a single stable structure for iron trioxide; my thought to understand the mutual relationships between various states, assess the reliability and limitations of the computational methods used, and provide guidance for constructing and analyzing larger $(Fe_2O_3)_n$ molecules, for which high-level theoretical treatments are not yet computationally feasible.

For this reason, I also critically re-examined the existing literature on $(Fe_2O_3)_n$ molecules structure predictions. In the following chapters, I will demonstrate that presupposing a unique spin state and geometry for a given n is not a valid approach. This conclusion becomes even more evident when symmetry constraints whether imposed on molecules or extended crystal systems are applied via predefined coordinate systems.

In summary, the only rigorous approach for investigating possible states of $(Fe_2O_3)_n$ molecules are to systematically construct geometries "manually," assign different spin states and charges, and explore all feasible configurations. For larger molecules, this process becomes increasingly demanding and time-consuming. It is therefore essential

that research continues into the applicability of various electronic-structure methods to eventually identify a set of computationally affordable yet reasonably accurate techniques for modeling the states of transition metal oxides.

6.1.1 $(Fe_2O_3)_1$

For the smallest possible structure of Fe(III) oxide, I employed high levels of theory with a large basis set. The results presented in this section were recently published [133], where I investigated the electronic structures of Iron(III) and Cobalt(III) oxide isomers along with their redox properties.

The molecular structures of the UB3LYP/aug−cc−pVTZ–optimized local minima of the lowest-energy states are shown in Figures 6 and 7. Geometric parameters are presented in greater detail in Figure 8. Both nonmagnetic and antiferromagnetic singlet states were considered. Not all spin states of neutral molecules were attainable; this depended on the method employed. For instance, when using the DFT method, all spin states of iron and cobalt trioxides were stable, whereas with the MP2 method, spindle configurations of both oxides were only accessible for certain imposed spins. For cobalt oxide, this limitation extended to the linear configuration as well. Furthermore, not all geometry types yielded stable cationic and anionic states. Following a one-electron reduction or oxidation, neutral isomers frequently underwent breaking of one or two Me–O bonds, converting into different isomers depending on the system spin. Some isomers also underwent geometry changes upon spin state alteration or after redox reactions. The originally linear iron trioxide molecule became bent, and after one-electron oxidation with subsequent geometry optimization, it bent further (see Figure 6).

Since many states of Fe_2O_3 and Co_2O_3 contain unpaired electrons in their outermost shells and owing to their generally high-spin or antiferromagnetic character, I performed all computations using spin-unrestricted Hartree–Fock (UHF) wave functions. Furthermore, the DODS approximation naturally yields an antiferromagnetic state, which by definition corresponds to the singlet open-shell state. Although UHF wave functions are not eigenfunctions of the spin-squared operator $\hat{S}^2$, they can formally be expanded in terms of pure spin states of higher multiplicities. UHF eigenfunctions offer a notable advantage over restricted open-shell HF (R(O)HF) wave functions, particularly in accurately describing bond dissociation energies and spin densities in open-shell systems. Therefore, I applied MP2 and DFT methods in conjunction with UHF reference wave functions, in which the unperturbed Hamiltonian and Kohn–Sham

operators are expressed as sums of the spin-up (α) and spin-down (β) Fock operators, which reflects spin contamination. However, the ground-state structures of $Fe_2O_3^{(0,+1,-1)}$ and $Co_2O_3^{(0,+1,-1)}$ obtained with the UMP2 and UB3LYP methods exhibit only modest spin contamination. The largest spin contamination was observed for antiferromagnetic configurations. Since spin contamination can lead to erroneous conclusions in specific cases, I performed additional calculations using restricted Kohn–Sham orbitals and the BHHLYP exchange-correlation functional, which has been recently validated for computing redox properties [134]. States obtained by RBHHLYP are free of spin contamination but cannot describe antiferromagnetic configurations. Thus, I obtained all plausible ferromagnetic and non-magnetic states for the three iron trioxide isomers and compared their energies. The restricted BHHLYP/aug−cc−pVTZ energy charts as a function of spin clearly indicate that iron trioxide isomers prefer higher spin states, while low-spin states, including the nonmagnetic ($S = 0$) state, have substantially higher energies. Similar conclusions follow from unrestricted DFT and MP2 computations, with the antiferromagnetic singlet state having lower energy than both the nonmagnetic and some ferromagnetic states.

The linear (straight or bent) geometries of Fe_2O_3 and Co_2O_3 have not been proposed previously; some authors have even suggested that only a single possible state exists (in terms of both structure and spin) for ferric oxide [31; 32; 33; 34; 132]. However, the situation is likely more complex, and no rigorous, comprehensive description of the relationships among geometry, spin, and charge currently exists. Earlier attempts were often based on oversimplified assumptions, considering only one type of structure, restricting the range of spins explored, and applying unnecessary symmetry constraints, thereby limiting the set of hypothetical configurations. The possible combinations of geometries, spins, and charges are evidently numerous, and their complexity grows with particle size $(Me_2O_3)_n$, where Me denotes a metal atom and n an integer. Identifying the lowest-energy state (in terms of both geometry and spin) is essential for accurately determining physical properties and for studying chemical reactions. It is equally important to compare antiferromagnetic and ferromagnetic states, given the large number of spin combinations possible in transition metal oxides. I therefore considered a broader set of plausible spins for all configurations of neutral iron and cobalt trioxides and computed their energies (Figures 9 and 10). At both the DFT level with the B3LYP functional and at the MP2 level, I also considered antiferromagnetic electronic configurations for all iron(III) and cobalt(III) oxide isomers, including their ionic variants (Figures 11, 12, 13 and 14). Antiferromagnetic configurations were also maintained

following redox reactions. The optimized ionic geometries are summarized in Figures 6 and 7.

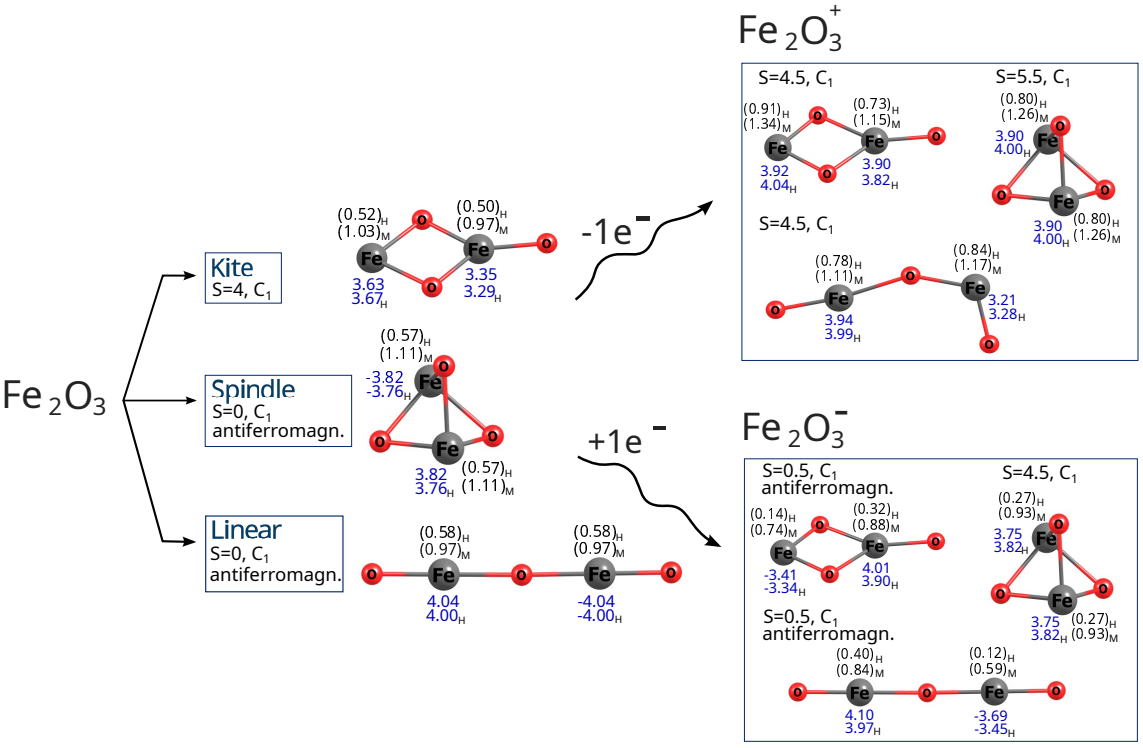


Figure 6. Molecular structures of UB3LYP/aug−cc−pVTZ optimized lowest-energy states of iron trioxides and the corresponding cations and anions. Total spins (S) are shown for each optimized state. No symmetry was imposed on the geometry. The structures were optimized in vacuum. Mulliken (M) and Hirshfeld (H) partial charges are shown in parentheses for the iron atom. Spin density values are shown in blue. If a given lowest-energy state among all those considered was characterized by an antiferromagnetic arrangement of spins, this is indicated in the drawing.

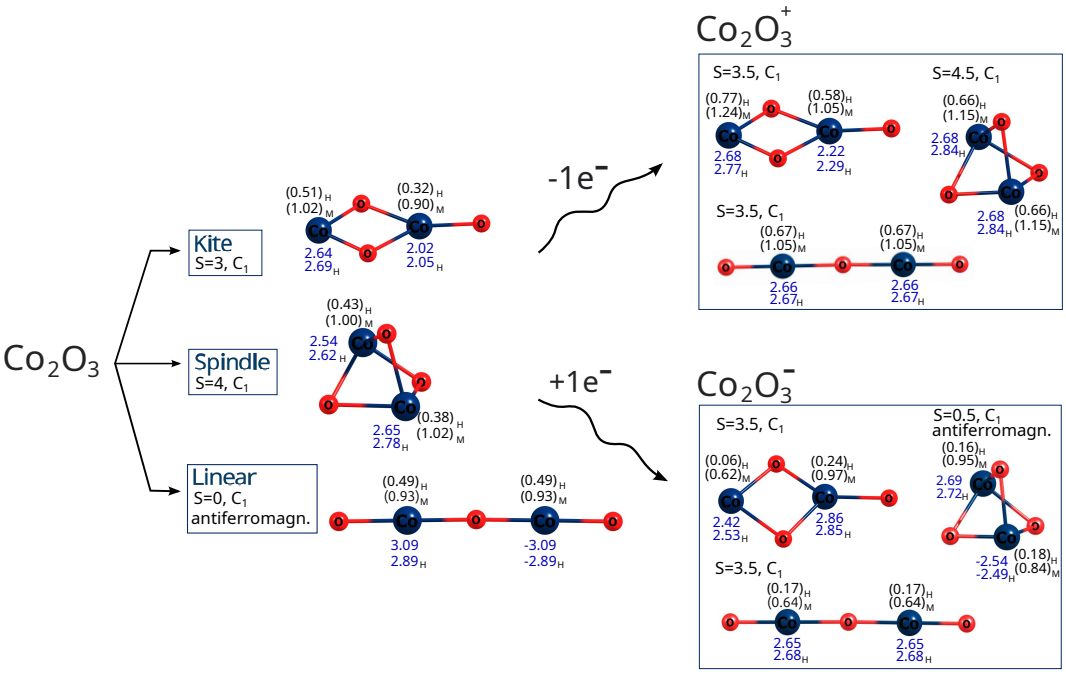


Figure 7. Molecular structures of UB3LYP/aug−cc−pVTZ optimized lowest-energy states of cobalt trioxides and the corresponding cations and anions. Total spins (S) are shown for each optimized state. No symmetry was imposed on the geometry. The structures were optimized in a vacuum. Mulliken (M) and Hirshfeld (H) partial charges are shown in parentheses for the cobalt atom. Spin density values are shown in blue. If a given lowest-energy state among all those considered was characterized by an antiferromagnetic arrangement of spins, this is indicated in the drawing.

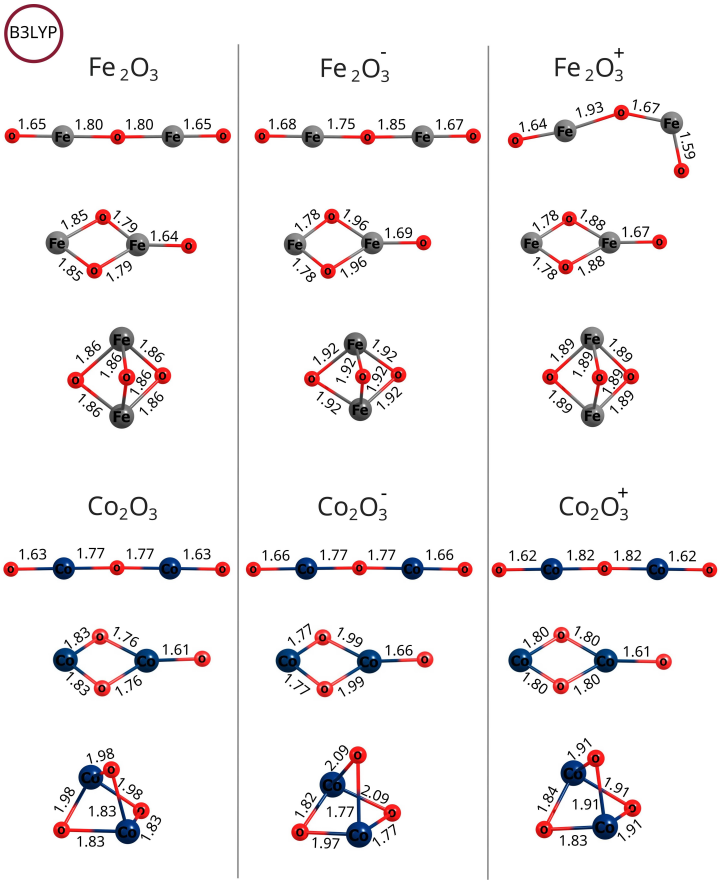
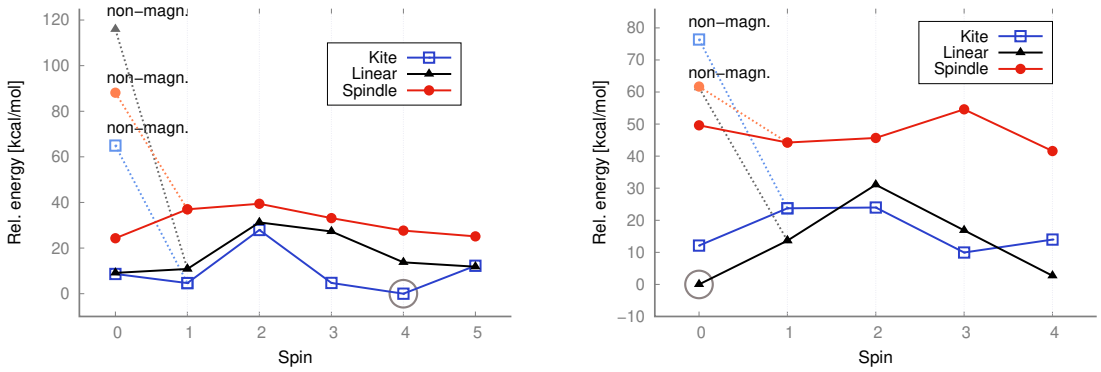
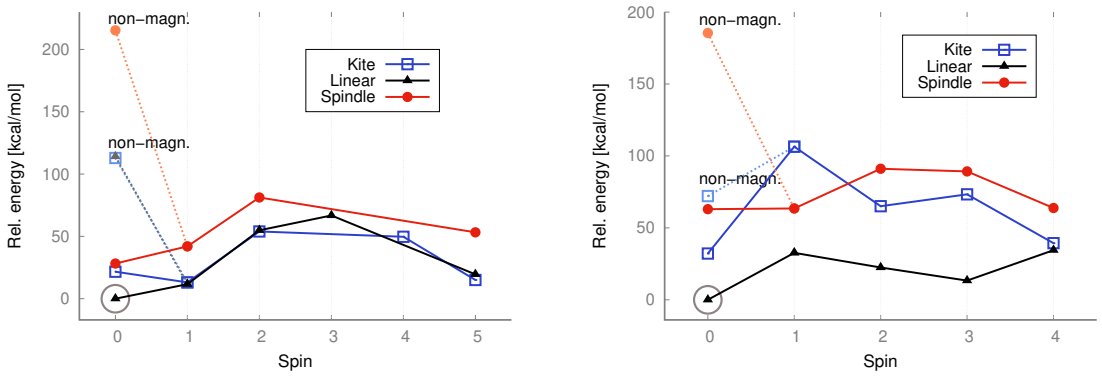


Figure 8. Bond lengths (Å) of the lowest-energy configurations of iron(III) and cobalt(III) oxides found at the UB3LYP/aug−cc−pVTZ level of theory.



(a) Neutral Fe_2O_3 (b) Neutral Co_2O_3

Figure 9. UB3LYP/aug−cc−pVTZ relative energies [kcal/mol] calculated with respect to the lowest-energy state of kite iron trioxide ($S = 4$) and linear cobalt trioxide ($S = 0$; antiferromagnetic conf.), respectively. The energies of both singlet states with non-magnetic (non-magn.) and antiferromagnetic configurations were taken into account. The lowest energy is marked with a circle.



(a) Neutral Fe_2O_3 (b) Neutral Co_2O_3

Figure 10. UMP2/aug−cc−pVTZ relative energies [kcal/mol] calculated with respect to the lowest-energy anti-ferromagnetic singlet ($S = 0$) state of the linear iron and cobalt trioxide, respectively. Non-magnetic singlet states are marked in a lighter color. The lowest energy is marked with a circle.

As revealed by the DFT computations, the lowest-energy neutral iron trioxide is a kite-shaped nonet, ferromagnetic structure. This result differs from that obtained by Sierka et al. [31; 32], who argued that the lowest-energy iron trioxide should be a kite structure with zero total spin and an antiferromagnetic electronic configuration. The singlet antiferromagnetic state of kite Fe_2O_3 lies approximately 10 kcal/mol higher in energy than the nonet. Examining the energy diagrams (Figures 9 and 10) more closely, it becomes evident that the isomers correspond to high open-shell singlets (antiferromagnetic) or high-spin ferromagnetic states. The non-magnetic singlet state is consistently much higher in energy than the lowest-energy spin state; in many cases, non-magnetic singlet states are the highest in energy altogether. Additionally, the linear isomer in its antiferromagnetic configuration has energy comparable to that of the antiferromagnetic kite. As observed in Figure 9, the highest-spin state of iron trioxide may be either a linear straight isomer or a kite structure, since their energies are nearly equal (see Figure 10). Notably, linear structures had not been considered in prior work; my computations show that this isomer exists in a very stable high-spin state, and its antiferromagnetic configuration is likewise highly stable. When using the B3LYP/aug−cc−pVTZ method, its energy was only approximately 10 kcal/mol above that of the nonet kite structure. The MP2 computations, however, indicate that the linear straight isomer corresponds to an antiferromagnetic singlet. The spindle-like structure, which is the most compact among the smallest iron trioxides (having the greatest number of iron–oxygen bonds), is consistently the highest in energy relative to the other isomers, for both antiferromagnetic and ferromagnetic electron configurations. Importantly, optimized structures

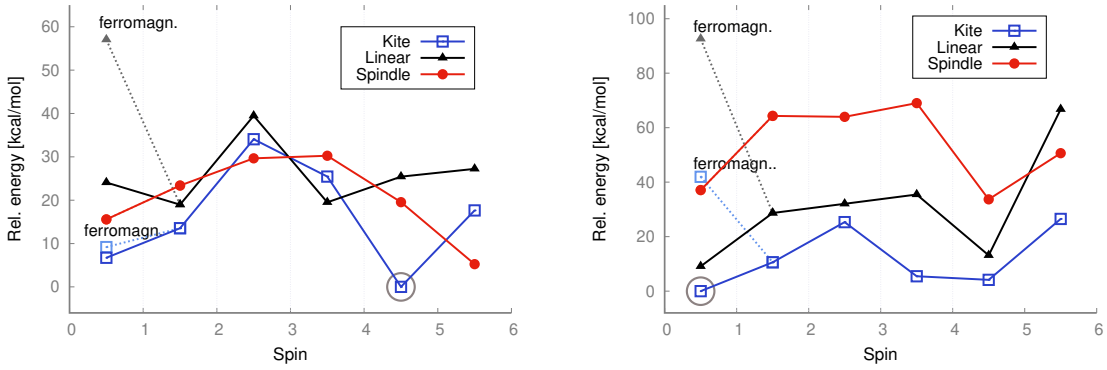
could be obtained at each level of theory for every imposed spin. It is worth noting that the spindle iron trioxide was also observed in optimized structures at the interface of α– and ϵ–Fe_2O_3 in the work of Ahamed et al. [135]. Although the energy of this structural type at the B3LYP level is relatively higher than that of the kite-like or linear straight structure, it should not be excluded from the pool of possible iron trioxide isomers; its antiferromagnetic singlet state is in fact a relatively low-energy configuration. The energy charts as a function of spin show that all isomers prefer higher spins or antiferromagnetic singlet states. In summary, both cobalt and iron oxides tend to favor either antiferromagnetic singlets or, conversely, high and very high spin states. Formally, a spin of 4 or 5 corresponds to 8 or 10 singly occupied molecular orbitals, respectively. This suggests that larger stoichiometric units of iron and cobalt trioxides are likely to adopt very high-spin states or antiferromagnetic singlets, irrespective of their spatial configuration. In general, this implies that metal oxide systems possess a very large number of singly occupied orbitals, with either a high or low spin (antiferromagnetic configuration). The definitive configuration of a metal trioxide, regardless of size, is rigorously connected to the mechanism of compound synthesis. As noted previously, many such methods involve wet synthesis starting from aqueous metal salt solutions and requiring relatively high-temperature treatment. The mechanisms of oxide synthesis from salts are olation and oxolation, as proposed in earlier experimental work [16; 17]. Given the lack of precise information on the configuration of products, intermediates, and byproducts, as well as their spin configurations during olation or oxolation, a comprehensive investigation of the complete reaction pathway (from salts to oxides), including solvent and pH effects, is essential. Possible spin-flipping transitions should also be considered. A thorough analysis of all conceivable spatial and spin configurations, together with their respective ionic forms, is therefore fundamental, and may enable a well-grounded interpolation of properties starting from the smallest possible configurations.

In the case of cobalt oxide, both DFT and MP2 calculations lead to the same conclusion: the lowest-energy isomer is the antiferromagnetic linear singlet. However, the ferromagnetic nonet (linear isomer) has an almost identical energy. Similarly to iron oxide, the spindle isomer of cobalt oxide — i.e., the one with the greatest number of bonds (exclusively oxide bridges, with no terminal oxygen atoms) — is the highest-energy one.

In the case of anions and cations of Fe_2O_3 and Co_2O_3, the situation is only slightly different; see the charts in Figures 11 and 13.

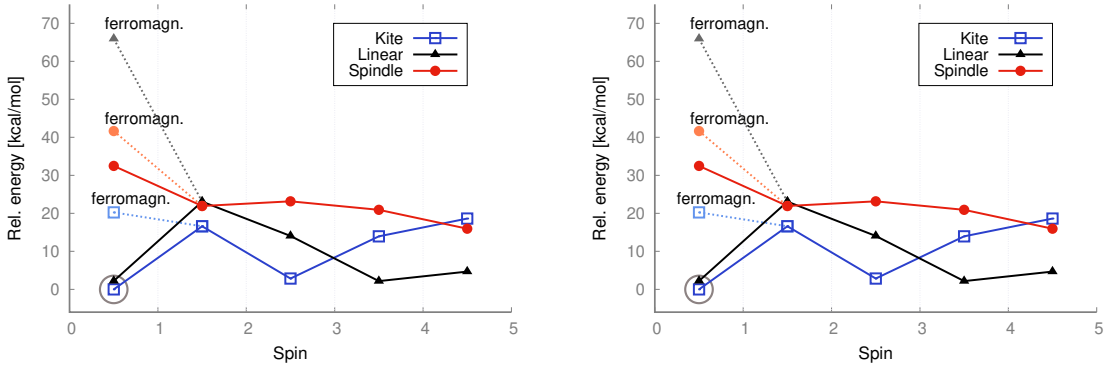
As revealed by the DFT computations, the lowest-energy anions and cations of both

iron trioxide and cobalt trioxide correspond to the kite-shaped isomer with a spin of $1/2$ (doublet state); the MP2 computations yield the same conclusion. Antiferromagnetic configurations were preserved during the redox reactions. After one-electron reduction (electron donation), the corresponding antiferromagnetic singlet states converted into doublet states retaining a partial antiferromagnetic electronic configuration. However, the ferromagnetic dectet ($S = 9/2$) kite lies only a few kcal/mol higher in energy. In contrast, one-electron oxidation does not lead to a change in geometry type or electronic configuration; the resulting product is a ferromagnetic dectet. For the spindle isomer, energies are generally the highest among all other cationic and anionic isomers. Furthermore, since the DFT/B3LYP computations identify the kite-like isomer as the lowest-energy neutral iron trioxide, one can expect that after one-electron reduction, no Fe–O bonds break, while the electronic configuration becomes more antiferromagnetic (shifting from the ferromagnetic nonet to the antiferromagnetic doublet). It must be emphasized that for the ionic species, all spin states were accessible for all isomers, just as in the neutral case. In other words, all isomers can undergo reduction or oxidation. Moreover, as shown by both MP2 and DFT computations, the linear isomer is very stable and is, in general, only a few kcal/mol higher in energy than the corresponding spin states of the kite-shaped Fe_2O_3 isomer. It can also be seen that some $Fe_2O_3^+$ isomers favor higher spin states to a greater degree than the respective $Fe_2O_3^-$ isomers. For anions and cations of cobalt oxides, the situation is similar (see the charts in Figures 11 and 13). Here as well, the cations prefer larger spins, although the energy differences are not as pronounced as in the case of neutral iron trioxides. For Co_2O_3 anions, the most stable form is the linear antiferromagnetic doublet at the MP2 level, or the antiferromagnetic kite at the DFT level; however, the energies of both the linear and kite isomers are nearly the same.



(a) $Fe_2O_3^+$ (b) $Fe_2O_3^-$

Figure 11. DFT UB3LYP/aug−cc−pVTZ relative energies [kcal/mol] calculated with respect to the lowest-energy state of ferromagnetic cation ($S = 4.5$) or anion ($S = 1/2$, including antiferromagnetic conf.) of a kite iron trioxide, respectively. The energies of both doublet states—with ferromagnetic (ferromagn.) and antiferromagnetic configurations—were taken into account. The lowest energy is marked with a circle.



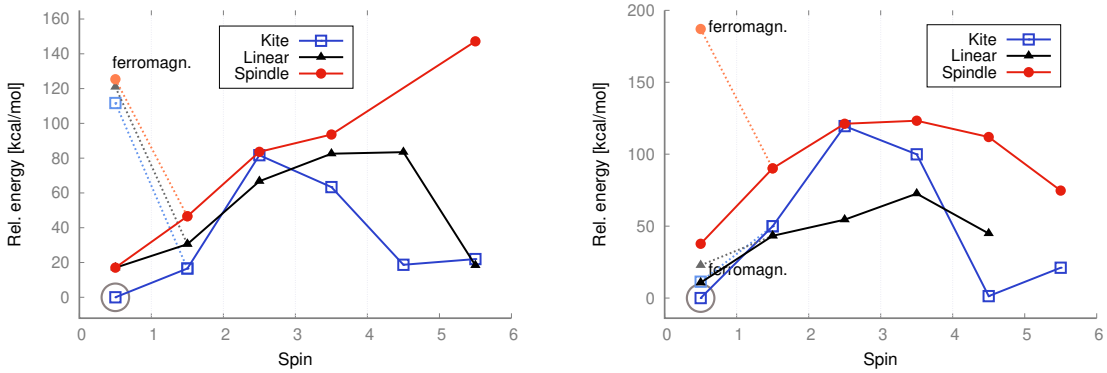
(a) $Co_2O_3^+$ (b) $Co_2O_3^-$

Figure 12. DFT UB3LYP/aug−cc−pVTZ relative energies [kcal/mol] calculated with respect to the lowest-energy doublet state ($S = 1/2$, including antiferromagnetic conf.) of the cation and anion of a kite cobalt trioxide, respectively. The energies of both doublet states—with ferromagnetic (ferromagn.) and antiferromagnetic configurations—were taken into account. The lowest energy is marked with a circle.

In addition, when a one-electron reduction or oxidation process occurs for neutral cobalt trioxide, the geometry remains linear, as established at both the DFT and MP2 levels of theory. The geometry of the linear Co_2O_3 isomer becomes bent after both oxidation and reduction.

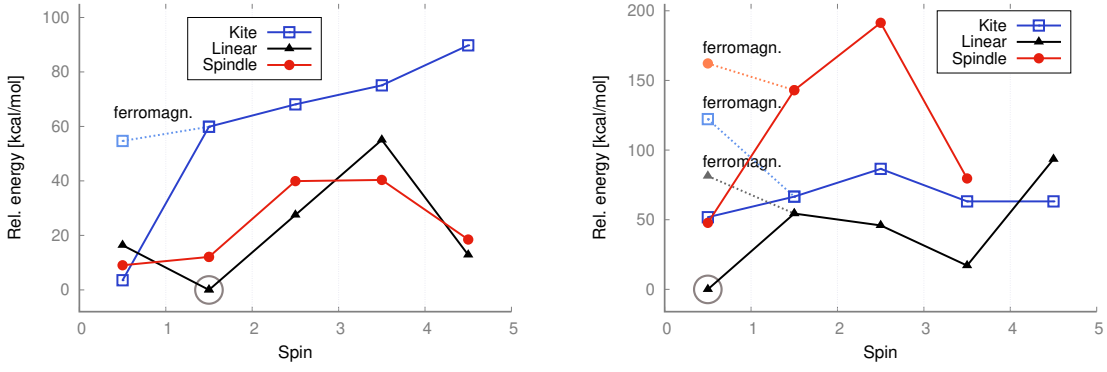
Comparing the geometries of the iron oxide isomers—see Figures 8 and 15—it is clear that B3LYP-level calculations generally yield a bent uncharged and cationic linear isomer, while MP2 optimization produces straightened linear systems. At both levels

of theory, the bonds to the terminal oxygen atoms are the shortest. The kite and spindle structures of iron oxide are similar for both neutral and ionic systems, though bonds in the anions are slightly elongated and in the cations slightly shortened.



(a) $Fe_2O_3^+$ (b) $Fe_2O_3^-$

Figure 13. UMP2/aug−cc−pVTZ relative energies [kcal/mol] calculated with respect to the lowest-energy anti-ferromagnetic doublet ($S = 1/2$) state of the kite iron trioxide. Ferromagnetic (ferromagn.) doublet states are marked in lighter color. The lowest energy is marked with a circle.



(a) $Co_2O_3^+$ (b) $Co_2O_3^-$

Figure 14. UMP2/aug−cc−pVTZ relative energies [kcal/mol] calculated with respect to the lowest-energy anti-ferromagnetic quartet ($S = 3/2$; cation) and anti-ferromagnetic doublet ($S = 1/2$; anion) states of the linear cobalt trioxide. Ferromagnetic doublet states are marked in lighter color. The lowest energy is marked with a circle.

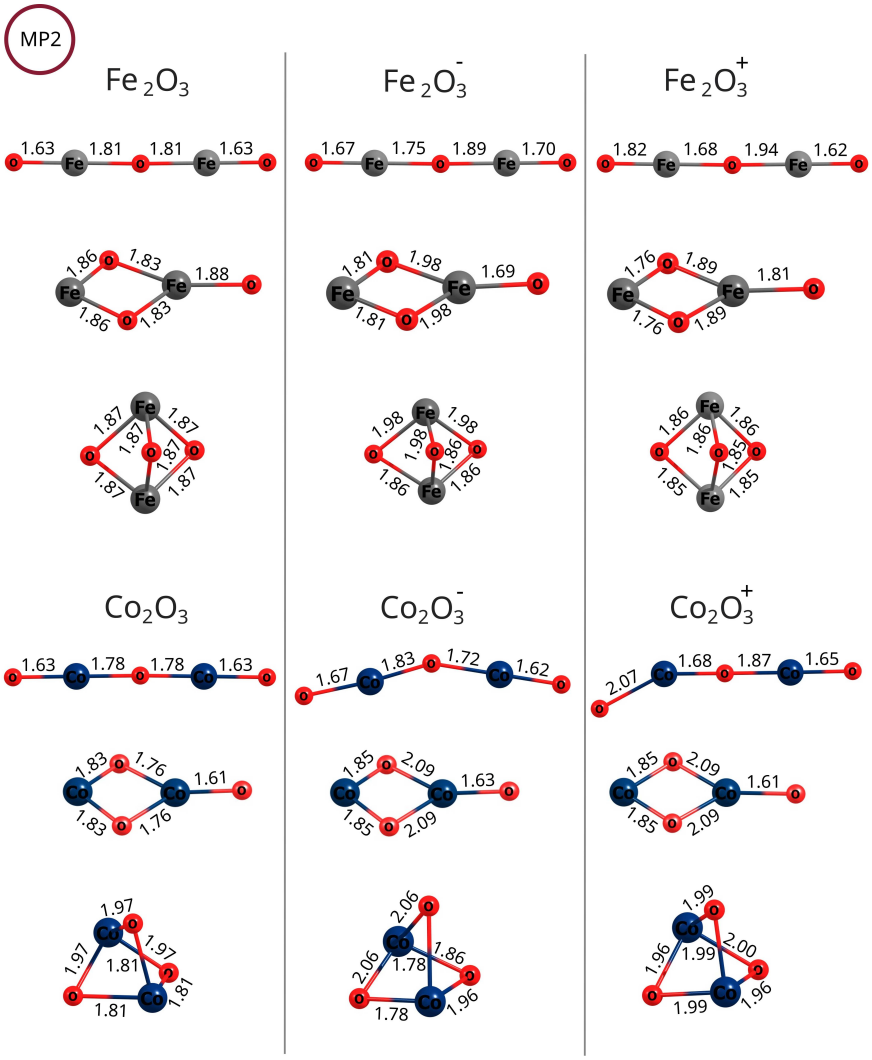


Figure 15. Bond lengths (Å) of the lowest-energy configurations of iron(III) and cobalt(III) oxides found at the UMP2/aug−cc−pVTZ level of theory. Antiferromagnetic states were not taken into account at this level of theory.

Similarly to the case of linear configurations, in the kite structures, the terminal oxygen atoms connect to the iron atom by the shortest bond compared to other oxygen–iron bonds. For cobalt oxide isomers, bond lengths are more uniform compared to the corresponding iron oxide isomers; that is, the bonds between the terminal oxygen atoms and iron atoms, as well as the remaining bonds, have very similar lengths. In contrast to iron oxide isomers, cobalt oxides maintain similar bond lengths after reduction or oxidation; bonds are not significantly shortened in cations, nor significantly lengthened in anions.

The calculated natural frequencies for all optimized isomers of iron and cobalt oxides confirm that these states are indeed local minima. Antiferromagnetic states

were obtained following the full gradient minimization procedure, and the stability of the wave function was verified.

Both computational methods, MP2 and DFT, with an extensive basis set incorporating a large number of polarization and diffuse functions, yield clearly stable isomers, also after reduction and oxidation. For each isomer of both cobalt(III) and iron(III) oxide, there are stoichiometrically two metal atoms. Single-electron reduction or oxidation does not cause disintegration of the molecule, and the calculated electron affinities and ionization potentials indicate a high stability of these systems toward redox processes, comparable to iron(III) and cobalt(III) salts and complexes (and other systems) used as redox couples in electrochemical cells (see Tables 1 and 2).

Oxygen is substantially more electronegative than iron and cobalt, as described in the Methods section. As a result, the electron density is strongly shifted toward the oxygen atoms, which is reflected in the positive effective partial charges on the metal atoms and negative charges on the oxygen atoms; see Figures 6 and 7. In the linear and spindle structures, the charges on the two metal atoms are nearly identical, whereas in kite-like molecules, the charge on the metal atom bonded to three oxygen atoms is significantly lower than on the metal atom bonded to two oxygen atoms.

Table 1. MP2/aug−cc−pVTZ and B3LYP/aug−cc−pVTZ values of vertical Ionization Potential (vIP), adiabatic Ionization Potential (aIP), vertical Electron Affinity (vEA), and adiabatic Electron Affinity (aEA) for Fe_2O_3 and Co_2O_3. The values are given in eV. The left-side superscript m in ^{m}calc represents the values calculated at the spin state m. The right-side superscripts refer to the literature data.

	vIP		**aIP**		**vEA**	**aEA**				
	MP2	**B3LYP**	**MP2**	**B3LYP**		**MP2**	**B3LYP**	**MP2**	**B3LYP**	
Fe_2O_3					Expt. ^{m}calc.					Expt. ^{m}calc.
linear	11.18	9.74	10.26	9.46		2.37	2.69	2.56	2.76	^{1} 2.39, ^{3} 2.86 [137]
kite	10.25	9.31	9.30	9.03	^{1} 8.5 [136]	2.92	2.12	3.24	2.77	^{1} 2.6, ^{3} 3.06 [138]
spindle	9.32	8.52	9.16	8.21		2.18	1.21	2.49	2.36	
Co_2O_3										
linear	12.42	10.19	11.11	9.89		2.44	2.76	2.53	2.79	
kite	11.17	10.37	9.86	9.37	^{6} 9.05 [139]	1.03	2.23	1.69	2.94	^{6} 2.75 [139]
spindle	9.92	9.12	9.25	8.69		2.54	1.35	2.71	2.47	

Table 2. UMP2/aug−cc−pVTZ and UB3LYP/aug−cc−pVTZ values of absolute standard reduction potentials (E°) and standard reduction potentials calculated against the SHE (E°_{SHE}) for the lowest-energy states of Fe_2O_3 and Co_2O_3. The temperature was 298.15 K and the pressure was 1013 hPa (1 atm). Relative water permittivity $\epsilon_r = 80$. The notation $(+1/0)$ corresponds to the reduction of the cation to the neutral molecule, and $(0/-1)$ corresponds to the reduction of a neutral molecule to an anion. The values are given in V.

	$E^{\circ\,(+1/0)}$		$E^{\circ\,(+1/0)}_{SHE}$		$E^{\circ\,(0/-1)}$		$E^{\circ\,(0/-1)}_{SHE}$	
	MP2	**B3LYP**	**MP2**	**B3LYP**	**MP2**	**B3LYP**	**MP2**	**B3LYP**
Fe_2O_3								
linear (ant.)	5.90	5.77	1.46	1.33	3.50	3.61	−0.94	−0.83
kite	5.42	4.54	0.98	0.10	3.66	4.07	−0.78	−0.37
spindle (ant.)	5.42	4.77	0.98	0.33	3.69	3.72	−0.75	−0.72
Co_2O_3								
linear (ant.)	7.26	6.57	2.82	2.13	4.43	3.81	−0.01	−0.63
kite	6.14	6.14	1.70	1.70	2.28	4.26	−2.16	−0.18
spindle	5.12	5.12	0.68	0.68	5.19	4.12	0.75	−0.32

After single-electron oxidation (in the case of cations), the charges on the metal atoms increase slightly, while after reduction (in the case of anions), the partial charges of the metal atoms decrease slightly. This indicates that, following both reduction and oxidation, it is primarily the oxygen atoms that bear the molecule's new charge, as the metal atoms more readily transfer these additional charges to the oxygen atoms. Hirshfeld charges are considerably lower than Mulliken charges owing to the more realistic charge partitioning based on electron density rather than atomic orbital overlap.

In the next step, I calculated the redox properties of the studied iron and cobalt oxides using both DFT and MP2 methods (see Tables 1 and 2). I calculated their ionization potentials and electron affinities, both vertical and adiabatic. Finally, I calculated standard reduction potentials for the case of a water solvent. As noted above, the iron and cobalt oxides were treated as molecules rather than bulk materials. Only the lowest-energy states of the neutral metal oxides, identified in the first step (see Figures 9 and 10), were taken into account.

The ionization potential corresponds to the oxidation reaction, while the electron affinity corresponds to reduction; both were calculated in vacuum, i.e., without any solvent. As shown by the DFT computations (see Table 1), the vertical electron affinity (vEA) of iron(III) oxides ranges from 1.21 eV for the most compact spindle isomer to 2.69 eV for the straight linear molecule, while the adiabatic EAs are generally close

to each other for each isomer, varying from 2.36 eV to 2.77 eV, respectively. The more compact the molecule, the smaller its electron affinity. For the MP2 computations, the vEAs range from 2.18 eV for the spindle isomer to 2.92 eV for the kite-like configuration. Similarly, the electron affinity of a neutral spindle Fe_2O_3 structure was reported by Hongbin Wu et al. [138] in a photoelectron spectroscopic study of monoiron oxides (FeO_y^-) and diiron oxides ($Fe_2O_y^-$), where (y = 1–4) and (y = 1–5), respectively. The adiabatic electron affinity (aEA) was determined from the binding energy of the vibrational feature at $v = 0$, when vibrational structures were resolved for the ground state, and the reported value for the spindle at the ground state was 3.06 eV. Simultaneously, Reilly et al. reported calculated vertical EA values of 2.39 eV and 2.86 eV for the singlet and triplet spin states, respectively [137], using the DZVP basis set with the generalized gradient approximation (GGA) method. Importantly, their results indicate that the ground state of $Fe_2O_3^-$ is a doublet kite-like configuration, even though no other isomers were considered. In the case of Co_2O_3, the structural reactivity of cobalt oxide clusters with CO was studied by Johnson et al. [139] using DFT with the GGA functional and DZVP basis sets. The calculated electron affinity and ionization potential for neutral Co_2O_3 were 1.76 eV and 7.9 eV at the antiferromagnetic configuration, respectively, while at the quintet spin state, these values were 2.75 eV and 9.05 eV. Another DFT study on the Fe_2O_n series was carried out by Gutsev et al. [136], who applied the BPW91 exchange-correlation functional and the 6-311+G* basis set. At that level of theory, the lowest-energy state was identified as an antiferromagnetic singlet for $2 < n < 5$, and the calculated adiabatic electron affinity and adiabatic ionization potential for kite Fe_2O_3 were approximately 2.5 eV and 8.5 eV, respectively. Electron affinities for bulk crystal heterostructures of ϵ-Fe_2O_3 and α-Fe_2O_3 were calculated using the PBE0/pseudopotential approach with plane waves, yielding values of 4.74 eV and 3.31 eV, respectively [135]. The first adiabatic ionization potentials, as shown in Table 1, range from approximately 8 eV to 9 eV for iron oxides and from approximately 9 eV to nearly 10 eV for cobalt oxides, as determined by the B3LYP computations. At the MP2 level of theory, the IPs and EAs are somewhat higher, with the largest values for the linear isomer and the smallest for the spindle configuration. For cobalt trioxides, both IPs and EAs are generally higher by 1–2 eV. The ionization potential is related to the one-electron oxidation process and is consequently about three times larger than the computed electron affinities at the same level of theory, while the electron affinity reflects the molecule's ability to accept an electron. Thus, both iron(III) and cobalt(III) oxides are approximately three times more likely to undergo reduction than oxidation.

Although the iron oxides studied here are the smallest possible representatives of iron and cobalt oxide materials, such as nanoparticles, it has been demonstrated that they can undergo one-electron reduction. Moreover, the experimental standard reduction potential of the half-reaction $Fe^{3+}_{aq} + e^- \rightarrow Fe^{2+}_{aq}$ is +0.77 V relative to the SHE; however, under standard basic conditions, the redox potential is -0.54 V (relative to SHE). For the reaction $Co^{3+}_{aq} + e^- \rightarrow Co^{2+}_{aq}$, the standard potential is +1.82 V relative to the SHE, while under standard basic conditions, the redox potential is +0.17 V. It is thus clear that aqueous cobalt(III) salts are considerably stronger oxidizing agents than the corresponding iron(III) salts. Iron trioxides exhibit standard reduction potentials ranging from -0.37 V to -0.72 V (relative to the SHE), depending on the geometry of the oxide, as determined at the DFT level of theory (see Table 2). The largest value was calculated for the kite-like structure and the smallest for the linear isomer. From the MP2 computations, the $E^{\circ\,(0/-1)}_{SHE}$ values are similar, ranging from -0.94 V for the linear isomer to -0.75 V for the spindle-like isomer. At the MP2 level, the largest value was obtained for the spindle-like structure and the smallest for the linear isomer. For cobalt trioxides, the standard reduction potentials span from -0.63 V to -0.18 V according to DFT calculations, while the MP2 computations yield a broader range from -2.16 V to $+0.75$ V. Thus, despite being the smallest possible units, the $(Me_2O_3)_1$ molecules demonstrate redox behavior that favors reduction. Cobalt oxide is more susceptible to reduction than iron oxide, and the same conclusion holds for the corresponding aqueous salts of cobalt(III) and iron(III). Kite Fe_2O_3 and linear Co_2O_3 are the most easily reduced by one electron, in contrast to the other respective configurations, as revealed by the DFT investigations. By analogy, the kite configuration of iron oxide and the linear molecule of cobalt oxide are the least susceptible to oxidation compared to the other configurations, as they have the largest ionization potentials. Interestingly, the linear configuration of iron(III) oxide was not even mentioned by authors investigating possible configurations of iron trioxides at various sizes [31; 32; 33; 34; 132]. Investigations of larger systems partially support these findings. The standard potential of the iodide/triiodide redox couple is 0.35 V (versus the SHE) [140], and this redox couple is widely used, for instance, in dye-sensitized solar cells. Fe_2O_3 small hematite crystals possess photocatalytic activity for the oxidation of sulfite (S(IV)), as shown by Faust et al. [141]. Kormann et al. [142] examined the applicability of Fe_2O_3 (3–20 nm in size) as a photocatalyst and compared the photocatalytic activity of hematite to that of ZnO and TiO_2 colloids and suspensions [143]. Furthermore, Yan et al. demonstrated that the pseudocapacitive behavior of Fe_2O_3 can occur in 1-ethyl-3-methylimidazolium

tetrafluoroborate ($EMIMBF_4$) ionic liquid, and that it is closely related to the chemical state variation between Fe^{3+} and Fe^{2+} on the surface of an Fe_2O_3 electrode during charging and discharging processes [25]. Interestingly, the presence of an antiferromagnetic configuration versus a high-spin ferromagnetic configuration does not significantly affect the calculated redox potentials for a given isomer; the calculated values are quite similar in both cases.

6.1.2 $(Fe_2O_3)_2$

B3LYP/aug-cc-pVTZ-optimized structures of the dimers of iron trioxides and their spins were depicted in figure 16. Here the achieved structures are evidently more compact than the smallest linear or bent iron trioxides. All the structures resemble multi-ring, cage or semi-cage structures, in some cases being quite similar to bricks of crystals (D1, D5), despite the fact that none symmetry was intentionally imposed. The structure D5 resembles organic adamantane because it posses three 6-atom rings, in this case consisting of iron and oxygen atoms.

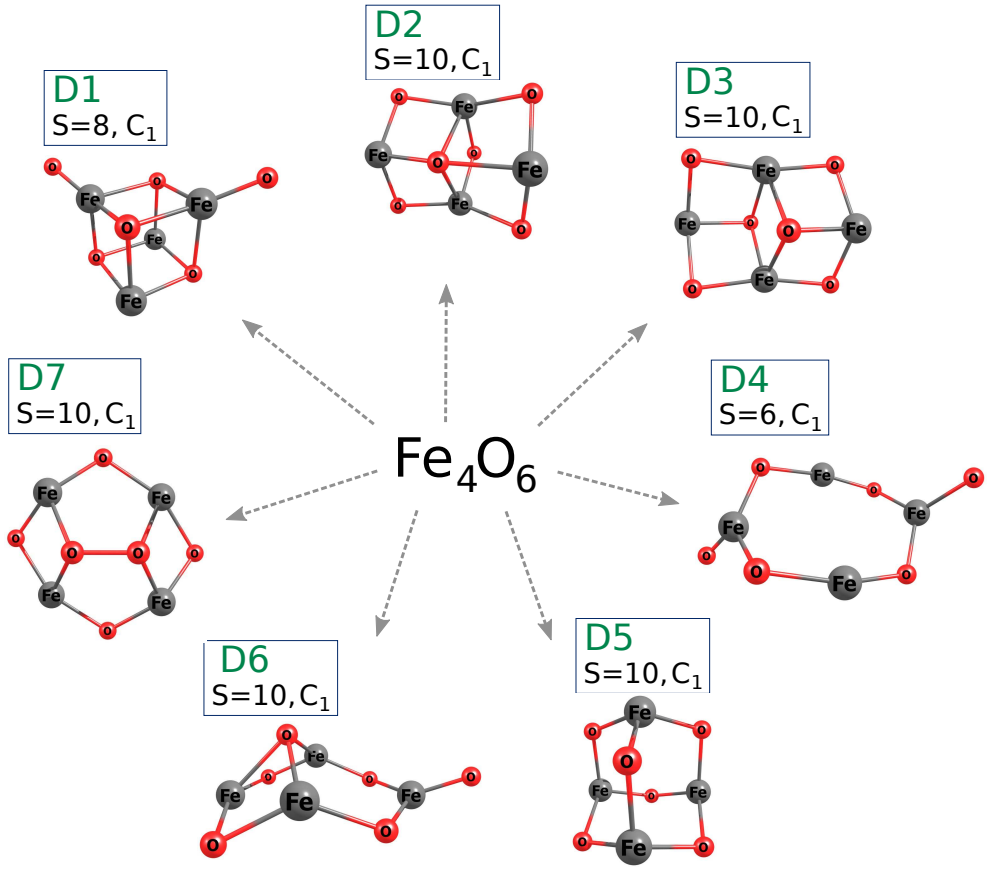


Figure 16. Lowest-energy structures. n=2. B3lyp/aug-cc-pVTZ

Comparison of energies of all isomers of the $(Fe_2O_3)_2$ molecules found were shown in figure 17. As it reveals for each basis set employed, both all-electron and pseudpotential, the lowest-energy structure is the D3, however the D5, i.e. the adamantane-like structure has almost equal energy. Typically, all dimers prefer larger spin, even some states were not able to achieve for smaller spins; singlets were found for all types of structures, while doublets, triplets and for some basis sets even quartets, quintets and sextets were not achievable. Similar to the case of n=1, the differences between energies of the lowest-energy states and energies of the corresponding singlets are very large, ranging from about 120 kcal/mol up to even 200 kcal/mol (depending on the basis set used and the type of the structure) which is relatively large amount of energy.

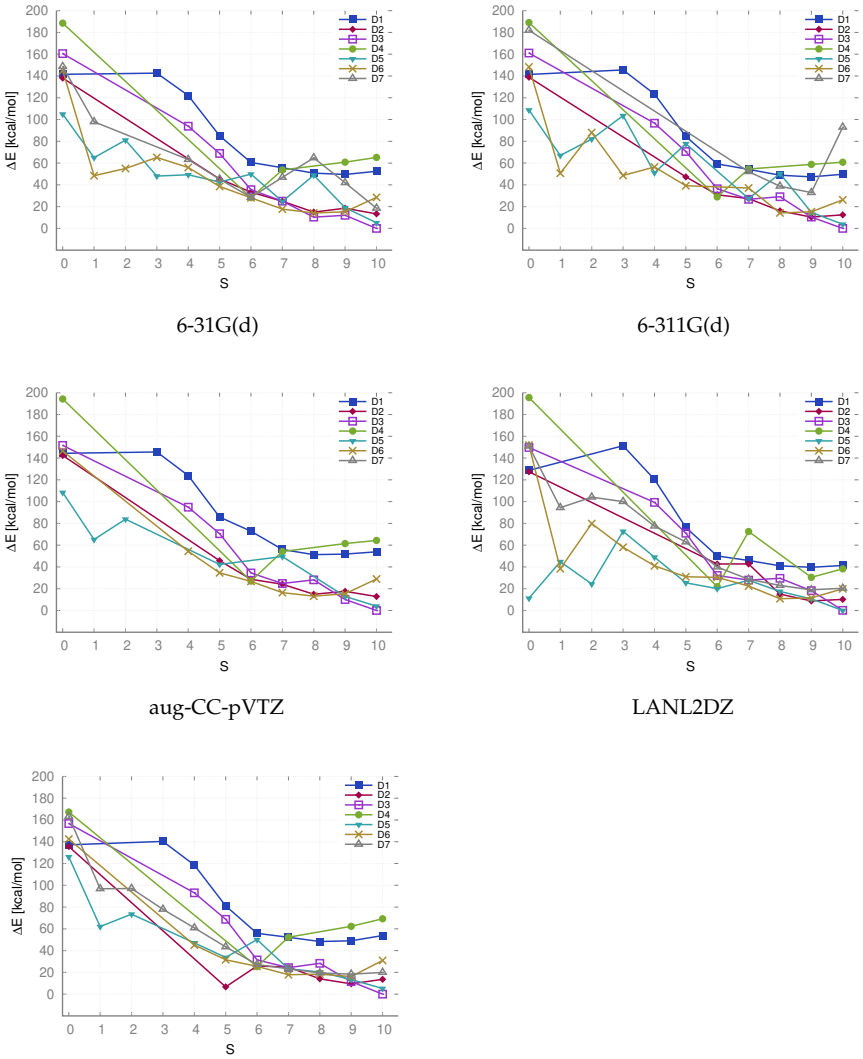


Figure 17. DFT B3LYP relative energies [kcal/mol] (calculated against the energies of D3 structure (S=10)) revealed for all 6 identified structures of the $(Fe_2O_3)_2$ Each subfigure was captioned by the basis set used during the computations.

6.1.3 $(Fe_2O_3)_{3,4}$

Isomers of trimer and tetamer $(Fe_2O_3)_n$ where (n=3,4) are optimized using B3lyp/lanl2dz and the ground state structures are depicted in Figure 18. The choice of the basis set is based on my analysis of the $(Fe_2O_3)_n$ n=1,2, where I have determined that pseudopotential (lanl2dz) gives qualitatively good result on the spin-state energetics. To begin with (n=3), the isomers (T1, T2, T3) of $(Fe_2O_3)_3$ are found the most stable spin-state (S=15). It is worth noting that (T4) is the only isomer of $(Fe_2O_3)_3$ studied in

my research which contains oxygen in the terminal position, and its ground state is associated with spin (S=14). Among four isomers of $(Fe_2O_3)_3$, (S=15) T1 is found the most stable isomer of $(Fe_2O_3)_3$, and it looks like two kite-like structures attached to six atom site hexagonal view. The similar structure was also observed for $(Al_2O_3)_3^+$ molecule[144]. Unlike T1 the optimized T2 structure appears to be more diffused and resembles trimer adamantane-like structure and it is the only structure Xun-Lei Ding et al.[33] did not achieved. The optimized T3 structure does not differ much from the T1 structure and it appears to be the second most stable structure of $(Fe_2O_3)_3$. Contrarily optimized the most stable structures of $(Fe_2O_3)_4$ do not contain any oxygen at the terminal position in its complexes and they are much compact compared to $(Fe_2O_3)_3$. B3lyp/lanl2dz optimized structures are depicted in Figure 6.1.3. From a structural point of view, isomers of tetramer iron trioxides have irregular shapes with their ground state (S=20) for Q1-Q3. On the other hand, (S=19) ground state structure of Q4 looks more ordered and it has tetragonal prisma core. Also, it resembles two (D3) the most stable structure of $(Fe_2O_3)_2$ are attached side-by-side to each other forming a compact $(Fe_2O_3)_4$ structure. Moreover, this type of structure was not reported in[31; 33]

From the spin-state energetics point of view, I calculated relative energy as a function of spin with respect to the lowest energy state of each particular $(Fe_2O_3)_3$ and $(Fe_2O_3)_4$. From the depicted Figure 6.1.3 and 6.1.3 the energy difference among the most stable isomers are not large as compared to the smaller size of iron trioxides at ground state. However, I noticed energy difference between low-spin (S=0) state and high-spin (S=15) for n=3 and (S=20) for n=4 are larger than those calculated low-spin, high-spin energy difference for smaller size of iron trioxides. Note low-spin (S=0) is closed-shell singlet in my all calculations.

It is also visible that the ground state the (T3) isomer of $(Fe_2O_3)_3$ appears to be slightly higher (0.32 kcal/mol) in energy than the most stable isomer (T1) being the second most stable isomer. However, intermediate spin-state (S=8) of (T1) isomer appears to be stable than those T2 and T4 isomers. Therefore, it is important to check all the possible spin states. Moreover, it is visible from my result in Figure 6.1.3 that at low-spin states and very intermediate spin-states the energy difference are larger than at very high intermediate spin-states. Similarly, for $(Fe_2O_3)_4$ which has found the Q2 structure is the most stable isomer as shown in Figure 6.1.3. It is worth noticing that ground state (Q1) and (Q2) isomers have almost negligible energy difference. However, at low-spin state and intermediate spin-states the (Q1) appears to have higher in energy than (Q2). Also, as I mentioned on the analysis of $(Fe_2O_3)_3$ that energy difference between two states

decreases at very high intermediate spin-states.

Additionally, it is important to mention that larger structures of iron trioxides are studied only by employing the lanl2dz basis set at the B3lyp level. From the structural and spin versus energy perspective the lanl2dz provides good agreement with the results obtained from $(Fe_2O_3)_{1,2}$.

Overall, studied structures of iron $(Fe_2O_3)_{3,4}$ have a ground state where energies tend to be degenerate. Furthermore, high spin structures of $(Fe_2O_3)_{3,4}$ appear to be C_1 symmetric.

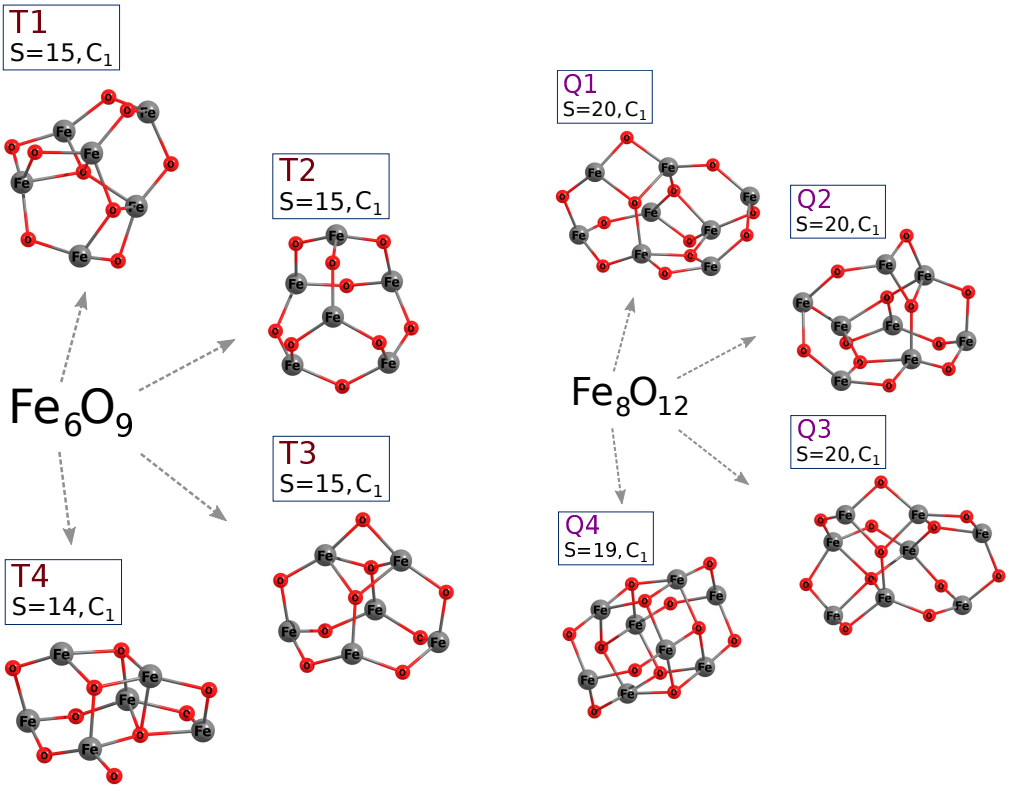


Figure 18. Lowest-energy structures of $(Fe_2O_3)_{3,4}$. B3lyp/lanl2dz

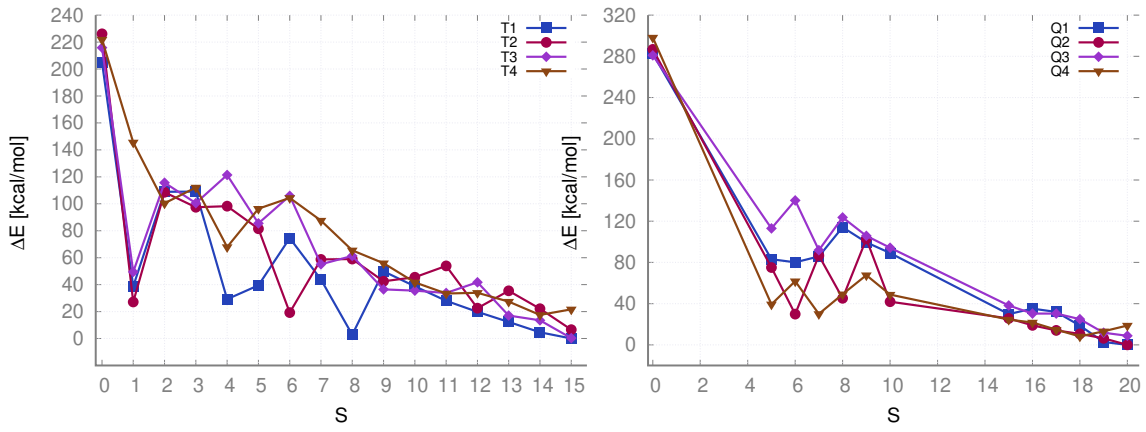


Figure 19. B3LYP/LANL2DZ relative energies [kcal/mol] (calculated against the energies of T1 structure (S=15) for n=3 and Q2 structure (S=20) revealed for 4 identified structures of the $(Fe_2O_3)_n$ where n=3,4 respectively

6.1.4 Charges

Magnetic iron trioxide nanoparticles were recently employed to obtain stable, long-lasting colloidal suspensions in several ionic liquid systems, forming true ferrofluids [29]. The stabilization of these suspensions was achieved through the use of specific surfactant ions in combination with ionic liquids, both of which contribute to the liquid interface. As revealed in this study, the surface charge of the nanoparticles played a critical role in governing the layering behavior of the surrounding ionic liquid.

One particularly effective surfactant ion was citrate an anion containing three carboxylate groups. Based on this, the authors [29] inferred that the surface of the iron trioxide nanoparticles must have been positively charged. However, they did not elaborate on the exact nature of the interaction between citrate ions and the Fe_2O_3 surface.

In a separate study, iron trioxide nanoparticles were also incorporated into graphene-based electrodes, where the electrochemical performance of the resulting pseudocapacitive system immersed in an ionic liquid was clearly attributed to redox reactions involving surface Fe^{3+} ions [25].

As demonstrated earlier, iron trioxide systems can adopt a wide range of structural and spin configurations. For larger molecules, the number of feasible structural isomers is expected to increase even further. Compounding this complexity is the fact that

certain configurations are only accessible at specific levels of theory or with certain computational tools. This makes any analysis of structure-dependent properties or physical quantities particularly delicate and method-dependent.

Given these considerations, I undertook a more detailed investigation of the partial atomic charges of iron atoms in Fe_2O_3 molecules, beginning with the smallest systems. Specifically, I computed two key quantities: (1) the average Mulliken partial charge of all iron atoms within a given structure (for $n = 1, \ldots, 4$), and (2) the individual Mulliken charges on each iron atom across all structures. The latter was especially important for analyzing charge separation between surface and interior iron atoms in larger iron trioxide molecules. The average partial charges as functions of total spin multiplicity are presented in Figures 20 and 21.

Table 3. Average partial atomic charges Fe ions in lowest energy state of $(Fe_2O_3)_1$

	6-31+G(d)	6-311+G(d)	aug-cc-pVTZ	LANL2DZ	Sapporo-DZP
Kite (S=4)	0.87	0.63	1.04	0.86	0.83
Spindle (S=4)	0.62	0.61	1.1	0.78	0.83
Linear (S=3)	0.93	0.92	0.92	0.78	0.77
Bent (S=5)	1.05	0.56	0.98	0.87	0.84

As it is seen in charts in fig. 20, essentially for each basis set used the average partial Mulliken charges on iron atoms increase along with the increase of total spin of the system, despite the fact that for some states there were aberrations. The partial charges for the highest spins range from 0.6e to 1.1e. The largest charges were found for different types of structures depending on the basis set used and there is no any regularity. Pseudpotential basis sets give lower average charges and the largest charges were found by using the basis sets augmented by diffuse functions, i.e. the aug-cc-pVTZ. It's unfortunately another case in which the properties of iron trioxides depend on the basis set used. In table 3 I additionally show the average Mulliken charges for the lowest-energy structures for n=1, comparing the basis sets used, similarly as I did for the structures, see section 6.1.1. Also in this case.

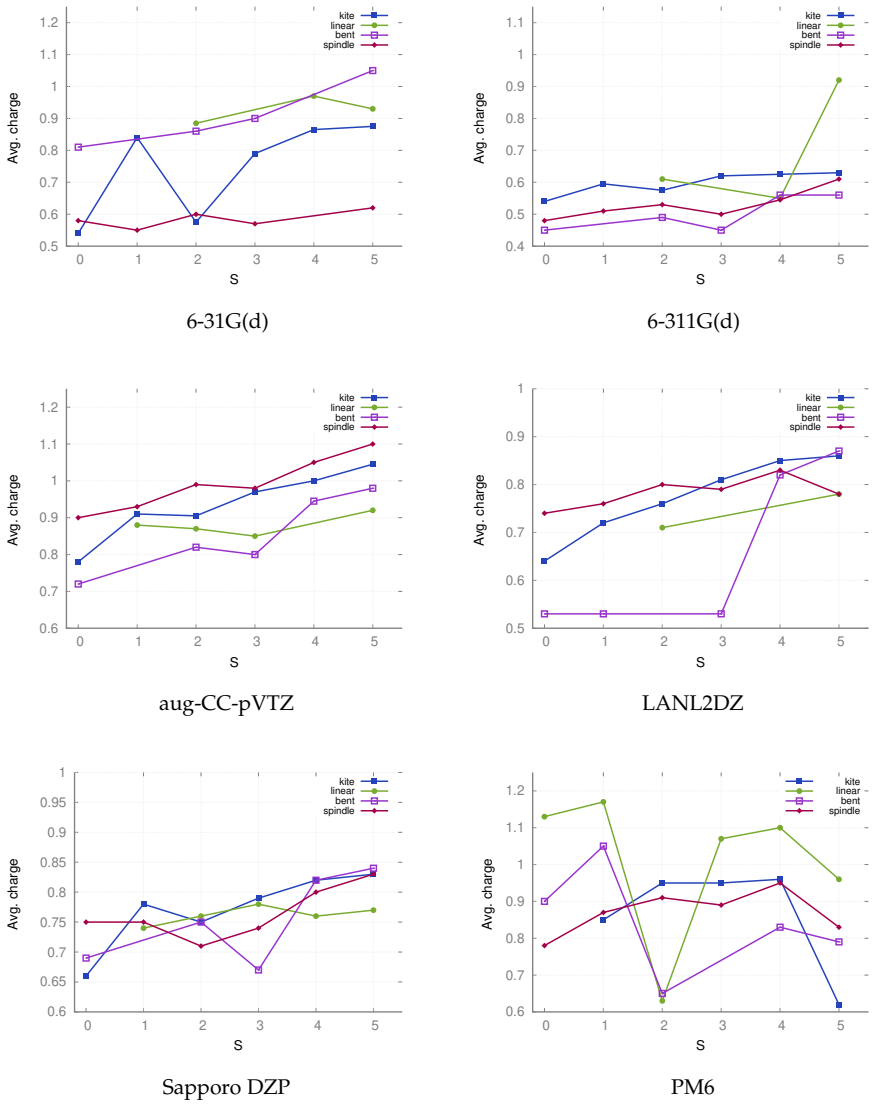
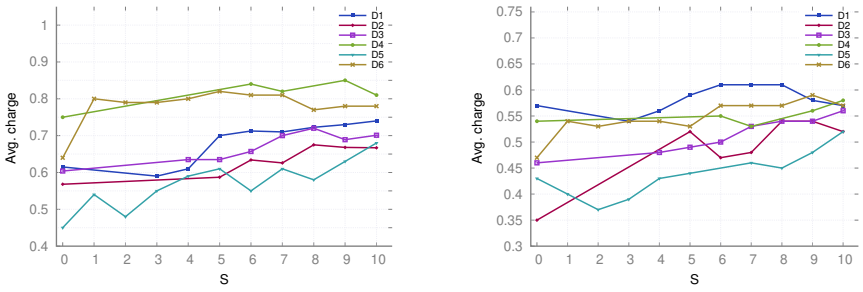
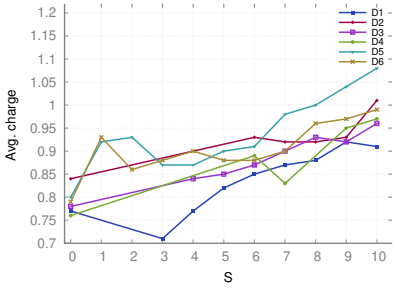


Figure 20. Mulliken partial charges for n=1.

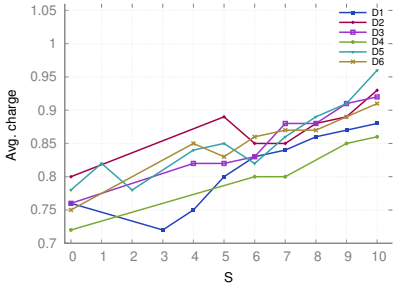


n=2, 6-31G(d)

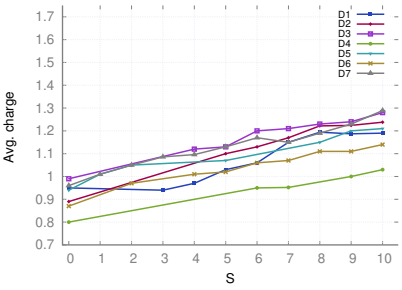
n=2, 6-311G(d)



n=2, LANL2DZ

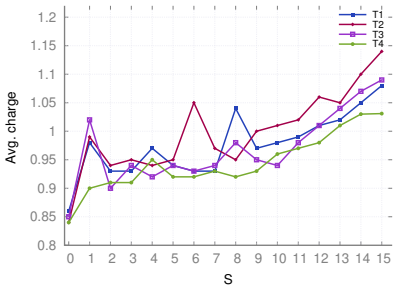


n=2, Sapporo DZP

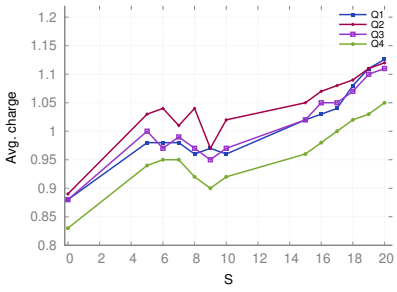


n=2, aug-cc-pVTZ

Figure 21. Mulliken partial charges for n=2.



n=3, LANL2DZ



n=4, LANL2DZ

Figure 22. Mulliken partial charges for n=3 and n=4.

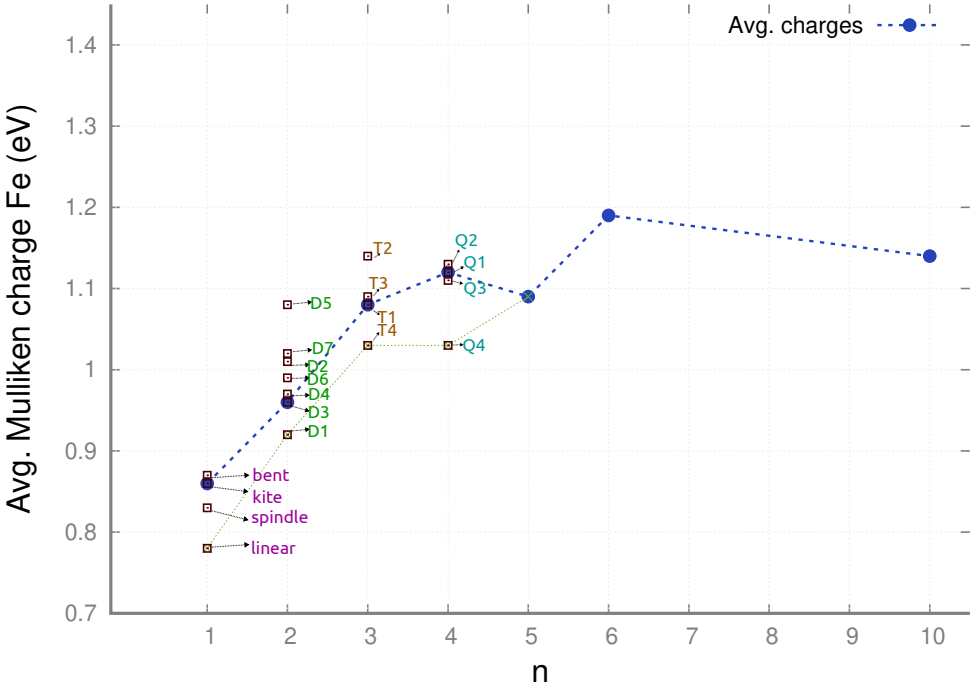


Figure 23. Average Mulliken partial charges found for the lowest-energy structures of $(Fe_2O_3)_n$ (points connected with dashed lines) for respective n.

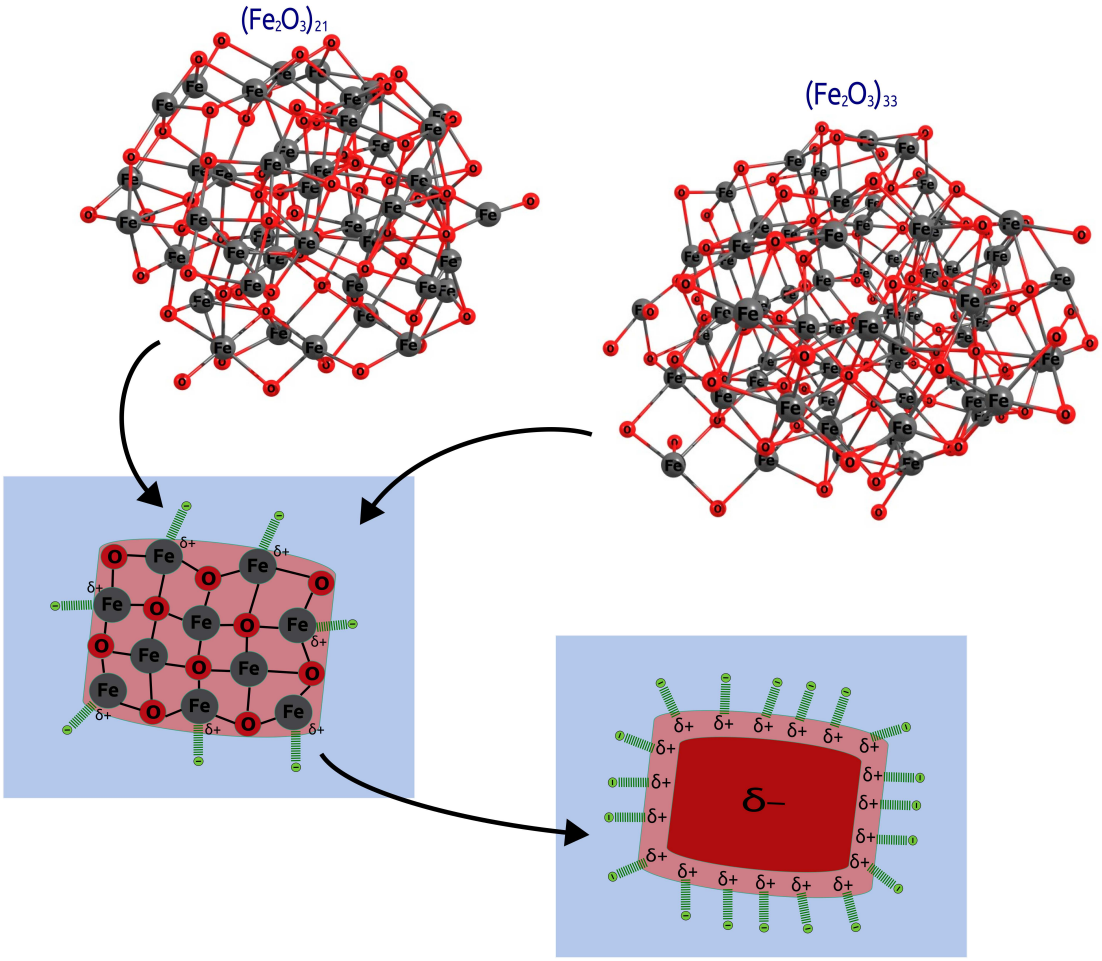


Figure 24. Depiction of larger-size iron trioxide particle. Surface positive partial charges of iron atoms were ilustrated along with the interaction of the surface with negative ions of liquids.

6.1.5 HOMO-LUMO gap

The HOMO-LUMO energy gap plays an important role in the stability and reactivity of the molecules which means a higher HOMO-LUMO gap indicates a more stable molecule. However, from a reactivity perspective, the smaller the HOMO-LUMO energy gap indicates high reactivity since there is a smaller energy gap for electron to move from the highest occupied molecular orbital (HOMO) to the lowest unoccupied molecular orbital (LUMO). The calculated HOMO-LUMO gap for the most stable spin state of $(Fe_2O_3)_n$ (n=1-4) molecules are shown in 25. Important to note that since the ground states of iron trioxide molecules are associated with high spin, there are many singly occupied orbitals depending on the size of the iron trioxide molecules therefore, I refer

to SOMO (Singly Occupied Molecular Orbitals) as HOMO. Also, in spin unrestricted formulation of Kohn-Sham DFT, there are two sets of spin densities one for alpha spin (spin up) and another for beta spin (spin down). In this case, I have taken into account both sets of orbitals and energy levels associated with these orbitals and DFT calculations have been module tool for predicting HOMO-LUMO gap of metal and metal oxide molecules[145; 146; 147; 148; 149; 150] due to reasonable estimation of excitation energy[151]

Since we are limited by the size of the molecule for all electron basis sets including polarization and diffuse functions (aug-cc-pVTZ) at first I represent the HOMO-LUMO energy gap for $(Fe_2O_3)_n$ (n=1-2) in two different basis sets one from Pseudopotential basis set LANL2DZ and another all electron basis set aug-cc-pVTZ as it is shown in Figure.**??**,17. From the result depicted in 25, the HOMO-LUMO energy gap for the smallest iron trioxide Fe_2O_3 deviates from 1.69 eV to 3.21 eV and from 3.30 eV to 1.54 eV in the basis of LANL2DZ and aug-cc-pVTZ respectively. From the structural perspective, the kite was found to have a nonet ground state in LANL2DZ and aug-cc-pVTZ basis sets, and it is found that the HOMO-LUMO energy gap only deviates 0.02 eV (3.21, 3.21). This means Pseudopotential basis set LANL2DZ with B3LYP functional predicts reasonable HOMO-LUMO gap. However, the largest HOMO-LUMO deviation was found with the bent structure (2.92,3.30 eV) and this could be the reason different bent type structures and spin states were observed in LANL2DZ and aug-cc-pVTZ basis sets. Among four types of Fe_2O_3 structures, linear is found to have the smallest HOMO-LUMO gap (1.69, 1.54 eV) in both LANL2DZ and aug-cc-pVTZ basis sets. These findings indicate that the stoichiometric composition of molecules play also important role in calculated HOMO-LUMO gap. Within the LANL2DZ basis set the highest HOMO-LUMO energy gap is found with the most stable kite structure which arises from the fact that the high HOMO-LUMO energy gap the more stable molecules.

Similarly, in the case of $(Fe_2O_3)_2$ the calculated HOMO-LUMO energy gap for 7 types (D1-7) of $(Fe_2O_3)_2$ structures are shown in Figure. 25. In this case, from the structural stability perspective the predicted HOMO-LUMO energy gap for $(Fe_2O_3)_2$ exhibits no systematic pattern as it was found that the D3 is the most stable structure of $(Fe_2O_3)_2$ among (D1-7). However, the highest HOMO-LUMO energy gap (3.23 eV) is calculated for the D5 type structure of $(Fe_2O_3)_2$ in the basis of LANL2DZ. It is also important to mention that in the basis of LANL2DZ the ground state structures of D3 and D5 degenerate as shown in Figure.17. Also, low spin ground state isomers D4 and D6 have the same 3.21 eV HOMO-LUMO energy gap and this energy gap is higher

than in comparison to energy gap calculated for (D1-3,7) in the basis set LANL2DZ. Between two basis sets LANL2DZ and aug-cc-pVTZ calculated HOMO-LUMO energy gaps represent divergent energy gaps for all the (D1-7) structures of $(Fe_2O_3)_2$ and the highest divergent energy was found in D6. It could be due to presence of a single terminal oxygen in the structure of D6 that LANL2DZ estimates HOMO-LUMO energy gap higher than in the case of aug-cc-pVTZ which includes polarization and diffuse functions on all atoms. Summing up overall calculated HOMO-LUMO energy gap for $(Fe_2O_3)_2$ are in the range of 2.28-3.23 eV and 2.27-3.05 eV for LANL2DZ and aug-cc-pVTZ basis sets respectively.

In the case of $(Fe_2O_3)_n$ (n=3,4), overall HOMO-LUMO energy gap range decreases increasing size of n of $(Fe_2O_3)_n$, and HOMO-LUMO energy gap among their respective isomers (T1-4) of $(Fe_2O_3)_3$ and (Q1-4) of $(Fe_2O_3)_4$ remains nearly the same. Similar results were observed in the case of $(Y_2O_3)_n^{0,-1,+1}$ (n=1-10) molecules[152]. Also, my results are consistent with the fact that the most stable molecules of $(Fe_2O_3)_n$ (n=3,4) shows the highest and equal HOMO-LUMO energy gap 2.58 eV. Previously reported values by Uday Kurien et al.[153] for nanosize γ-Fe_2O_3 and α-Fe_2O_3 are 2.39 and 2.2 eV respectively. Moreover, David M. Sherman experimentally studied the reactivity of Fe-Mg (hydr)oxide minerals to sunlight-induced photochemical dissolution by electronic structure of the mineral-water interface and has found iron(III) (hydr)oxide minerals have band gap of nearly 2.0-2.5 eV and manganese(IV) oxides have smaller 1.0-1.8 eV band gaps.

Overall, predicted HOMO-LUMO energy gaps from smalls $(Fe_2O_3)_1$ to largest $(Fe_2O_3)_4$ considered in this study show good agreement experimentally reported energy gaps for γ-Fe_2O_3 and based on my knowledge HOMO-LUMO energy gap of various sizes $(Fe_2O_3)_n$ (n=1-4) were not reported before.

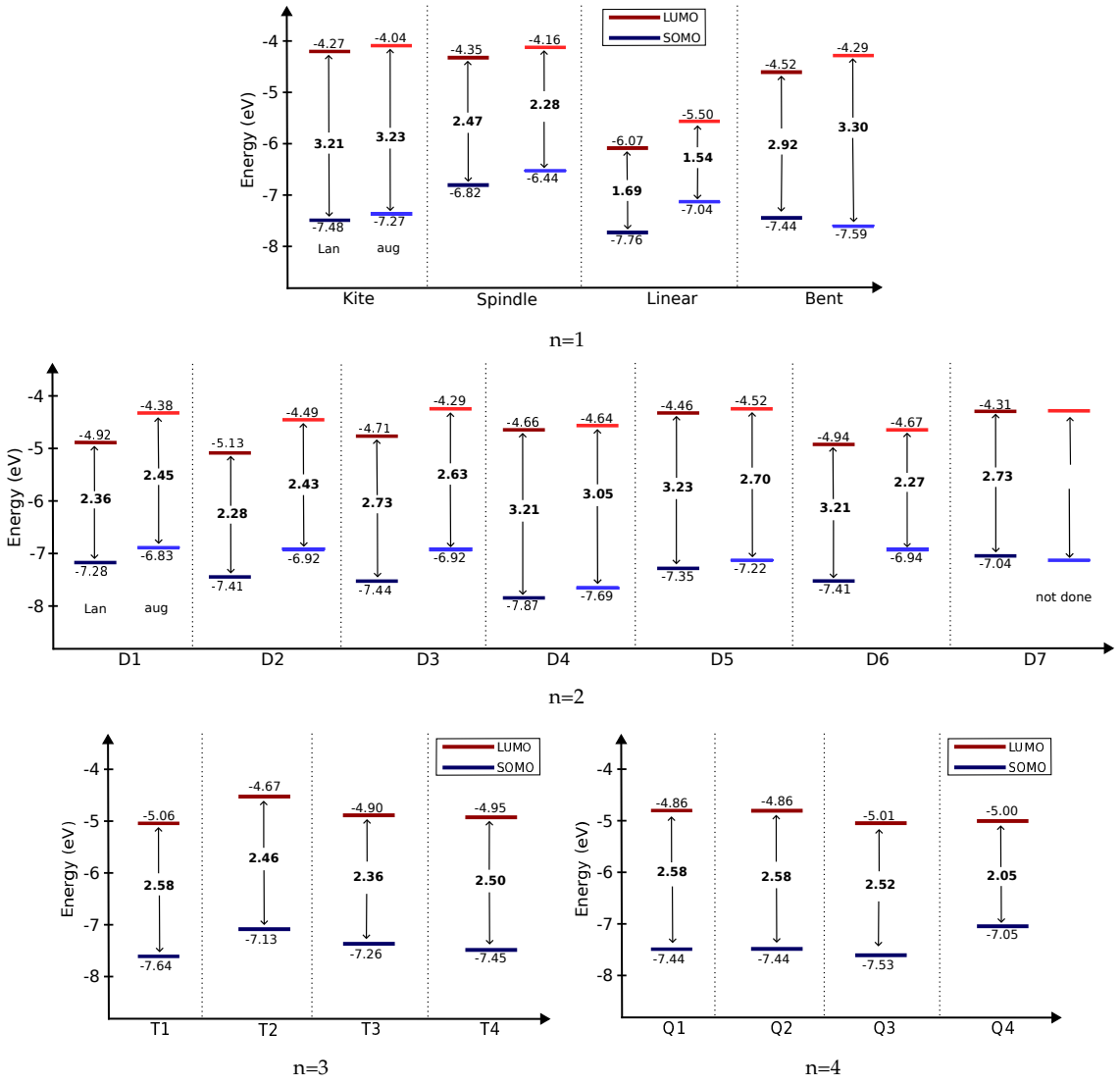


Figure 25. HOMO LUMO gap

6.2 NH_3 decomposition reaction on $(Fe_2O_3)_n$, n=1-4

In this section, I am going to discuss one of my achievement, which was published in JCP journal[154]. Ammonia decomposition process plays crucial role in geen energy technology. Here, I systematically investigated the ammonia decomposition reaction mechanisms on $(Fe_2O_3)_n$ molecules of various sizes n, where $n = 1{-}4$. Firstly, I identified approximate reaction pathways for the interactions between NH_3 molecules and the most stable isomers of $(Fe_2O_3)_n$ molecules using the Artificial Force Induced Reaction (AFIR) technique. The obtained AFIR pathways were subsequently re-optimized along the minimum energy path using the Locally Updated Plane (LUP) method, without

applying artificial forces. I calculated various reaction mechanisms and the stepwise dissociation[155] of hydrogen atoms from nitrogen-containing compounds on Fe(III) oxide molecules, following the elementary steps:

$$NH_3 + ^* \rightarrow NH_3^* \tag{6.1}$$

$$NH_3^* \rightarrow NH_2^* + H^* \tag{6.2}$$

$$NH_2^* + H^* \rightarrow NH^* + 2H^* \tag{6.3}$$

$$NH^* + 2H^* \rightarrow N^* + 3H^*, \tag{6.4}$$

Here, * denotes a free molecule, while the adsorbed intermediates on the surface of the $(Fe_2O_3)_n$ molecules are represented by * in the superscript.

Finally, the adsorbed hydrogen atoms on the $(Fe_2O_3)_n$ molecules can combine to produce molecular hydrogen (H_2):

$$NH^* + 2H^* \rightarrow NH^* + H_2 \tag{6.5}$$

$$N^* + 3H^* \rightarrow N^* + H^* + H_2 \tag{6.6}$$

This section, is organized as follows. I first discuss the structures of free molecular structures of iron trioxide, followed by the adsorption of NH_3 on the most stable isomers of $(Fe_2O_3)_n$, $n = 1 - 4$, molecules. I then examine the complete dehydrogenation and H_2 formation processes for each molecular size.

6.2.1 Structure of $(Fe_2O_3)_n$ molecules with $n = 1 - 4$

Figure 26 demonstrates the most stable structures of small $(Fe_2O_3)_n$ molecules with $n = 1 - 4$, as obtained in the present work using automated AFIR approach. A total of up to 60 isomer structures have been obtained for each molecular size n. The low-energy isomers for each molecule size, along with their relative binding energies are presented in Figs. S2-S5. I found that the most stable structure of the smallest Fe_2O_3 molecule is a nonet kite-like type with a binding energy E_b=362.7 kcal/mol. This finding confirm my previous investigations discussed in previous section. For the best of my knowladge, the kite-like structure is a commonly studied configuration[156; 157; 158]. They observed

the most stable spin configuration for this structure to be S=0. In contrast, I found that the lowest energy structure corresponds to a nonet state with S=4, while the singlet kite-like structure is 0.62 kcal/mol less stable at the B3LYP/6-31+G* level of theory as shown in Table S1. This finding is also compared with another hybrid functional, M06,[159] and a range-separated functional with additional dispersion correction, wB97XD,[160] in Table S1. The results of my calculations show that the absolute binding energy of $(Fe_2O_3)_n$ rapidly increases with increasing $(Fe_2O_3)_n$ molecule size n from 1 to 2 by 60.4 kcal/mol. However, further growth in binding energy with molecule size slows down, demonstrating a tendency for saturation as n increases.

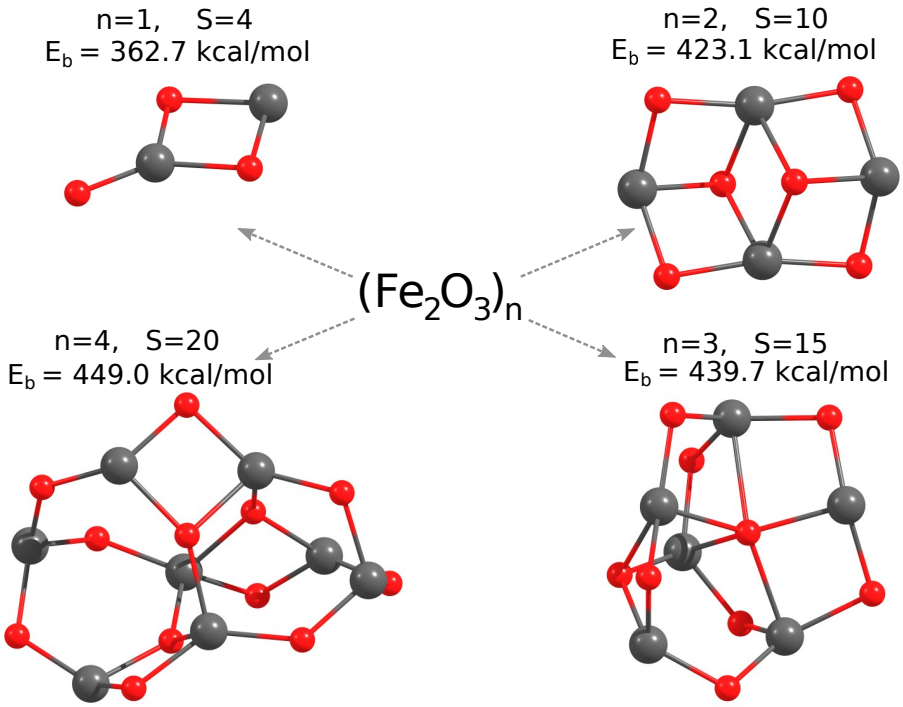


Figure 26. The most stable structures of $(Fe_2O_3)_n$ molecules with $n = 1 - 4$. The total spin S and the binding energy E_b, of the molecules are shown in inserts.

6.2.2 Ammonia adsorption on $(Fe_2O_3)_n$ molecules

Adsorption of ammonia on $(Fe_2O_3)_n$ molecules is a crucial initial step in the whole dehydrogenation process. Figure 27 demonstrates the most stable adsorption configurations of the NH_3 molecule on $(Fe_2O_3)_n$ molecules with $n = 1 - 4$. The corresponding basis set superposition error corrected free energies of adsorption and Fe−N bond distances are shown in Table 4 at 0 K. My calculations show that the adsorption of NH_3 on the smallest Fe_2O_3 molecule is the most stable among all molecular sizes considered in this study, with an adsorption free energy of -28.55 kcal/mol. This finding is corrobo-

rated by Mulliken charge analysis, which shows that more electrons are shared between the lone pair of the N atom and the 3d orbitals of Fe^{2+} for $n = 1$. On the other hand, for larger molecular sizes with $n = 2 - 4$, which primarily contain Fe^{3+}, the electron density is more localized over the bonding region, as also reported by Sierka *et al.*[158] Therefore, bonding occurs with the nitrogen lone pair.

My theoretical analysis indicates that the adsorption energy ΔG_{ads} of ammonia on $(Fe_2O_3)_n$ molecules decreases from $n = 1$ to $n = 3$, followed by a slight increase for $n = 4$. A similar trend in the change of adsorption energy with molecular size was reported by Zhou *et al.*[161] for Ru_n@CNT systems. I also compared the adsorption energy of NH_3 on different metal and metal oxides in Table 4. The obtained NH_3 adsorption energies on $(Fe_2O_3)_n$ molecules are about 8 kcal/mol higher than the data reported by Zhang *et al.* for the Ru(0001) surface.[162] Moreover, the adsorption of NH_3 and NO_x on the γ-Fe_2O_3(111) surface was studied by Huang *et al.*[163] using periodic density functional calculations. They calculated adsorption energies on octahedral and tetrahedral sites of γ-Fe_2O_3(111) to be -2.13 kcal/mol and -21.68 kcal/mol, respectively. Similarly, my calculated NH_3 adsorption energies on $(Fe_2O_3)_n$ molecules for $n = 3$ and $n = 4$ are close to the data reported by Wei Huang *et al.*,[163] as adsorption of NH_3 on the three-coordinated Fe^{3+} site resembles the tetrahedral site of γ-Fe_2O_3(111), while the adsorption on the four-coordinated Fe^{3+} site resembles the octahedral site of γ-Fe_2O_3.

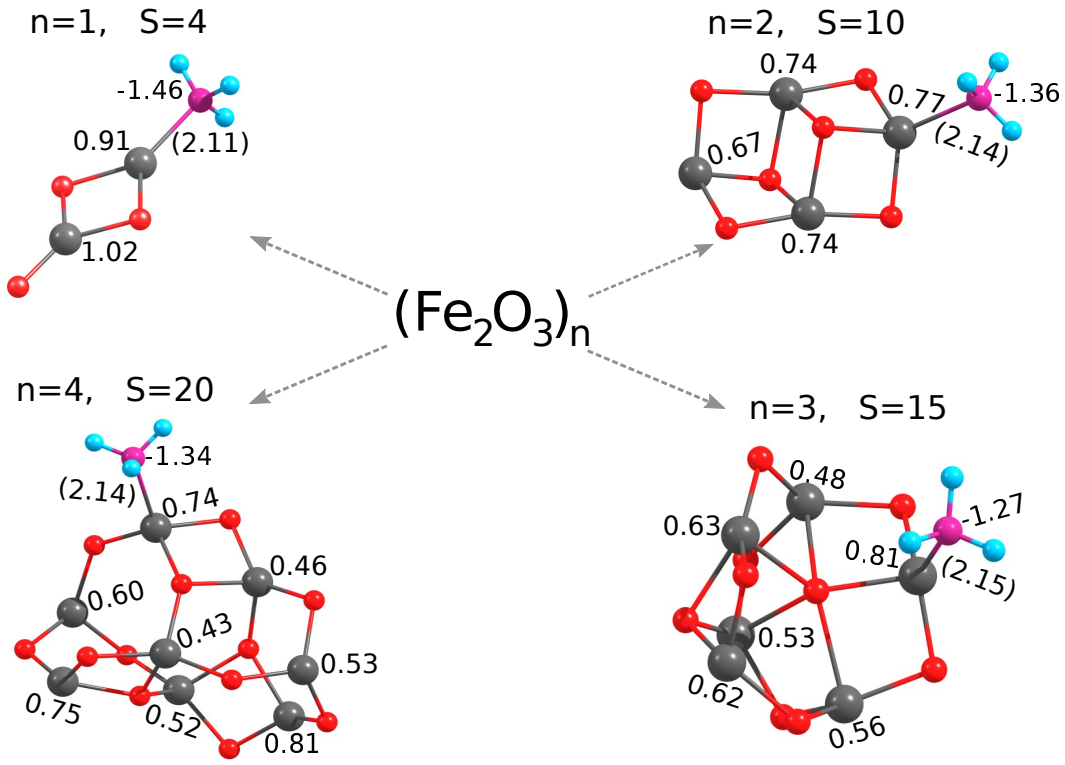


Figure 27. Optimized geometries of NH_3 adsorbed on $(Fe_2O_3)_n$ molecules for $n = 1$–4. N−Fe distances (Å) are shown in parentheses, along with the partial atomic charges on neighboring atoms. The total spin S of the molecules is shown in the insets.

Table 4. NH_3 adsorption free energy ΔG_{ads} and d(Fe – N) bond length in various size of $(Fe_2O_3)_n$ where $n = 1 - 4$.

	ΔG_{ads} *(kcal/mol)*	Fe − N (Å)	reference
NH_3/Fe_2O_3	-28.55	2.11	this work
$NH_3/(Fe_2O_3)_2$	-28.36	2.14	
$NH_3/(Fe_2O_3)_3$	-27.65	2.15	
$NH_3/(Fe_2O_3)_4$	-27.85	2.14	
$NH_3/ZnFe_2O_4(110)$	-48.54	Zn − N (2.03)	a
	-41.52	Fe − N (1.99)	
$NH_3/Ru(0001)$	-20.52	Ru − N (2.17)	b
NH_3/Fe_2O_3/AC	-49.12, -37.35	-	c
	-26.29, -31.13	-	
NH_3/γ-Fe_2O_3 nano	-37.52	-	d
NH_3/γ-Fe_2O_3 (111)	-21.68	Fe_{tet} − N (2.13)	f
	-2.13	Fe_{oct} − N (2.101)	

a,[164] b,[162] c,[165] d,[166] and f[163]

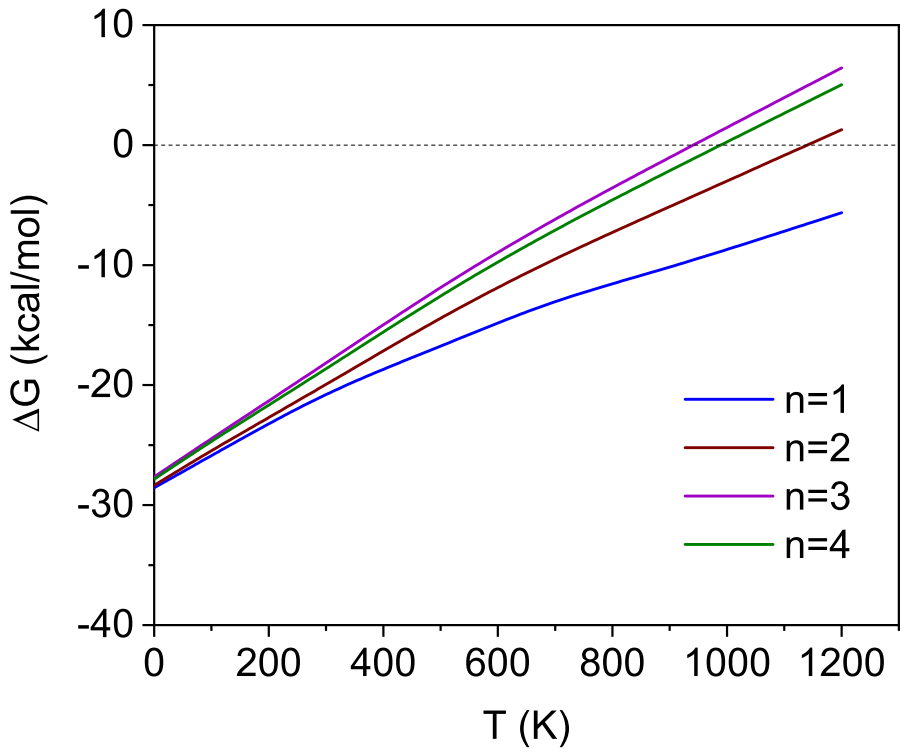


Figure 28. Temperature dependence of the adsorption free energy for NH_3 adsorption on $(Fe_2O_3)_n$ molecules with $n = 1$–4 at 1 atm.

As mentioned above, the calculated adsorption energies indicate that the adsorption of an NH_3 molecule on $(Fe_2O_3)_n$ structures ($n = 1 - 4$) weakens as the n increases from $n = 1$ to $n = 3$. In industrial processes, the dehydrogenation of ammonia typically occurs at high temperatures, often in the range of 400°C to 700°C, depending on the specific catalysts and conditions used. Therefore, it is important to determine the range of temperatures at which ammonia adsorption on $(Fe_2O_3)_n$ remains stable. Figure 28 demonstrates the temperature dependence of ΔG_{ads} in the range from 0 K to 1200 K for the most stable adsorption configurations of NH_3 on $(Fe_2O_3)n$ molecules ($n = 1 - 4$). The negative values of ΔG_{ads} correspond to stable adsorption. As seen in Fig. 28, NH_3 adsorbed on the smallest Fe_2O_3 molecule is stable across the whole range of the considered temperatures. However, for larger molecular sizes, ammonia adsorption becomes energetically unfavorable at temperatures of 1140 (K), 940 (K), and 989 (K) for $n = 2, 3$ and 4, respectively.

6.2.3 NH_3 decomposition on Fe_2O_3

In this section, I discuss the complete NH_3 decomposition and H_2 formation reactions (6.1) - (6.6) on the smallest considered Fe_2O_3, at room temperature, T=298.15

K, explored by the AFIR method. This method allows for the automatic exploration of the full reaction path network, systematically accounting for the variety of possible isomer structures and adsorption sites. This is an important approach in nanocatalysis because it has been demonstrated that the most stable structures are not always the most reactive. Therefore, a systematic search for reaction pathways that accounts for the contributions of low-energy isomers is required to accurately describe the catalytic properties of small structures at finite temperatures.[167]

To illustrate the isomer and reaction-site effects, I explicitly consider two different isomers of the Fe_2O_3: the most stable kite-like structure with one terminal oxygen atom, and the linear structure isomer with two terminal oxygen atoms which is 6.24 kcal/mol less stable (see Fig. S2). The kite-like structure possess two type of catalytically active metal centers - two-coordinated and three-coordinated Fe sites. Therefore I consider adsorption and decomposition of NH_3 molecule on both of them.

Figure 29(a) demonstrates that the adsorption of NH_3 on the kite-like Fe_2O_3 structure is an exothermic reaction, occurring at both the two-coordinated and three-coordinated Fe sites. The adsorption free energies are -21.85 kcal/mol for the two-coordinated Fe site (intermediate $I'_1 1$) and -8.75 kcal/mol for the three-coordinated Fe site (intermediate $I''_1 1$), respectively. The optimized structures of all intermediates (I) and transition satates (T) along the reaction pathways are shown in Fig. 29(b) and 30(b), for the kite-like and linear structure, respectively. Here the lower index corresponds to the molecular size n, while the numbering corresponds to the order of intermediates(transition states) along the reaction path. As discussed in the previous section, the most stable adsorption site for NH_3 is the two-coordinated Fe site, with an Fe−N bond length of 2.11 Å. In contrast, the Fe−N bond length at the three-coordinated Fe site is 2.16 Å. These findings are supported by the fact that NH_3 adsorption highly depends on the local geometry and electronic structure of the catalyst.

In the case of the Fe_2O_3 kite-like structure, the first dehydrogenation reaction is the second step in the reaction mechanism, occurring after adsorption with activation barriers of 21.85 kcal/mol and 19.58 kcal/mol through the reaction paths $I'_1$1-$T'_1$1-$I'_1$2 and $I''_1$1-$T''_1$1-$I''_1$2, respectively. The reactions on these two-coodinated and three-coordinated active sites are exothermic by 21.44 kcal/mol and 10.07 kcal/mol, respectively. However, the first dehydrogenation of NH_3 on the linear-type structure Fig. 30(a) occurs with smaller activation barrier of 13.96 kcal/mol via the reaction path $I^L_1$1 - $T^L_1$1 - $I^L_1$2, demonstrating that the less stable linear isomer is more reactive.

The role of Fe_2O_3 isomer structure on NH_3 adsorption and first hydrogen atom

transfer was previousely studied by Xie *et al.*[165] They performed DFT-D3 calculations on the adsorption mechanisms of different molecules (NH_3, NO, O_2) on activated carbon (AC) supported iron-based catalysts Fe_xO_y/AC. The calculated adsorption electronic energies of NH_3 were -37.4 kcal/mol and -53.7 kcal/mol on different isomers of Fe_2O_3/AC, and the first hydrogen atom transfer had an activation barrier of 15.5 kcal/mol. Similarly, the adsorption and dehydrogenation of ammonia on different metal oxides were investigated by Erdtman and co-workers[168] for the application of gas sensors. They reported that the adsorption energy of NH_3 on the RuO_2(110) surface is -38.24 kcal/mol, and the first N−H bond cleavage had an activation energy barrier of 17.45 kcal/mol.

The third step of the NH_3 dehydrogenation reaction (6.3) involves the dissociation of the adsorbed NH_2^* intermediate into NH^* and H^* species. In this step, the abstracted hydrogen atom transfers to one of the oxygen atoms in the strctures. Figure 29(a) demonstrates, that in the case of the kite-like structure the energy barriers for this step are 43.91 kcal/mol and 34.51 kcal/mol, corresponding to the reaction paths $I_1'2$ - $T_1'2$ - $I_1'3$ and $I_1''2$ - $T_1''2$ - $I_1''3$, respectively.

In the fourth step (6.4), the adsorbed NH^* intermediate further dissociates into N^* and H^* species as shown in Fig. 29(a). The reaction barriers associated with this step are 46.98 kcal/mol and 8.95 kcal/mol for the two-coordinated and three-coordinated reaction paths, respectively. The decomposition of NH_3 on kite-like structures becomes endothermic starting from the third step (6.3). My calculations reveal that NH_3 dehydrogenation has a high energy barrier when the NH_3 molecule is adsorbed at a two-coordinated Fe site, which is the most stable adsorption site. On the other hand, dehydrogenation of the adsorbed NH_3 at a three-coordinated Fe site has a considerably lower activation barrier of 8.95 kcal/mol for the reaction step (6.4).

Overall, for the NH_3 decomposition reaction on the kite-like Fe_2O_3 structure, with initial NH_3 adsorption on the two-coordinated Fe atom, the rate-limiting step is the fourth reaction (6.4), with a barrier of 46.98 kcal/mol. Alternatively, for the less favorable NH_3 adsorption on the three-coordinated Fe atom, the rate-limiting step is the third reaction step (6.3), with a barrier of 34.51 kcal/mol.

The reaction pathway calculated for NH_3 decomposition on the linear-type Fe_2O_3 isomer is shown in Fig. 30(a), and respective intermediate and transition state structures are shown in Fig. 30(b). Since this structure consists of two iron atoms connected through a central oxygen, each containing a terminal oxygen, the reaction mechanism differs slightly from that of the kite-like isomer. For instance, in the third step of the reaction,

the second hydrogen from the adsorbed NH_2^* intermediate is transferred to the second terminal oxygen. The energy barrier for this step on the linear-type structure is 23.8 kcal/mol, as shown in the reaction path (I_1^L2 - T_1^L2 - I_1^L3) in Fig. 30a.

The fourth step on this isomer is not straightforward, involving the central oxygen atom breaking its bond with one of the neighboring iron atoms while forming an Fe − N − Fe bridge. This process leads to two different intermediates: the formation of the adsorbed H_2O^* and the transfer of a hydrogen atom from one side of the Fe − N − Fe bridge to the other. Subsequently, the final dehydrogenation step from the NH^* intermediate occurs, with an activation energy barrier of 34.76 kcal/mol.

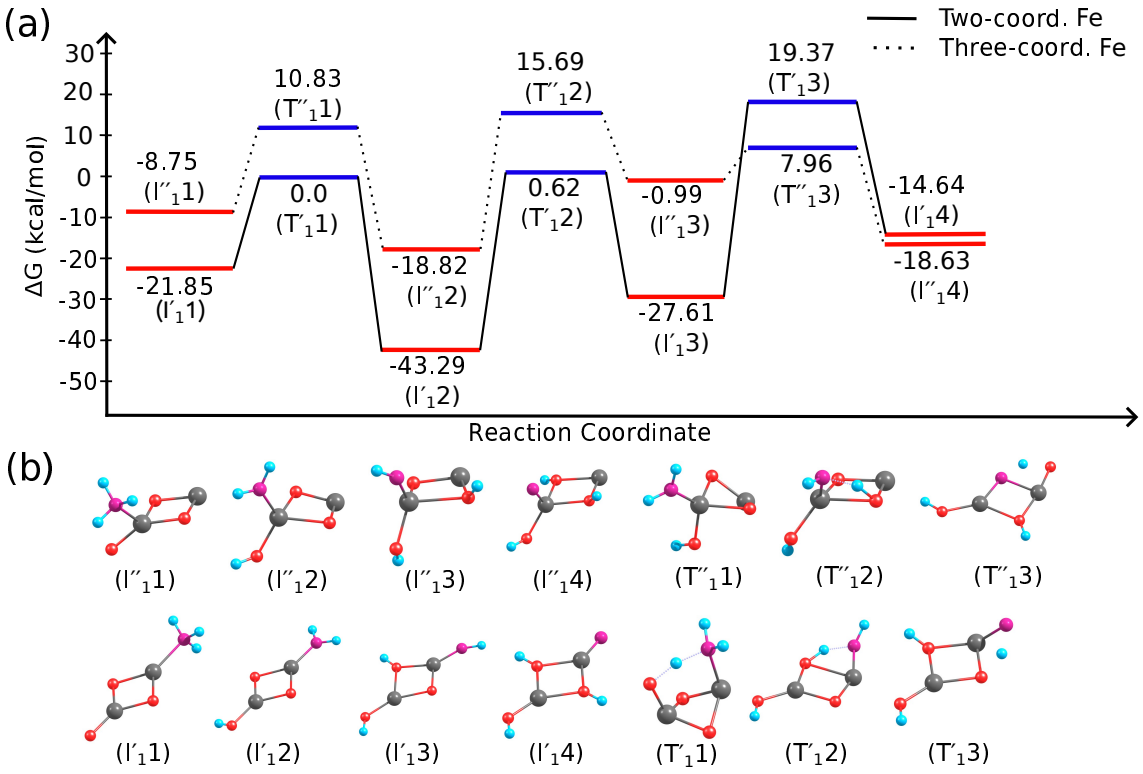


Figure 29. (a) The energy profile for $NH_3^* \rightarrow NH_2^* + H^* \rightarrow NH^* + 2H^* \rightarrow N^* + 3H^*$ reaction path on the kite-like isomer of Fe_2O_3 at T=298.15 K. (b) Geometries of the optimized equilibrium and transition states along the reaction path.

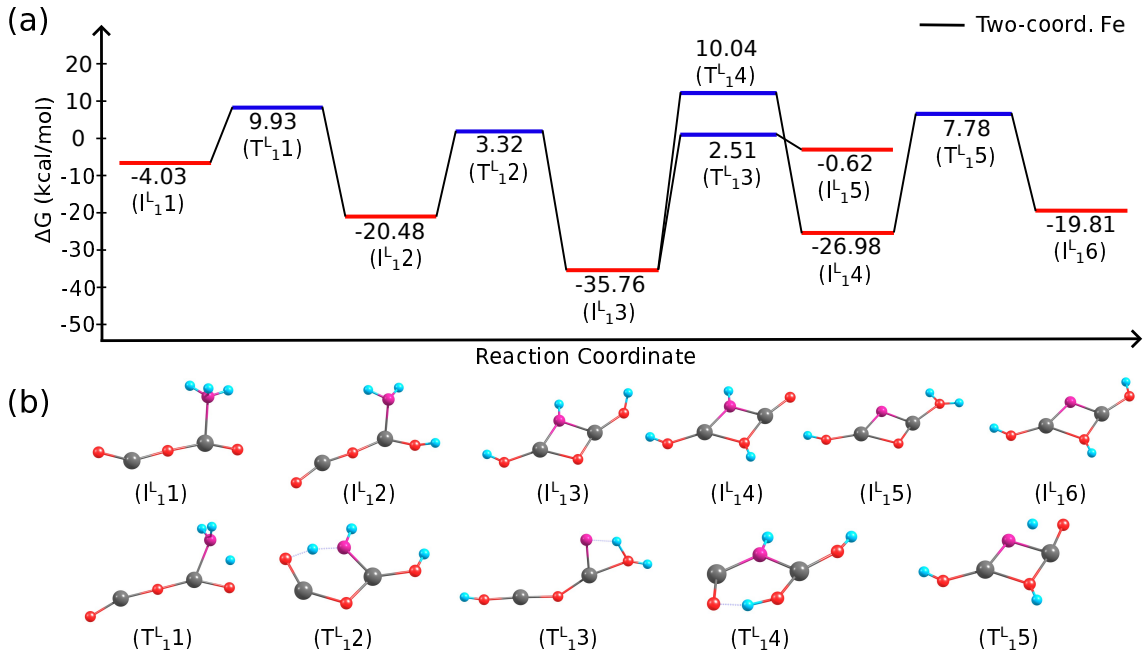


Figure 30. (a) The energy profile for $NH_3^* \rightarrow NH_2^* + H^* \rightarrow NH^* + 2H^* \rightarrow N^* + 3H^*$ reaction path on the linear-type isomet of Fe_2O_3 at T=298.15 K. (b) Geometries of the optimized equilibrium and transition states along the reaction path.

As a next step I consider possible H_2 formation via reactions (6.5) and (6.6) on the kite-like and linear isomers of Fe_2O_3. The possible pathways for H_2 formation in the case of the most stable ammonia adsorption on the two-coordinated site (I′ intermediates) of the kite-like Fe_2O_3 isomer are shown in Fig. 31(a), while the corresponding structures of the optimized equilibrium and transition states along the reaction path are illustrated in Fig. 31(b).

Note that H_2 formation can occur after partial decomposition of ammonia in reaction (6.5), starting from intermediate (I_1^I3) via the path $I'_1$3 - $T'_1$6 - $I'_1$7 - $T'_1$7 - $I'_1$8. On the other hand, H_2 formation can occur via full decomposition of ammonia in reaction (6.6), through the intermediate (I_1^I4) via the path $I'_1$4 - $T'_1$4 - $I'_1$5 - $T'_1$5 - $I'_1$6. In both cases, the reaction pathways include breaking one O−H bond and forming an Fe−H bond. The H_2 formation barriers through these intermediates are 89.74 kcal/mol and 92.49 kcal/mol, respectively. From these results, we conclude that H_2 formation on the kite-like Fe_2O_3 structure is more favorable via reaction (6.5), with the NH^* intermediate remaining adsorbed on the iron oxide structure. The H_2 formation reaction, starting from (I_1^I4), is the rate-limiting step in molecular hydrogen formation on the kite Fe_2O_3.

Similarly, the H_2 formation reaction pathways on the linear-type structure of Fe_2O_3 are shown in Fig. 32(a), while the optimized equilibrium and transition states along

the reaction path are illustrated in Fig. 32(b). The H_2 formation through the NH^* intermediate (I_1^L4) via the reaction path I_1^L4 - T_1^L8 - I_1^L9 - T_1^L9 - I_1^L10 has an energy barrier of 79.99 kcal/mol. On the other hand H_2 formation through intermediate (I_1^L6) via reaction path I_1^L6 - T_1^L6 - I_1^L7 - T_1^L7 - I_1^L8 has an activation energy of 70.84 kcal/mol, which is about 10 kcal/mol lower energy than reaction path through intermediate (I_1^L4).

Overall, on the basis of my calculated reaction pathways for H_2 formation show similar pattern for both kite-type and linear-type Fe_2O_3, where H_2 formation in reactions (6.5) and (6.6) take place via breaking one of O−H bond and forming intermediate Fe−H bond. However, from both thermodynamic and kinetic perspectives, H_2 formation on the two types of Fe_2O_3 structures varies. Reaction (6.5) is more favorable on the kite-like structure, while reaction (6.6) is more favorable on the linear structure. This highlights that the rate-limiting step for H_2 formation is highly dependent on the catalyst's structure.

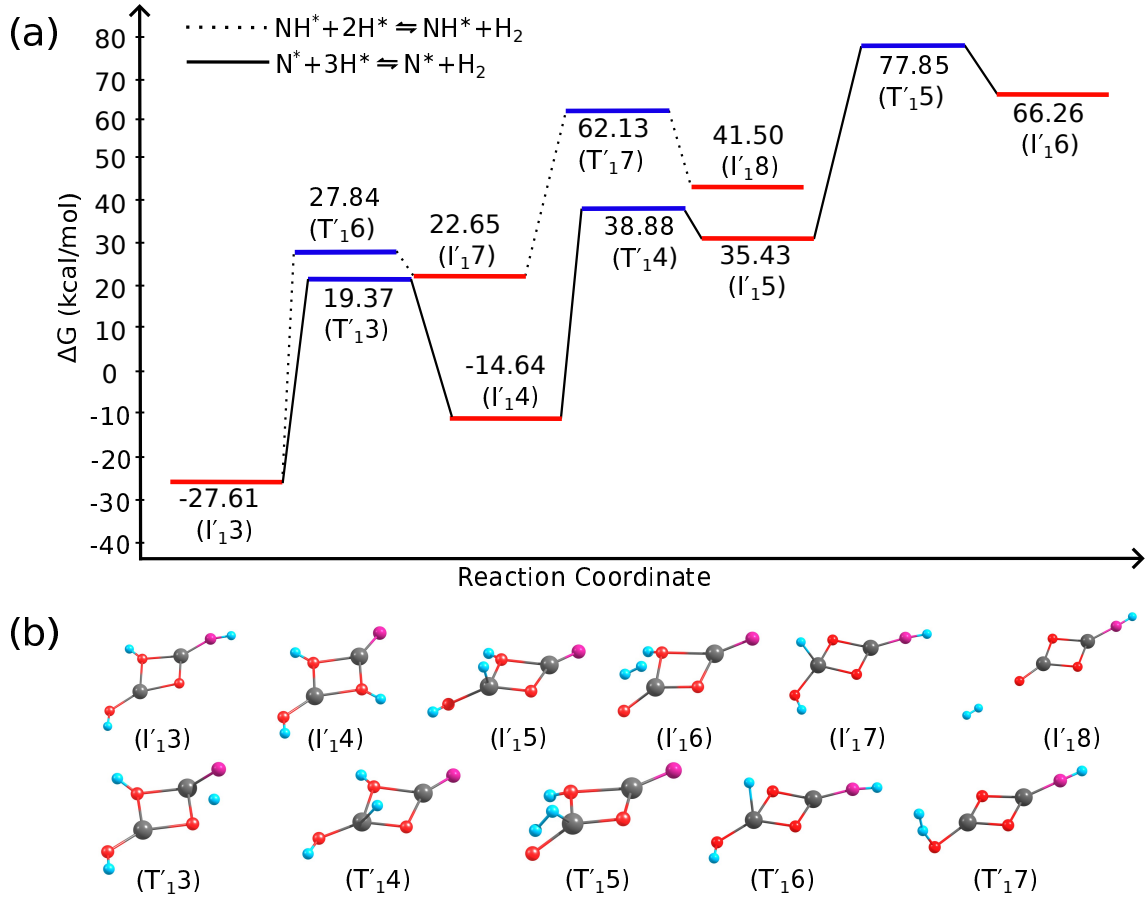


Figure 31. (a) The energy profile for H_2 formation on the kite-like Fe_2O_3 structure at T=298.15 K. (b) Geometries of the optimized equilibrium and transition states along the reaction path.

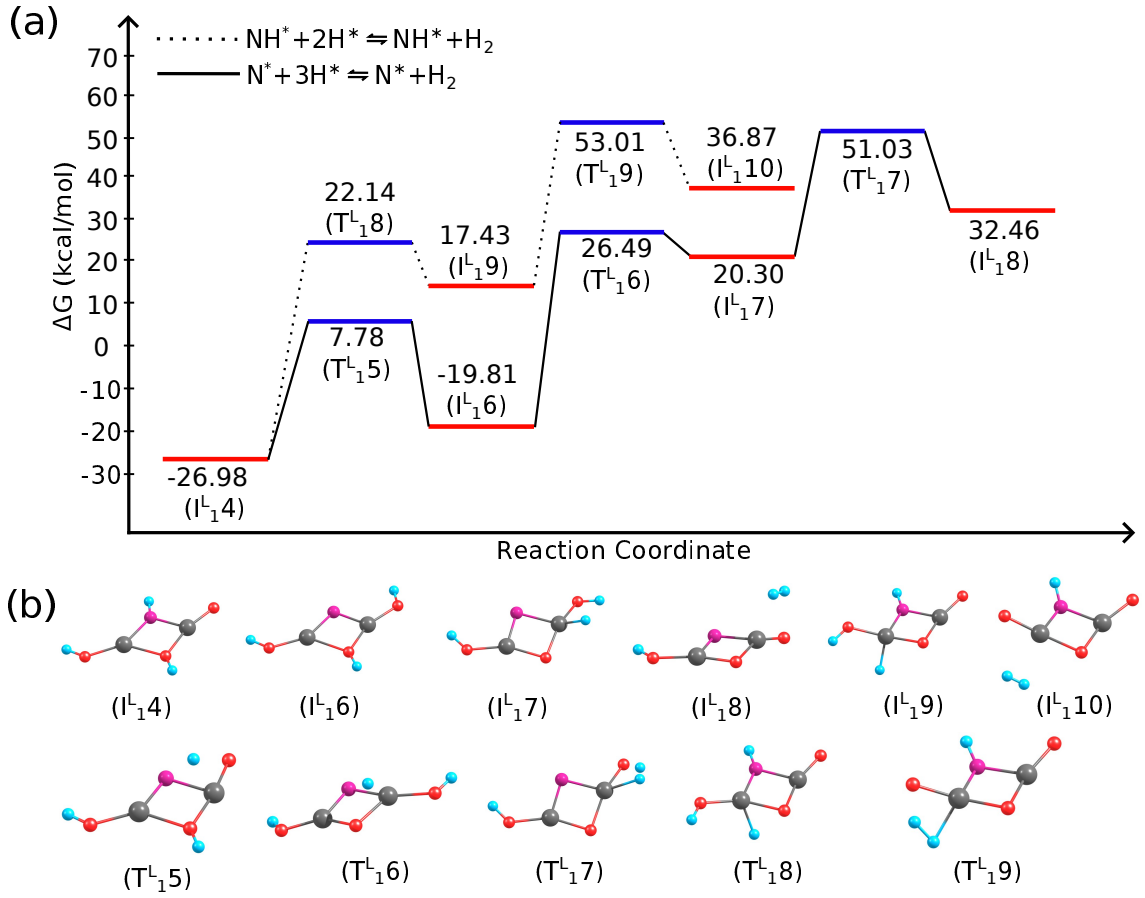


Figure 32. (a) The energy profile for H_2 formation on the linear isomer of the Fe_2O_3 at T=298.15 K. (b) Geometries of the optimized equilibrium and transition states along the reaction path.

6.2.4 NH_3 decomposition on Fe_4O_6

In the following subsection, I discuss the catalytic activity of $(Fe_2O_3)_2$ towards NH_3 dehydrogenation and H_2 formation reactions. On the basis of adsorption characteristics discussed in 6.2.2, the threefold coordinate Fe^{3+} site of the Fe_4O_6 is the most stable site for NH_3 adsorption. Complete reaction pathway for stepwise decomposition of NH_3 and formation of H_2 reactions on $(Fe_2O_3)_2$ are depicted in Fig. 33(a), and the corresponding intermediate and transition state structures are shown in Fig. 33(b). From this point forward, the first dehydrogenation step follows starting from the intermediate ($I_2$1) where NH_3 molecule interacting with three-coordinated Fe site of $(Fe_2O_3)_2$ by transferring a hydrogen to its one of neighboring oxygen via reaction pathway ($I_2$1 - $T_1$1 - $I_2$2) and reaction barrier of this step is 23.35 kcal/mol which is 1.5 kcal/mol higher energy barrier than first hydrogen transfer on kite-like Fe_2O_3. This reaction also involves different isomer of $(Fe_2O_3)_2$, where decomposition takes place on the second

minima isomer of $(Fe_2O_3)_2$ shown in Fig. S3. Relative binding energy of second minima isomer is 2.35 kcal/mol. The second dehydrogenation step follows from adsorbate NH_2^* intermediate ($I_2$2) further dissociate to NH^* + $2H^*$ which dissociated hydrogen atom subsequently transferred to another neighboring oxygen as shown in the reaction path ($I_2$2 - $T_2$2 - $I_2$3). This reaction occurs with energy barrier of 38.57 kcal/mol. The ultimate dehydrogenation step is the formation of N^* + $3H^*$ where N is bound to the central top Fe^{3+} and all the hydrogen atoms interact with three neighboring oxygens. The last dehydrogenation step occurs with the energy barrier 3.86 kcal/mol higher than the energy barrier of the second dehydrogenation step and it is shown in the reaction pathway ($I_2$3 - $T_2$3 - $I_2$4). It suggests that dehydrogenation of adsorbate NH^* is rate-determining step on $(Fe_2O_3)_2$. Moreover, from a thermodynamic viewpoint calculated dehydrogenation steps of NH_3 on $(Fe_2O_3)_2$ is endothermic by 8.12, 18.6, and 23.78 kcal/mol.

Considering H_2 formation reactions via two reaction pathways. First H_2 formation reaction (6.5) occurs with partial decomposition of NH_3 starting from intermediate ($I_2$3) through ($I_2$9). The first stage through this reaction path starting from ($I_2$3), the transition state ($T_2$6) was found that the H atom adsorbed on the Fe atom and formed a Fe−H bond. In the second stage of the reaction, the transition state ($T_2$7) was the one that splits the adsorbed H atom from the adjacent O atom to adsorbed NH^*. Then, the dissociated H atom was adsorbed in the O atom which is an adjacent atom to the Fe−H bond, and at the final stage, the dissociative molecular H_2 formed via ($T_2$8), and barrier of this reaction is 91.1 kcal/mol.

Completed reaction pathway for reaction (6.5) is ($I_2$3 - $T_2$6 - $I_2$7 - $T_2$7 - $I_2$8 - $T_2$8 - $I_2$9). The second H_2 formation reaction (6.6) is that occurs with fully decomposed NH_3 molecule starting from intermediate ($I_2$4) through intermediate ($I_2$6). It is important to note that last dehydrogenation reaction (6.4) is the one which has the highest barrier on the $(Fe_2O_3)_2$. So dissociative molecular hydrogen formation through this reaction path cost an energy as shown in reaction path ($I_2$4 - $T_2$4 - $I_2$5 - $T_2$5 - $I_2$6). Overall, as it seen from depicted reaction pathways in Fig. 33, H_2 formation reaction is kinetically and energetically costly in reaction $N^* + 3H^* \rightarrow N^* + H^* + H_2$, and it is more favorable via reaction $NH^* + 2H^* \rightarrow NH^* + H_2$ which is partial decomposition of NH_3 on $(Fe_2O_3)_2$.

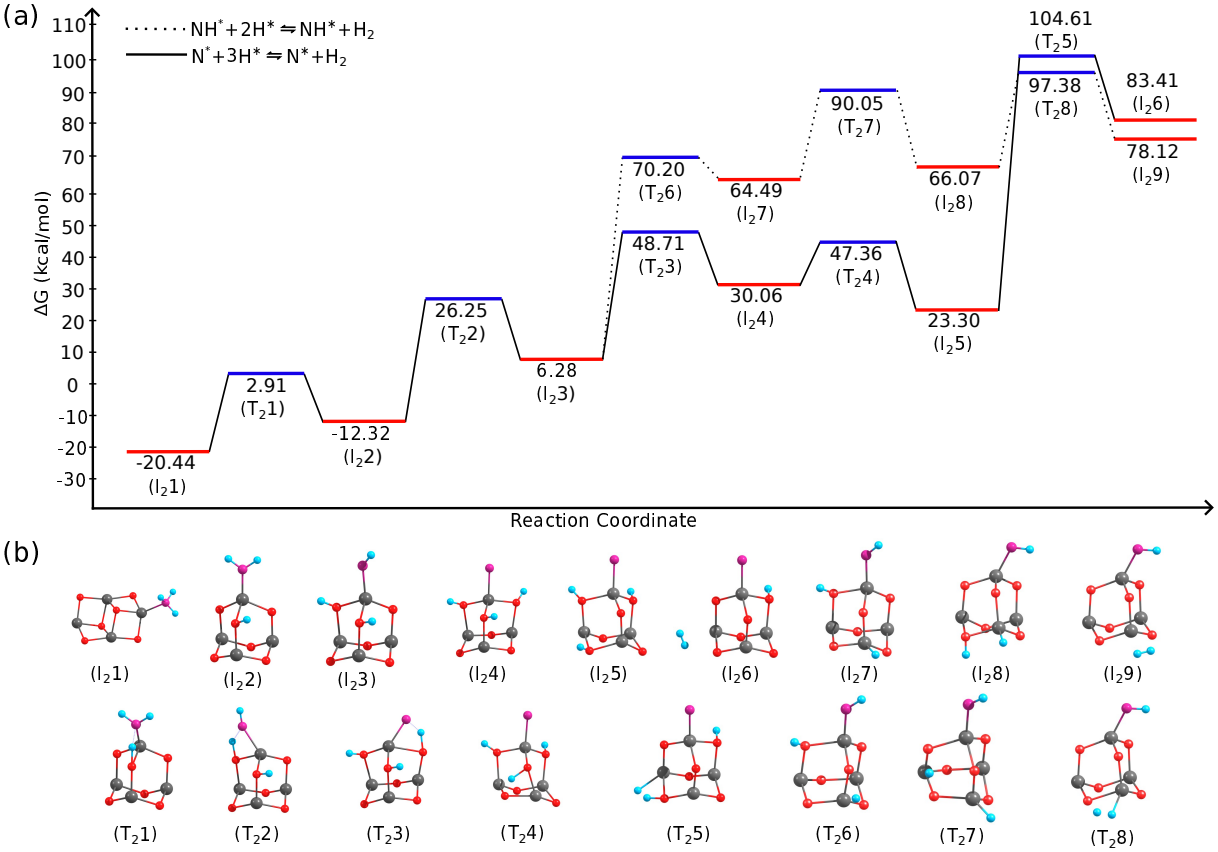


Figure 33. (a) The energy profile for $NH_3^* \rightarrow NH_2^* + H^* \rightarrow NH^* + 2H^* \rightarrow N^* + 3H^*$ and H_2 formation reaction paths on the $(Fe_2O_3)_2$ at T=298.15 K. (b) Geometries of the optimized equilibrium and transition states along the reaction path.

6.2.5 NH_3 decomposition on Fe_6O_9

The energy profile for the stepwise dehydrogenation of NH_3 on the $(Fe_2O_3)_3$ is presented in Fig. 34(a), while the intermediate and transition state structures along this reaction pathway are shown in Fig. 34(b). The dissociation of NH_3 on the $(Fe_2O_3)_3$ is more complex compared to smaller Fe(III) oxide structures, as NH_3 can adsorb at various sites on the $(Fe_2O_3)_3$ surface.

I identified the most favorable adsorption configuration, $I_3 1$, with an adsorption energy of $\Delta G = -18.8$ kcal/mol, from which the stepwise decomposition reaction proceeds. The first dehydrogenation reaction, as described in (6.2), begins with NH_3^* adsorbed on the $(Fe_2O_3)_3$ as $I_3 1$ and proceeds through the transition state $T_3 1$. The energy barrier along this pathway is 20.04 kcal/mol, which is lower than the barrier for the first H abstraction from NH_3 on the $(Fe_2O_3)_2$. Although the first dehydrogenation

reaction on the $(Fe_2O_3)_3$ is endothermic, I observed that when the NH_2^* species migrates to a bridging position between two Fe atoms (Fe − N − Fe), the reaction becomes exothermic by 14.15 kcal/mol, as shown in the reaction pathways $I_32 - T_32 - I_33$ and $I_33 - T_33 - I_34$.

The second H abstraction involves the further dehydrogenation of NH_2^* into NH^* and H^*, with an energy barrier of 35.97 kcal/mol along the pathway $I_34 - T_34 - I_35$. This barrier is 15.96 kcal/mol higher than that of the first dehydrogenation step. Additionally, this reaction is endothermic, with a reaction energy of 15.74 kcal/mol.

Similarly, in the third step (6.4), the remaining NH^* dissociates into N^* and H^*, with an energy barrier 17.94 kcal/mol higher than that of the second dissociation step. This is the largest barrier encountered in the decomposition of NH_3. The calculated reaction pathway indicates that this process is endothermic, with a reaction energy of 25.76 kcal/mol.

Lastly, the possible H_2 formation reactions (6.5 and 6.6) on the $(Fe_2O_3)_3$ were calculated, as shown in Fig. 34. The first H_2 formation reaction (6.5) begins with one adsorbed NH^* and two H^* species on the $(Fe_2O_3)_3$. The reaction proceeds in a manner similar to that discussed in the previous subsection: the adsorbed H^* on oxygen, adjacent to the NH^* adsorbed on Fe, migrates away by forming Fe−H bonds through transition states T_37 and T_38. The overall energy barrier for H_2 formation via reaction (6.5) is 100.74 kcal/mol.

The second possible H_2 formation pathway starts from fully decomposed NH_3 (I_36) and proceeds through the transition state T_36. This pathway has a significantly high energy barrier, calculated to be 116.89 kcal/mol, as shown in the reaction path $I_36 - T_36 - I_37$. These results suggest that, from both a thermodynamic and kinetic perspective, H_2 formation after full dehydrogenation of NH_3 is less favorable.

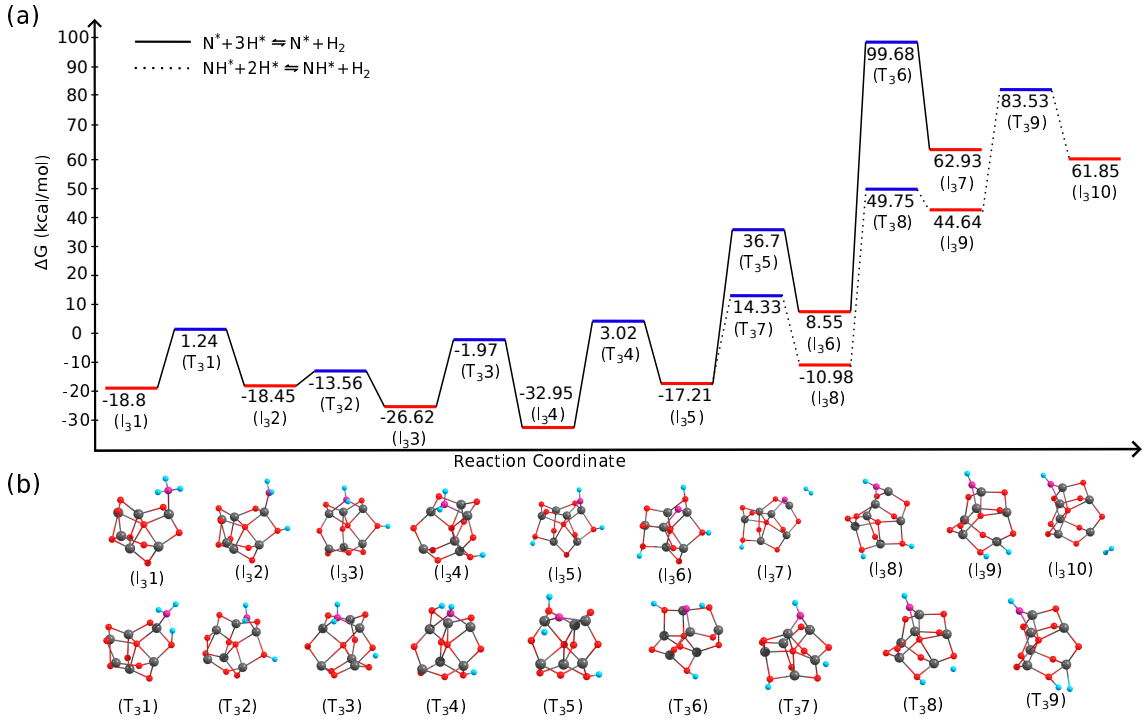


Figure 34. (a) The energy profile for $NH_3^* \rightarrow NH_2^* + H^* \rightarrow NH^* + 2H^* \rightarrow N^* + 3H^*$ and H_2 formation reaction paths on the $(Fe_2O_3)_3$ at T=298.15 K. (b) Geometries of the optimized equilibrium and transition states along the reaction path.

6.2.6 NH_3 decomposition on Fe_8O_{12}

Finally, the decomposition of NH_3 and the H_2 formation pathways on the $(Fe_2O_3)_4$ are illustrated in Fig. 35(a), with the intermediate and transition state structures shown in Fig. 35(b). As discussed in previous subsections, increasing the number of units n in $(Fe_2O_3)_n$ increases the number of active sites that interact with NH_3. However, similar to the reactions on $(Fe_2O_3)_n$ ($n = 2, 3$), the most stable adsorption site for NH_3 on $(Fe_2O_3)_4$ is a three-coordinated Fe site, with an adsorption energy of -19.2 kcal/mol at room temperature, slightly higher than that on $(Fe_2O_3)_3$. The dehydrogenation of NH_3 begins with the adsorption of NH_3^*, as shown in the intermediate state $I_4$1. The first dehydrogenation step involves breaking one N−H bond and forming an O−H bond, with an energy barrier of 19.74 kcal/mol, as shown in the reaction pathway $I_4$1 − $T_4$1 − $I_4$2. The second dehydrogenation step (6.3) involves the dissociation of $NH_2^* + H^*$ to form $NH^* + 2H^*$, proceeding through the transition state $T_4$2. The energy barrier for this step is 43.96 kcal/mol, which is higher than the corresponding second dehydrogenation steps on $(Fe_2O_3)_n$ ($n = 1 - 3$). The final dehydrogenation step occurs along the pathway $I_4$3 − $T_4$3 − $I_4$4, with a barrier of 42.24 kcal/mol. All NH_3 dehydrogenation steps on

$(Fe_2O_3)_4$ are endothermic, with reaction energies of 1.11 kcal/mol, 15.39 kcal/mol, and 41.47 kcal/mol, respectively.

The final reaction pathway on the $(Fe_2O_3)_4$ involves H_2 formation from both partially and fully decomposed NH_3, as described in (6.5) and (6.6). As observed for all sizes of $(Fe_2O_3)_n$, H_2 formation is energetically more favorable after the partial decomposition of NH_3 in reaction (6.5) compared to the fully decomposed pathway (6.6). However, this pathway also presents the highest energy barrier on this molecular structure of iron trioxide.

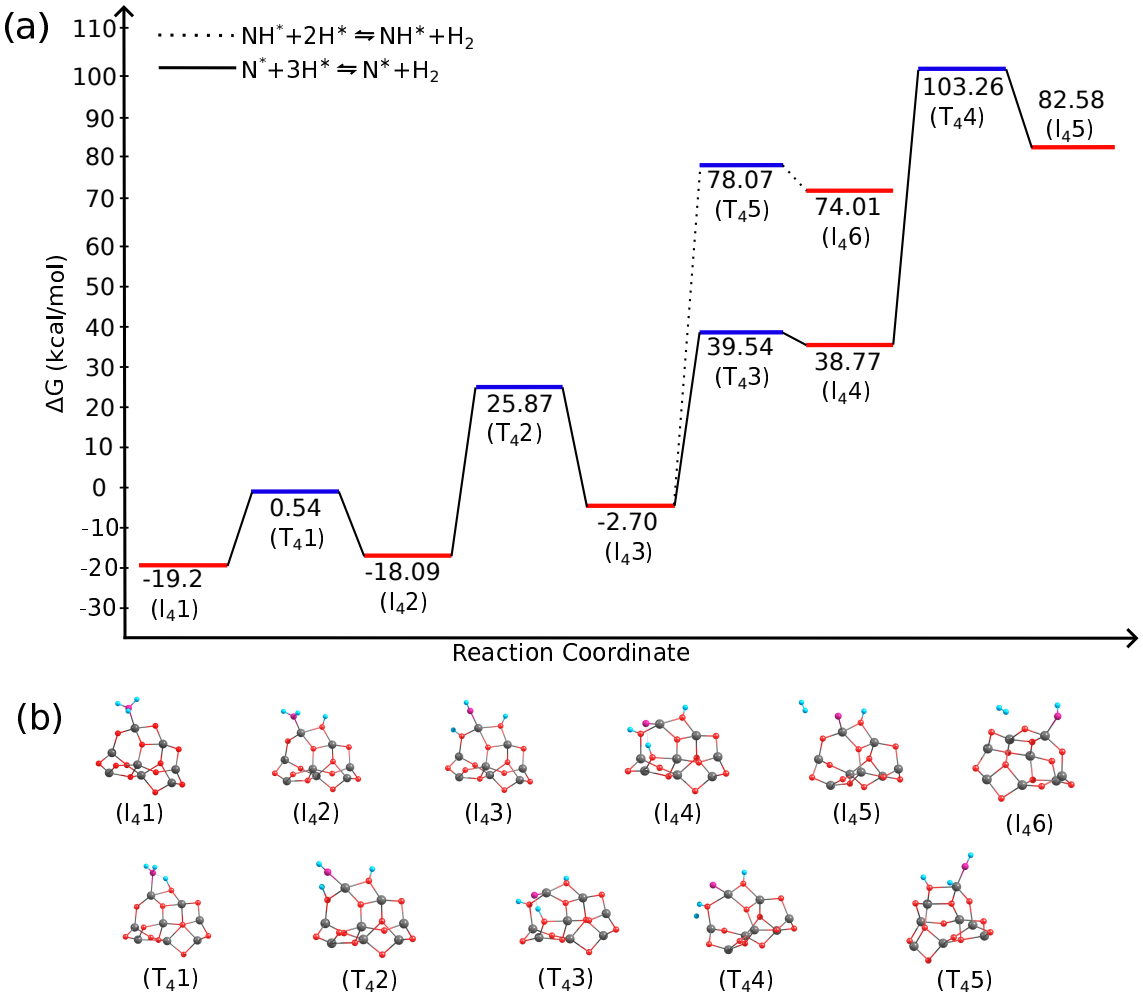


Figure 35. (a) The energy profile for $NH_3^* \rightarrow NH_2^* + H^* \rightarrow NH^* + 2H^* \rightarrow N^* + 3H^*$ and H_2 formation reaction path on the $(Fe_2O_3)_4$ at T=298.15 K. (b) Geometries of the optimized equilibrium and transition states along the reaction path.

7 Comparison and conclusion

Nanoparticles composed of transition metal oxides are, in essence, large molecules. Portions of their structure may be periodic ("crystalline"), but this is not necessarily the case. Providing a theoretical description of such systems is inherently difficult, because the number of possible stoichiometric spatial configurations is very large and only a small subset may possess any symmetry. Imposing symmetry constraints therefore automatically narrows the analysis and causes loss of information about the true lowest-energy structures, as became clear in this work.

A deeper examination of the stoichiometric geometries and spin states of iron(III) and cobalt(III) oxides leads to several new conclusions. The lowest-energy iron trioxide is a ferromagnetic nonet ($S = 4$) kite isomer, as established by the B3LYP/aug−cc−pVTZ computations. The antiferromagnetic singlet is also a very low-energy configuration, lying only approximately 10 kcal/mol above the nonet state. More generally, iron(III) oxide isomers are most stable at high spin or in the antiferromagnetic configuration; in both cases, a large number of singly occupied molecular orbitals are present. These findings differ from those of Sierka et al. [31; 32], who claimed the lowest-energy iron trioxide to be a kite structure with an antiferromagnetic electronic configuration exclusively. My results show that low-spin non-magnetic states of ferric oxide are markedly less stable than high-spin or antiferromagnetic states, regardless of the quantum-chemical method employed, a conclusion further confirmed using spin-restricted Kohn–Sham orbitals for ferromagnetic states. For cobalt trioxide, the lowest-energy state is the antiferromagnetic linear isomer, while the ferromagnetic linear nonet is also a low-energy structure according to the DFT computations.

These observations carry important implications. Neither a spatial nor a spin configuration should be deliberately excluded from consideration, because spin-state and geometric transitions cannot be ruled out along reaction pathways, during synthesis, or in other processes. Even when antiferromagnetic configurations are set aside, the

energy differences between high-spin and low-spin states remain relatively large, supporting the conclusion that the final particles and intermediate oxides formed during the synthesis of cobalt(III) and iron(III) oxide nanosystems are most likely high-spin or antiferromagnetic. The same tendency holds for the cations and anions formed after one-electron redox reactions: higher-spin states are consistently preferred, or alternatively the antiferromagnetic configuration. An additional asymmetry is observed between the cationic and anionic species: $Fe_2O_3^+$ isomers favor higher spin states than $Fe_2O_3^-$ isomers, while the reverse is true for the corresponding cobalt oxide species.

Regarding the redox properties, the one-electron reduction characteristics of cobalt and iron trioxides are broadly similar, though the calculated ionization potentials, electron affinities, and standard reduction potentials are consistently higher for cobalt oxides. The computed standard one-electron reduction potentials are lower than the values conventionally reported for aqua salts, and they depend on the molecular geometry. The kite isomers of both Fe_2O_3 and Co_2O_3 are the most susceptible to one-electron reduction, while the linear configurations of both oxides are the least susceptible to oxidation, owing to their largest ionization potentials. It is reasonable to expect that larger $(Me_2O_3)_n$ analogues with greater n would exhibit similar redox trends, provided that comprehensive investigations of all plausible spin and spatial configurations are carried out. This remains computationally challenging, as the results depend sensitively on the quality of the quantum-chemical algorithms and on the accurate representation of ionic states.

Turning to the catalytic findings, my results indicate that NH_3 dehydrogenation can be a thermodynamically favorable reaction on $(Fe_2O_3)_n$ ($n = 1$–4), though the favorability depends on both the size and geometry of the iron trioxide cluster and on the specific reaction step. Across all reactions studied, ΔG increases with temperature. NH_3 dehydrogenation on $(Fe_2O_3)_n$ ($n = 2, 4$) can be energetically favorable at moderate temperatures, while above a certain threshold it becomes unfavorable. For $n = 1$, all dehydrogenation reactions are energetically favorable within the full range of temperatures considered (0–1000 K). For $n = 2$ and $n = 4$, only the final dehydrogenation step is rate-limiting, and since ΔG of the third step already exceeds zero at 0 K, that step is not favorable at any temperature. The $n = 3$ cluster exhibits better stabilization of reaction intermediates during the second dehydrogenation step, which remains favorable up to 800 K, whereas for $n = 4$ this step is favorable only up to 400 K. The most endothermic step on the $n = 4$ structure is $NH^* + 2H^* \rightarrow N^* + 3H^*$, while the first and second dehydrogenation steps are favorable up to 1100 K and 700 K, respectively. The formation of

molecular hydrogen is not thermodynamically favorable at any temperature on any of the clusters studied; however, if sufficient energy is available to overcome the activation barrier, the reaction can still proceed.

A comparison of the energy barriers for each elementary step in NH_3 decomposition and H_2 formation across different sizes and shapes of $(Fe_2O_3)_n$ ($n = 1$–4) is shown in Fig. 36. The rate-determining step varies with cluster size. For $n = 1$–3, the rate-determining step in ammonia dehydrogenation is $NH^* \rightarrow N^* + H^*$, whereas for $n = 4$ it is the second N–H dissociation step, $NH_2^* \rightarrow NH^* + H^*$. The final H_2 formation step consistently exhibits the highest energy barrier across all cluster sizes, yet the lowest barrier for H_2 formation is associated with the largest molecule considered, $(Fe_2O_3)_4$. The first dehydrogenation step shows a nearly uniform barrier across all structures, being exothermic for $n = 1$ and $n = 3$ and endothermic for $n = 2$ and $n = 4$. For the second dehydrogenation step, the $n = 3$ cluster demonstrates substantially higher activity compared to the other sizes. It is also noteworthy that the $n = 1$ linear configuration is the only Fe_2O_3 structure containing two terminal O^{2-} ions, a structural feature that may promote enhanced activity toward NH_3 dehydrogenation and H_2 formation.

These catalytic trends are consistent with the adsorption behavior. The NH_3 molecule adsorbs preferentially at two-coordinated Fe sites for $n = 1$, and at three-coordinated Fe sites for $n = 2$–4. The adsorption energy decreases from $n = 1$ to $n = 3$, then slightly increases for $n = 4$. From a thermodynamic standpoint, NH_3 adsorption on Fe_2O_3 ($n = 1$) is favorable across the entire temperature range considered (0–1200 K), while for the larger clusters ($n = 2, 3, 4$), adsorption becomes energetically unfavorable at 1140 K, 940 K, and 989 K, respectively.

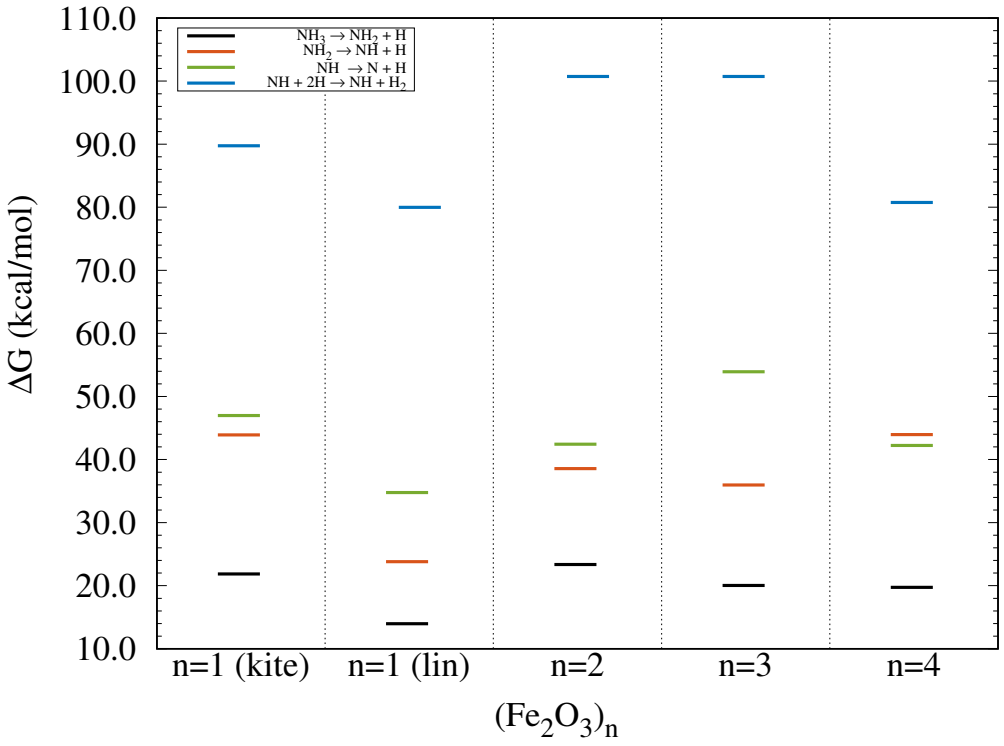


Figure 36. Reaction barrier ($\Delta G^{\ddagger}$) for NH_3 dehydrogenation and H_2 formation reactions on $(Fe_2O_3)_n$ ($n = 1 - 4$).

In this dissertation, various structures of $(Fe_2O_3)_n$ ($n = 1$–4) were obtained using the SC-AFIR method, and the ammonia decomposition and molecular hydrogen formation pathways on the most stable isomers were investigated by means of the SC-AFIR and DS-AFIR methods within the Global Reaction Route Mapping (GRRM) strategy, employing the B3LYP exchange-correlation functional in Kohn–Sham DFT.

Taken together, the results of this dissertation establish a comprehensive picture of the structural, electronic, and catalytic properties of iron(III) oxide nanoclusters. The combination of high-level electronic structure calculations with systematic exploration of spin and spatial configurations reveals that high-spin and antiferromagnetic states are consistently the most relevant, that redox properties are geometry-dependent, and that catalytic activity in NH_3 decomposition is strongly size-dependent. I believe these findings provide a solid foundation for the rational design of iron trioxide-based nanocatalysts, in which the size and geometry of $(Fe_2O_3)_n$ can be tuned to enhance H_2 production from the catalytic decomposition of ammonia.

Appendices

Supporting Information



Table 5. Relative energies (ΔE, kcal/mol) calculated using 6-31+G* and aug-cc-pVTZ basis sets with respect to the lowest energy state of kite-like Fe_2O_3 across three different DFT functionals.

	B3LYP		M06		wB97XD	
	6-31+G*	aug-cc-pVTZ	6-31+G*	aug-cc-pVTZ	6-31+G*	aug-cc-pVTZ
Spin						
0	0.62	8.88	0.29	0.81	0.57	6.64
4	0.0	0.0	0.0	0.0	0.0	0.0
5	4.75	12.15	4.42	5.41	3.44	10.35

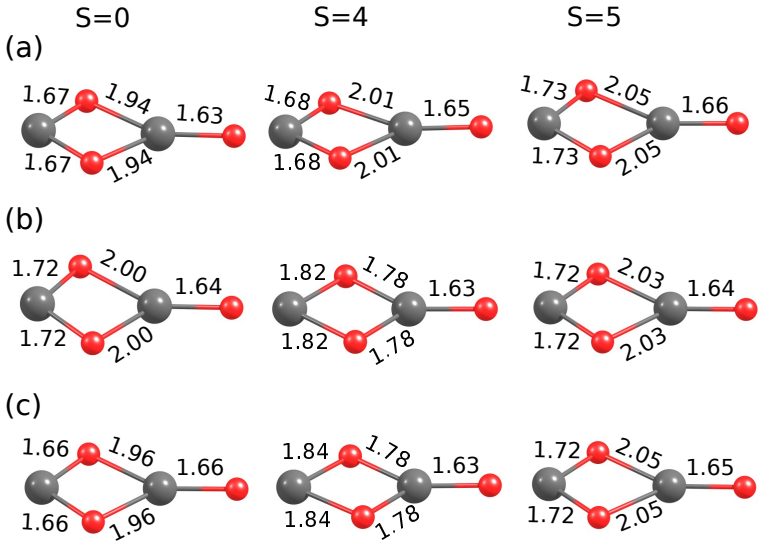


Figure 37. Structures and Fe-O bond lengths of Fe_2O_3 with total spins $S = 0$, 4, and 5. The bond lengths are given in Å. (a) B3LYP/6-31+G*, (b) M06/6-31+G*, and (c) wB97XD/6-31+G*.

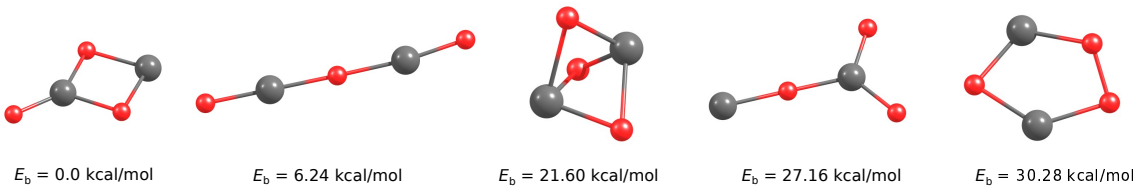


Figure 38. The lowest energy isomers of Fe_2O_3 with total spin S=4. The binding energies, E_b, are shown in inserts.

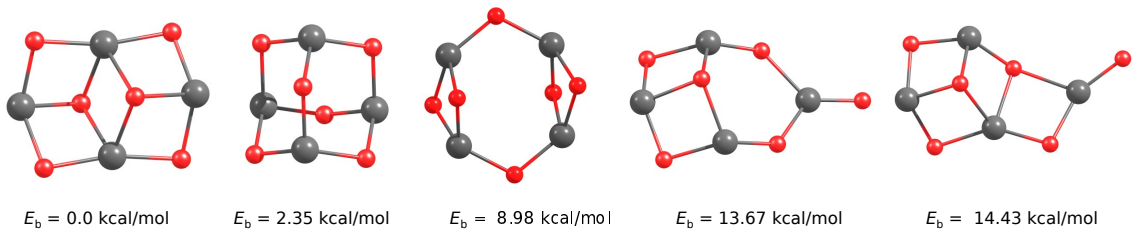


Figure 39. The lowest energy isomers of $(Fe_2O_3)_2$ with total spin S=10. The binding energies, E_b, are shown in inserts.

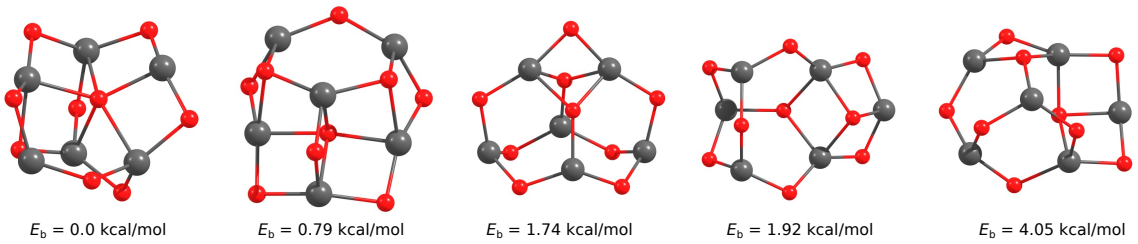


Figure 40. The lowest energy isomers of $(Fe_2O_3)_3$ with total spin S=15. The binding energies, E_b, are shown in inserts.

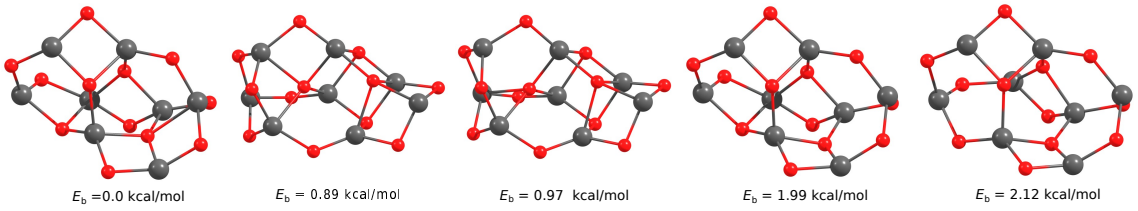


Figure 41. The lowest energy isomers of $(Fe_2O_3)_4$ with total spin S=20. The binding energies, E_b, are shown in inserts.

The bindig energy E_b per unit n of a $(Fe_2O_3)_n$ molecule is defined as follows:

$$E_b = -\frac{E_{el}((Fe_2O_3)_n) + E_{ZPE}((Fe_2O_3)_n)) - [2nE(Fe) + 3nE(O)]}{n} \quad \text{(A.1)}$$

where $E_{\mathrm{el}}((Fe_2O_3)_n)$ and $E_{\mathrm{ZPE}}((Fe_2O_3)_n)$ are the electronic and zero-point energies of a molecule $(Fe_2O_3)_n$ with a number of units n, while E(Fe) and E(O) are the energis of free Fe and O atoms.

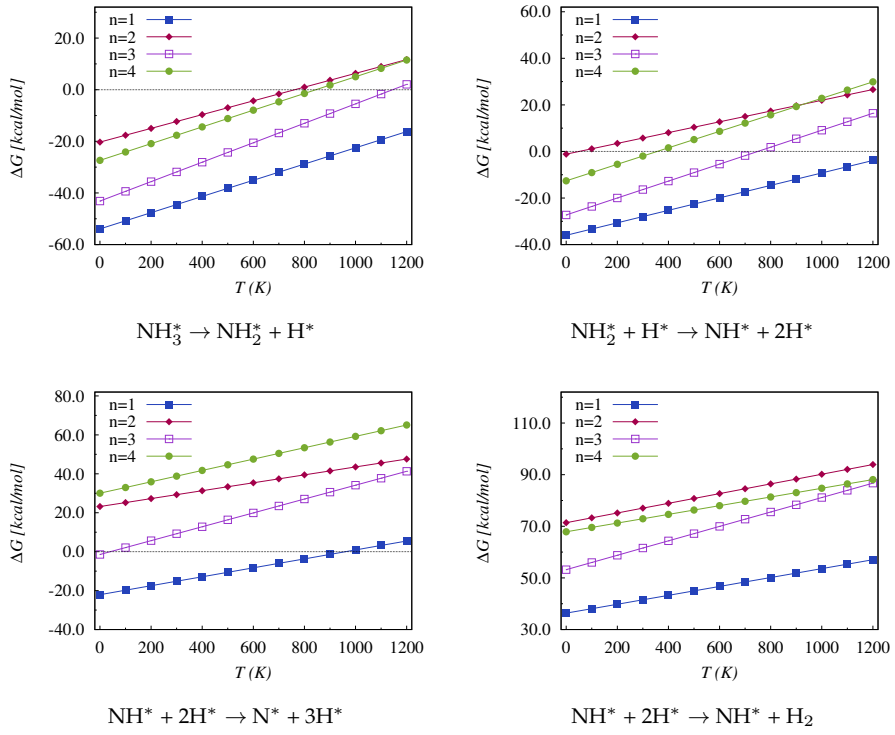


Figure 42. Variation of Gibbs free energy (ΔG) with temperature for each dehydrogenation step of NH_3 on $(Fe_2O_3)_n$ (n=1−4) molecules, along with the H_2 formation reaction $NH^* + 2H^* \rightarrow NH^* + H_2$. For simplicity, the temperature dependence of entropy, $S(T)$, was neglected.

Participation another research projects

B

During my PhD study, I have participated at several research projects. Here are the lest of scientific research projects that I participated

1. Participation in HORAZON 2020 project MAGENTA (MAGnetic nanoparticle based liquid energy materials for Thermoelectric device Applications)

2. Pariticipation in project ”STE(E)R-ING towards Internatinal Doctoral School” Gdansk University of Technology, Poland

3. Pariticipation in project MANABIYA program, Hokkaido University, Institute for Chemical Reaction, Design and Discovery, Japan

C Scientific Achievements

Scientific Publications:

1. Wtulich, M., Skwierawska, A., Ibragimov, S., Lisowska–Oleksiak, A. (2024). Exploring the role of carbon nitrides (melem, melon, g-C3N4) in enhancing photoelectrocata- lytic properties of TiO2 nanotubes for water electrooxidation. Applied Surface Sci- ence, 161994

2. Ibragimov, S., Lyalin, A., Kumar, S., Ono, Y., Taketsugu, T., Bobrowski, M. (2025). Theoretical design of nanocatalysts based on (Fe2O3) n clusters for hydrogen production from ammonia. The Journal of Chemical Physics, 162(5).

3. Soporboev, Z., Ibragimov, S., Eshchanov, K., Khudoyberganov, O., Ashirov, M., and Khasanov, S. (2025). Theoretical investigations on interactions between 2-benzoxazolinone and Cun (n= 1-13) clusters, as well as their binding properties to the N-malonyltransferase enzymes. Nanochemistry Research, e230286.

4. Ibragimov, S., Komando, L. Standard redox potential of [Co(bpy)3]2+/3+ and [Co(phen)3]2+/3+ redox couples using a density functional theory protocol. Struct Chem (2025)

5. Ibragimov, S., Komando, L., and Bobrowski, M. (2025). Isomers of Iron (III) Oxides and Cobalt (III) Oxides and Their Redox Properties: Quantum-Chemical Insights. Molecules, 30(21), 4158.

Conference Reports:

1. Poster presentation in the 31^{st} Topical meeting of the International Society of Electrochemistry, (May 15-19, 2022) Aachen, Germany . Meeting topic: Theory and Computation in Electrochemistry: Seeking Synergies in Methods, Materials and Systems.

2. Poster Presentation in the 25^{th} International Workshop on Quantum Systems in Chemistry, Physics and Biology. (June 19-24, 2022) Torun, Poland.

3. Poster Presentation in the 5^{th} Conference of Theory and Applications of Computational Chemistry, (4-9 September, 2023) Hokkaido University, Sapporo, Japan.

References

[1] K. Wandelt, Encyclopedia of interfacial chemistry: surface science and electrochemistry.

[2] K. Xie, M. Guo, H. Huang, Y. Liu, Fabrication of iron oxide nanotube arrays by electrochemical anodization, Corrosion science 88 (2014) 66–75.

[3] S. Mathur, M. Veith, V. Sivakov, H. Shen, V. Huch, U. Hartmann, H.-B. Gao, Phase-selective deposition and microstructure control in iron oxide films obtained by single-source cvd, Chemical Vapor Deposition 8 (6) (2002) 277–283.

[4] J. Nagahama, H. Yumoto, Application of fe oxide films prepared by pvd methods to protect fe metal from corrosion, Surface and Coatings Technology 169 (2003) 658–661.

[5] S. Hasany, I. Ahmed, J. Rajan, A. Rehman, Systematic review of the preparation techniques of iron oxide magnetic nanoparticles, Nanosci. Nanotechnol 2 (6) (2012) 148–158.

[6] A. Ali, H. Zafar, M. Zia, I. ul Haq, A. R. Phull, J. S. Ali, A. Hussain, Synthesis, characterization, applications, and challenges of iron oxide nanoparticles, Nanotechnology, science and applications (2016) 49–67.

[7] K. K. Priya, Naveen, S. AK, Green synthesis: An eco-friendly route for the synthesis of iron oxide nanoparticles., Frontiers in Nanotechnology (2021) 3.

[8] A. B. B. A. H. A. W. J. B. I. B. Wickman, B.; Fanta, Iron oxide films prepared by rapid thermal processing for solar energy conversion, Nature 7.

[9] S. Verma, A. K. Pathak, B. A. Rahman, Review of biosensors based on plasmonic-enhanced processes in the metallic and meta-material-supported nanostructures, Micromachines 15 (4) (2024) 502.

[10] A. Lassoued, B. Dkhil, A. Gadri, S. Ammar, Control of the shape and size of iron oxide (α-fe2o3) nanoparticles synthesized through the chemical precipitation method, Results in physics 7 (2017) 3007–3015.

[11] H. A. De Abreu, L. Guimaraes, H. A. Duarte, Density-functional theory study of iron (iii) hydrolysis in aqueous solution, The Journal of Physical Chemistry A 110 (24) (2006) 7713–7718.

[12] J.-P. J. . in collaboration with Marc Henry, J. L. . translated by Eric Bescher, Metal oxide chemistry and synthesis : from solution to solid state, John Wiley and Sons.

[13] O. Sadeghi, L. N. Zakharov, M. Nyman, Aqueous formation and manipulation of the iron-oxo keggin ion, Science 347 (6228) (2015) 1359–1362.

[14] M. Katherine, B. Pieter, J. Arne, A. Liam, B. Richard, S. Samuel, et al., Ferrihydrite formation: The role of fe13 keggin clusters.

[15] J. Combes, A. Manceau, G. Calas, J. Bottero, Formation of ferric oxides from aqueous solutions: A polyhedral approach by x-ray absorption spectroscdpy: I. hydrolysis and formation of ferric gels, Geochimica et Cosmochimica Acta 53 (3) (1989) 583–594.

[16] J. Scheck, B. Wu, M. Drechsler, R. Rosenberg, A. E. Van Driessche, T. M. Stawski, D. Gebauer, The molecular mechanism of iron (iii) oxide nucleation, The journal of physical chemistry letters 7 (16) (2016) 3123–3130.

[17] J.-P. J. E. T. C. Chanéac, Iron oxides: From molecular clusters to solid. a nice example of chemical versatility, Comptes Rendus Geoscience 338 (2006) 488–497.

[18] A. P. LaGrow, M. O. Besenhard, A. Hodzic, A. Sergides, L. K. Bogart, A. Gavriilidis, N. T. K. Thanh, Unravelling the growth mechanism of the co-precipitation of iron oxide nanoparticles with the aid of synchrotron x-ray diffraction in solution, Nanoscale 11 (14) (2019) 6620–6628.

[19] I. Rahinov, J. Sellmann, M. R. Lalanne, M. Nanjaiah, T. Dreier, S. Cheskis, I. Wlokas, Insights into the mechanism of combustion synthesis of iron oxide nanoparticles gained by laser diagnostics, mass spectrometry, and numerical simulations: a mini-review, Energy & Fuels 35 (1) (2020) 137–160.

[20] S. Laurent, D. Forge, M. Port, A. Roch, C. Robic, L. Vander Elst, R. N. Muller, Magnetic iron oxide nanoparticles: synthesis, stabilization, vectorization, physicochemical characterizations, and biological applications, Chemical reviews 108 (6) (2008) 2064–2110.

[21] F. Ahimou, F. A. Denis, A. Touhami, Y. F. Dufrêne, Probing microbial cell surface charges by atomic force microscopy, Langmuir 18 (25) (2002) 9937–9941.

[22] A. Azam, A. S. Ahmed, M. Oves, M. S. Khan, S. S. Habib, A. Memic, Antimicrobial activity of metal oxide nanoparticles against gram-positive and gram-negative bacteria: a comparative study, International journal of nanomedicine (2012) 6003–6009.

[23] R. M. Cornell, U. Schwertmann, et al., The iron oxides: structure, properties, reactions, occurrences, and uses, Vol. 664, Wiley-vch Weinheim, 2003.

[24] D. Faivre, T. U. Godec, From bacteria to mollusks: the principles underlying the biomineralization of iron oxide materials, Angewandte Chemie International Edition 54 (16) (2015) 4728–4747.

[25] S. Sun, J. Lang, R. Wang, L. Kong, X. Li, X. Yan, Identifying pseudocapacitance of fe 2 o 3 in an ionic liquid and its application in asymmetric supercapacitors, Journal of Materials Chemistry A 2 (35) (2014) 14550–14556.

[26] J. Krysa, M. Zlamal, S. Kment, M. Brunclikova, Z. Hubicka, Tio2 and fe2o3 films for photoelectrochemical water splitting, Molecules 20 (1) (2015) 1046–1058.

[27] B. Iandolo, B. Wickman, I. Zorić, A. Hellman, The rise of hematite: origin and strategies to reduce the high onset potential for the oxygen evolution reaction, Journal of Materials Chemistry A 3 (33) (2015) 16896–16912.

[28] A. B. Mohammadi, M. Pourmadadi, M. Abdouss, A. Rahdar, A. M. Díez-Pascual, Polyacrylic acid/polyvinylpyrrolidone/iron oxide nanocarrier for efficient delivery of doxorubicin, Inorganic Chemistry Communications 161 (2024) 112037.

[29] J. C. Riedl, M. A. Kazemi, F. Cousin, E. Dubois, S. Fantini, S. Lois, R. Perzynski, V. Peyre, Colloidal dispersions of oxide nanoparticles in ionic liquids: Elucidating the key parameters, Nanoscale Advances 2 (4) (2020) 1560–1572.

[30] D. Kostyukova, Y. H. Chung, Synthesis of iron oxide nanoparticles using isobutanol, Journal of Nanomaterials 2016 (1) (2016) 4982675.

[31] A. Erlebach, H.-D. Kurland, J. Grabow, F. A. Müller, M. Sierka, Structure evolution of nanoparticulate fe 2 o 3, Nanoscale 7 (7) (2015) 2960–2969.

[32] A. Erlebach, C. Hühn, R. Jana, M. Sierka, Structure and magnetic properties of (fe 2 o 3) n clusters (n= 1–5), Physical Chemistry Chemical Physics 16 (48) (2014) 26421–26426.

[33] X.-L. Ding, W. Xue, Y.-P. Ma, Z.-C. Wang, S.-G. He, Density functional study on cage and noncage (fe2o3) n clusters, The Journal of Chemical Physics 130 (1).

[34] D. Wei, W. Ma, X. Wu, L. Cheng, A modified dynamic lattice searching method for structural optimization of metal oxide clusters, Chemical Physics 543 (2021) 111097.

[35] R. Mejia-Olvera, J. Reveles, S. Pacheco-Ortín, J. Santoyo-Salazar, Molecular dynamics and electronic structure study of neutral, cationic and anionic (fe3o4) 1–5 clusters, Chemical Physics Letters 706 (2018) 494–500.

[36] D. A. Hansgen, D. G. Vlachos, J. G. Chen, Using first principles to predict bimetallic catalysts for the ammonia decomposition reaction, Nature chemistry 2 (6) (2010) 484–489.

[37] C. Plana, S. Armenise, A. Monzón, E. García-Bordejé, Ni on alumina-coated cordierite monoliths for in situ generation of co-free h_2 from ammonia, Journal of Catalysis 275 (2) (2010) 228–235.

[38] H. Liu, H. Wang, J. Shen, Y. Sun, Z. Liu, Promotion effect of cerium and lanthanum oxides on ni/sba-15 catalyst for ammonia decomposition, Catalysis today 131 (1-4) (2008) 444–449.

[39] R. Lan, J. T. Irvine, S. Tao, Ammonia and related chemicals as potential indirect hydrogen storage materials, International journal of hydrogen energy 37 (2) (2012) 1482–1494.

[40] A. Klerke, C. H. Christensen, J. K. Nørskov, T. Vegge, Ammonia for hydrogen storage: challenges and opportunities, Journal of Materials Chemistry 18 (20) (2008) 2304–2310.

[41] J. C. Ganley, F. Thomas, E. Seebauer, R. I. Masel, A priori catalytic activity correlations: the difficult case of hydrogen production from ammonia, Catalysis Letters 96 (2004) 117–122.

[42] S.-F. Yin, Q.-H. Zhang, B.-Q. Xu, W.-X. Zhu, C.-F. Ng, C.-T. Au, Investigation on the catalysis of cox-free hydrogen generation from ammonia, Journal of Catalysis 224 (2) (2004) 384–396.

[43] Á. Logadóttir, J. K. Nørskov, Ammonia synthesis over a ru (0001) surface studied by density functional calculations, Journal of Catalysis 220 (2) (2003) 273–279.

[44] I. Lucentini, X. Garcia, X. Vendrell, J. Llorca, Review of the decomposition of ammonia to generate hydrogen, Industrial & Engineering Chemistry Research 60 (51) (2021) 18560–18611.

[45] L. Yao, T. Shi, Y. Li, J. Zhao, W. Ji, C.-T. Au, Core–shell structured nickel and ruthenium nanoparticles: Very active and stable catalysts for the generation of cox-free hydrogen via ammonia decomposition, Catalysis Today 164 (1) (2011) 112–118.

[46] K. Zemski, D. Justes, A. Castleman, Studies of metal oxide clusters: Elucidating reactive sites responsible for the activity of transition metal oxide catalysts, The Journal of Physical Chemistry B 106 (24) (2002) 6136–6148.

[47] D. Yang, M. Babucci, W. H. Casey, B. C. Gates, The surface chemistry of metal oxide clusters: From metal–organic frameworks to minerals, ACS central science 6 (9) (2020) 1523–1533.

[48] E. C. Tyo, S. Vajda, Catalysis by clusters with precise numbers of atoms, Nature nanotechnology 10 (7) (2015) 577–588.

[49] U. Heiz, U. Landman, Nanocatalysis, Springer Science & Business Media, 2007.

[50] A. Fernando, K. D. M. Weerawardene, N. V. Karimova, C. M. Aikens, Quantum mechanical studies of large metal, metal oxide, and metal chalcogenide nanoparticles and clusters, Chemical reviews 115 (12) (2015) 6112–6216.

[51] K. Nishimaki, S. Ohmae, T. Yamamoto, M. Katsura, Formation of iron-nitrides by the reaction of iron nanoparticles with a stream of ammonia, Nanostructured Materials 12 (1-4) (1999) 527–530.

[52] G. Lanzani, K. Laasonen, Nh_3 adsorption and dissociation on a nanosized iron cluster, International journal of hydrogen energy 35 (13) (2010) 6571–6577.

[53] G. S. Otero, B. Pascucci, M. M. Branda, R. Miotto, P. G. Belelli, Evaluating the size of fe nanoparticles for ammonia adsorption and dehydrogenation, Computational Materials Science 124 (2016) 220–227.

[54] X. Zhang, Z. Lu, D. Ma, Z. Yang, Adsorption and dissociation of ammonia on small iron clusters, international journal of hydrogen energy 40 (1) (2015) 346–352.

[55] J. Zhang, H. Xu, X. Jin, Q. Ge, W. Li, Characterizations and activities of the nano-sized ni/al$_2$o$_3$ and ni/la–al$_2$o$_3$ catalysts for nh3 decomposition, Applied Catalysis A: General 290 (1-2) (2005) 87–96.

[56] A. M. Karim, V. Prasad, G. Mpourmpakis, W. W. Lonergan, A. I. Frenkel, J. G. Chen, D. G. Vlachos, Correlating particle size and shape of supported ru/γ-al2o3 catalysts with nh3 decomposition activity, Journal of the American Chemical Society 131 (34) (2009) 12230–12239.

[57] J. Ji, X. Duan, G. Qian, P. Li, X. Zhou, D. Chen, W. Yuan, Fe particles on the tops of carbon nanofibers immobilized on structured carbon microfibers for ammonia decomposition, Catalysis today 216 (2013) 254–260.

[58] J. Zhang, M. Comotti, F. Schüth, R. Schlögl, D. S. Su, Commercial fe-or co-containing carbon nanotubes as catalysts for nh3 decomposition, Chemical communications (19) (2007) 1916–1918.

[59] D. Xuezhi, Z. Jinghong, Q. Gang, L. Ping, Z. Xinggui, C. De, Carbon nanofiber-supported ru catalysts for hydrogen evolution by ammonia decomposition, Chinese Journal of Catalysis 31 (8) (2010) 979–986.

[60] Q. Yang, X.-P. Fu, C.-J. Jia, C. Ma, X. Wang, J. Zeng, R. Si, Y.-W. Zhang, C.-H. Yan, Structural determination of catalytically active subnanometer iron oxide clusters, ACS Catalysis 6 (5) (2016) 3072–3082.

[61] N. Iordanova, M. Dupuis, K. M. Rosso, Charge transport in metal oxides: A theoretical study of hematite α-fe2o3, The Journal of chemical physics 122 (14).

[62] M. Sánchez, L. Sabio, N. Gálvez, M. Capdevila, J. M. Dominguez-Vera, Iron chemistry at the service of life, IUBMB life 69 (6) (2017) 382–388.

[63] L. Machala, J. Tucek, R. Zboril, Polymorphous transformations of nanometric iron (iii) oxide: a review, Chemistry of materials 23 (14) (2011) 3255–3272.

[64] Y. Feng, J. Wei, Y. Ding, Efficient photochemical, thermal, and electrochemical water oxidation catalyzed by a porous iron-based oxide derived metal–organic framework, The Journal of Physical Chemistry C 120 (1) (2016) 517–526.

[65] Q. Shi, Y. Zhou, J. Cheng, Y. Pan, Y. Wu, L. Zhu, Z. Yuan, Turning carbon black into hollow carbon nanospheres to encapsulate fe2o3 as high-performance lithium-ion batteries anode, Microporous and Mesoporous Materials 332 (2022) 111681.

[66] H. Zhao, M. Jiang, Q. Kang, L. Liu, N. Zhang, P. Wang, F. Zhou, Electrocatalytic oxygen and hydrogen evolution reactions at ni3b/fe2o3 nanotube arrays under visible light radiation, Catalysis Science and Technology 10 (24) (2020) 8305–8313.

[67] S. Maeda, T. Taketsugu, K. Morokuma, Exploring transition state structures for intramolecular pathways by the artificial force induced reaction method, Journal of computational chemistry 35 (2) (2014) 166–173.

[68] W. Sameera, A. Kumar Sharma, S. Maeda, K. Morokuma, Artificial force induced reaction method for systematic determination of complex reaction mechanisms, The Chemical Record 16 (5) (2016) 2349–2363.

[69] A. Szabo, N. S. Ostlund, Modern Quantum Chemistry: Introduction to Advanced Electronic Structure Theory, Dover Publications, 1989.

[70] T. Helgaker, P. Jørgensen, J. Olsen, Molecular Electronic-Structure Theory, Wiley, 2000.

[71] C. C. J. Roothaan, New developments in molecular orbital theory, Rev. Mod. Phys. 23 (1951) 69–89.

[72] G. G. Hall, The molecular orbital theory of chemical valency. VIII. A method of calculating ionization potentials, Proc. R. Soc. London A 205 (1951) 541–552.

[73] F. Jensen, Introduction to Computational Chemistry, 3rd Edition, Wiley, 2017.

[74] C. A. Coulson, I. Fischer, Notes on the molecular orbital treatment of the hydrogen molecule, Philos. Mag. 40 (1949) 386–393.

[75] P.-O. Löwdin, Quantum theory of many-particle systems. I. physical interpretations by means of density matrices, natural spin-orbitals, and convergence problems in the method of configurational interaction, Phys. Rev. 97 (1955) 1474–1489.

[76] J. A. Pople, R. K. Nesbet, Self-consistent orbitals for radicals, J. Chem. Phys. 22 (1954) 571–572.

[77] P. J. Knowles, J. S. Andrews, R. D. Amos, N. C. Handy, J. A. Pople, Restricted Møller-Plesset theory for open-shell molecules, Chem. Phys. Lett. 186 (1993) 130–136.

[78] H. B. Schlegel, Potential energy curves using unrestricted Møller–Plesset perturbation theory with spin annihilation, J. Chem. Phys. 84 (1986) 4530–4534.

[79] C. C. J. Roothaan, Self-consistent field theory for open shells of electronic systems, Rev. Mod. Phys. 32 (1960) 179–185.

[80] H.-J. Werner, P. J. Knowles, A second order multiconfiguration SCF procedure with optimum convergence, J. Chem. Phys. 82 (1985) 5053–5063.

[81] P. E. M. Siegbahn, J. Almlöf, A. Heiberg, B. O. Roos, The complete active space SCF (CASSCF) method in a newton-Raphson formulation with application to the HNO molecule, J. Chem. Phys. 74 (1981) 2384–2396.

[82] W. Koch, M. C. Holthausen, A Chemist's Guide to Density Functional Theory, Wiley-VCH, 1999.

[83] J. N. Harvey, On the accuracy of density functional theory in transition metal chemistry, Annu. Rep. Prog. Chem., Sect. C 102 (2006) 203–226.

[84] U. Ryde, P. Soderhjelm, Ligand-binding affinity estimates supported by quantum-mechanical methods, Chem. Rev. 116 (2016) 5520–5566.

[85] F. Neese, Importance of direct spin-spin coupling and spin-flip excitations for the zero-field splittings of transition metal complexes: A case study, J. Am. Chem. Soc. 128 (2006) 10213–10222.

[86] B. O. Roos, P. R. Taylor, P. E. Sigbahn, A complete active space scf method (casscf) using a density matrix formulated super-ci approach, Chemical Physics 48 (2) (1980) 157–173.

[87] L. Cheung, K. Sundberg, K. Ruedenberg, Dimerization of carbene to ethylene, Journal of the American Chemical Society 100 (25) (1978) 8024–8025.

[88] K. Ruedenberg, M. W. Schmidt, M. M. Gilbert, S. Elbert, Are atoms intrinsic to molecular electronic wavefunctions? i. the fors model, Chemical Physics 71 (1) (1982) 41–49.

[89] J. S. Sears, C. David Sherrill*, On the choice of reference in multi-reference electronic structure theory: minimal references for bond breaking, Molecular Physics 103 (6-8) (2005) 803–814.

[90] M. J. Bearpark, F. Bernardi, S. Clifford, M. Olivucci, M. A. Robb, B. R. Smith, T. Vreven, The azulene s1 state decays via a conical intersection: a casscf study with mmvb dynamics, Journal of the American Chemical Society 118 (1) (1996) 169–175.

[91] M. Boggio-Pasqua, M. A. Robb, M. J. Bearpark, Photostability via a sloped conical intersection: A casscf and rasscf study of pyracylene, The Journal of Physical Chemistry A 109 (39) (2005) 8849–8856.

[92] M.-D. Su, Cascsf study on the photochemical transposition reactions of pyrazines, The Journal of Physical Chemistry A 110 (30) (2006) 9420–9428.

[93] M. Bearpark, M. Robb, N. Yamamoto, A casscf study of the cyclopentadienyl radical: conical intersections and the jahn–teller effect, Spectrochimica Acta Part A: Molecular and Biomolecular Spectroscopy 55 (3) (1999) 639–646.

[94] L. Serrano-Andrés, M. Merchán, R. Lindh, Computation of conical intersections by using perturbation techniques, The Journal of chemical physics 122 (10).

[95] Y. Haas, Conical intersections leading to chemical reactions in the gas and liquid phases, Advances in Chemistry 2014 (1) (2014) 419102.

[96] K. Pierloot, B. J. Persson, B. O. Roos, Theoretical study of the chemical bonding in [ni (c2h4)] and ferrocene, The Journal of Physical Chemistry 99 (11) (1995) 3465–3472.

[97] K. Shamasundar, G. Knizia, H.-J. Werner, A new internally contracted multi-reference configuration interaction method, The Journal of chemical physics 135 (5).

[98] E. R. Sayfutyarova, Q. Sun, G. K.-L. Chan, G. Knizia, Automated construction of molecular active spaces from atomic valence orbitals, Journal of chemical theory and computation 13 (9) (2017) 4063–4078.

[99] C. J. Stein, M. Reiher, Automated selection of active orbital spaces, Journal of chemical theory and computation 12 (4) (2016) 1760–1771.

[100] P. G. Szalay, T. Muller, G. Gidofalvi, H. Lischka, R. Shepard, Multiconfiguration self-consistent field and multireference configuration interaction methods and applications, Chemical reviews 112 (1) (2012) 108–181.

[101] C. Møller, M. S. Plesset, Note on an approximation treatment for many-electron systems, Physical review 46 (7) (1934) 618.

[102] J. M. Herbert, M. Head-Gordon, Accuracy and limitations of second-order many-body perturbation theory for predicting vertical detachment energies of solvated-electron clusters, Physical Chemistry Chemical Physics 8 (1) (2006) 68–78.

[103] C. D. Sherrill, T. Takatani, E. G. Hohenstein, An assessment of theoretical methods for nonbonded interactions: Comparison to complete basis set limit coupled-cluster potential energy curves for the benzene dimer, the methane dimer, benzene- methane, and benzene- h2s, The Journal of Physical Chemistry A 113 (38) (2009) 10146–10159.

[104] A. Varandas, Spin-component-scaling second-order møller–plesset theory and its variants for economical correlation energies: unified theoretical interpretation and use for quartet n3, The Journal of chemical physics 133 (6).

[105] W. Kohn, Density functional theory, Introductory quantum mechanics with MATLAB: for atoms, molecules, clusters, and nanocrystals.

[106] R. O. Jones, Density functional theory: Its origins, rise to prominence, and future, Reviews of modern physics 87 (3) (2015) 897–923.

[107] A. J. Cohen, P. Mori-Sánchez, W. Yang, Insights into current limitations of density functional theory, Science 321 (5890) (2008) 792–794.

[108] S. Grimme, J. Antony, S. Ehrlich, H. Krieg, A consistent and accurate ab initio parametrization of density functional dispersion correction (dft-d) for the 94 elements h-pu, The Journal of chemical physics 132 (15).

[109] S. Huzinaga, Gaussian-type functions for polyatomic systems. i, The Journal of chemical physics 42 (4) (1965) 1293–1302.

[110] H. Partridge, Near hartree–fock quality gto basis sets for the first-and third-row atoms, The Journal of chemical physics 90 (2) (1989) 1043–1047.

[111] T. H. Dunning Jr, Gaussian basis functions for use in molecular calculations. iii. contraction of (10s6p) atomic basis sets for the first-row atoms, The Journal of Chemical Physics 55 (2) (1971) 716–723.

[112] F. Weigend, F. Furche, R. Ahlrichs, Gaussian basis sets of quadruple zeta valence quality for atoms h–kr, The Journal of chemical physics 119 (24) (2003) 12753–12762.

[113] F. Weigend, R. Ahlrichs, Balanced basis sets of split valence, triple zeta valence and quadruple zeta valence quality for h to rn: Design and assessment of accuracy, Physical Chemistry Chemical Physics 7 (18) (2005) 3297–3305.

[114] J. Almlöf, P. R. Taylor, Atomic natural orbital (ano) basis sets for quantum chemical calculations, in: Advances in Quantum Chemistry, Vol. 22, Elsevier, 1991, pp. 301–373.

[115] T. H. Dunning Jr, K. A. Peterson, A. K. Wilson, Gaussian basis sets for use in correlated molecular calculations. x. the atoms aluminum through argon revisited, The Journal of Chemical Physics 114 (21) (2001) 9244–9253.

[116] R. A. Kendall, T. H. Dunning Jr, R. J. Harrison, Electron affinities of the first-row atoms revisited. systematic basis sets and wave functions, The Journal of chemical physics 96 (9) (1992) 6796–6806.

[117] F. Jensen, Polarization consistent basis sets: Principles, The Journal of Chemical Physics 115 (20) (2001) 9113–9125.

[118] P. J. Hay, W. R. Wadt, Ab initio effective core potentials for molecular calculations. potentials for the transition metal atoms sc to hg, The Journal of chemical physics 82 (1) (1985) 270–283.

[119] W. R. Wadt, P. J. Hay, Ab initio effective core potentials for molecular calculations. potentials for main group elements na to bi, The Journal of chemical physics 82 (1) (1985) 284–298.

[120] P. J. Hay, W. R. Wadt, Ab initio effective core potentials for molecular calculations. potentials for k to au including the outermost core orbitals, The Journal of chemical physics 82 (1) (1985) 299–310.

[121] S. Maeda, K. Morokuma, Communications: A systematic method for locating transition structures of a+ b→ x type reactions, The Journal of chemical physics 132 (24).

[122] S. Maeda, K. Morokuma, Finding reaction pathways of type a+ b→ x: Toward systematic prediction of reaction mechanisms, Journal of Chemical Theory and Computation 7 (8) (2011) 2335–2345.

[123] S. Maeda, K. Ohno, K. Morokuma, Systematic exploration of the mechanism of chemical reactions: the global reaction route mapping (grrm) strategy using the addf and afir methods, Physical Chemistry Chemical Physics 15 (11) (2013) 3683–3701.

[124] S. Maeda, Y. Harabuchi, M. Takagi, K. Saita, K. Suzuki, T. Ichino, Y. Sumiya, K. Sugiyama, Y. Ono, Implementation and performance of the artificial force induced reaction method in the grrm17 program (2018).

[125] W. Sameera, S. Maeda, K. Morokuma, Computational catalysis using the artificial force induced reaction method, Accounts of Chemical Research 49 (4) (2016) 763–773.

[126] S. Trasatti, The absolute electrode potential: an explanatory note (recommendations 1986), Pure and Applied Chemistry 58 (7) (1986) 955–966.

[127] J. Tomasi, B. Mennucci, R. Cammi, Quantum mechanical continuum solvation models, Chemical reviews 105 (8) (2005) 2999–3094.

[128] C. J. Cramer, D. G. Truhlar, et al., Implicit solvation models: equilibria, structure, spectra, and dynamics, Chemical Reviews 99 (1999) 2161–2200.

[129] M. Orozco, F. J. Luque, Theoretical methods for the description of the solvent effect in biomolecular systems, Chemical Reviews 100 (11) (2000) 4187–4226.

[130] C. J. Cramer, D. G. Truhlar, A universal approach to solvation modeling, Accounts of chemical research 41 (6) (2008) 760–768.

[131] A. Klamt, G. Schüürmann, Cosmo: a new approach to dielectric screening in solvents with explicit expressions for the screening energy and its gradient, Journal of the Chemical Society, Perkin Transactions 2 (5) (1993) 799–805.

[132] K. Pradhan, G. L. Gutsev, C. A. Weatherford, P. Jena, A systematic study of neutral and charged 3d-metal trioxides and tetraoxides, The Journal of chemical physics 134 (14).

[133] S. Ibragimov, L. Komando, M. Bobrowski, Isomers of iron (iii) oxides and cobalt (iii) oxides and their redox properties: Quantum-chemical insights, Molecules 30 (21) (2025) 4158.

[134] J. A. Thompson, R. Gonzalez-Cabaleiro, L. Vila-Nadal, Reducing systematic uncertainty in computed redox potentials for aqueous transition-metal-substituted polyoxotungstates, Inorganic chemistry 62 (31) (2023) 12260–12271.

[135] I. Ahamed, N. Seriani, R. Gebauer, A. Kashya, Heterostructures of ϵ-fe_2o_3 and α-fe_2o_3: insights from density functional theory, RSC Adv. 10 (46). doi:10.1039/d0ra04020g.

[136] G. Gutsev, K. Bozhenko, L. Gutsev, A. Utenyshev, S. Aldoshin, Dependence of properties and exchange coupling constants on the charge in the mn2o n and fe2o n series, The Journal of Physical Chemistry A 122 (25) (2018) 5644–5655.

[137] N. M. Reilly, J. U. Reveles, G. E. Johnson, J. M. del Campo, S. N. Khanna, A. M. Köster, A. Castleman, Experimental and theoretical study of the structure and reactivity of fe m o n+(m= 1, 2; n= 1- 5) with co, The Journal of Physical Chemistry C 111 (51) (2007) 19086–19097.

[138] H. Wu, S. R. Desai, L.-S. Wang, Observation and photoelectron spectroscopic study of novel mono-and diiron oxide molecules: Feo y-(y= 1- 4) and fe2o y-(y= 1- 5), Journal of the American Chemical Society 118 (22) (1996) 5296–5301.

[139] G. E. Johnson, J. U. Reveles, N. M. Reilly, E. C. Tyo, S. N. Khanna, A. Castleman Jr, Influence of stoichiometry and charge state on the structure and reactivity of cobalt oxide clusters with co, The Journal of Physical Chemistry A 112 (45) (2008) 11330–11340.

[140] G. Boschloo, A. Hagfeldt, Characteristics of the iodide/triiodide redox mediator in dye-sensitized solar cells, Accounts of chemical research 42 (11) (2009) 1819–1826.

[141] B. C. Faust, M. R. Hoffmann, D. W. Bahnemann, Photocatalytic oxidation of sulfur dioxide in aqueous suspensions of. alpha.-iron oxide (fe2o3), The Journal of Physical Chemistry 93 (17) (1989) 6371–6381.

[142] C. Kormann, D. W. Bahnemann, M. R. Hoffmann, Environmental photochemistry: Is iron oxide (hematite) an active photocatalyst? a comparative study: α-fe2o3, zno, tio2, Journal of Photochemistry and Photobiology A: Chemistry 48 (1) (1989) 161–169.

[143] C. Marius, I. Grozescu, Fe_2O_3 - Nanoparticles, Physical Properties and Their Photochemical and Photoelectrochemical Applications, POLITEHNICA Univ. (Timişoara) Volume 54 (2009) 1–8.

[144] D. Gobrecht, J. P. Sindel, H. Lecoq-Molinos, L. Decin, The ionization energies of dust-forming metal oxide clusters, Universe 7 (7) (2021) 243.

[145] S. Sahoo, G. Rollmann, P. Entel, First-principles calculation of cluster geometries and magnetization of pure ni and fe–ni clusters, Phase Transitions 78 (9-11) (2005) 723–731.

[146] P. Nava, M. Sierka, R. Ahlrichs, Density functional study of palladium clusters, Physical Chemistry Chemical Physics 5 (16) (2003) 3372–3381.

[147] J. Li, X. Li, H.-J. Zhai, L.-S. Wang, Au20: a tetrahedral cluster, Science 299 (5608) (2003) 864–867.

[148] J. F. Parker, K. A. Kacprzak, O. Lopez-Acevedo, H. Hakkinen, R. W. Murray, Experimental and density functional theory analysis of serial introductions of electron-withdrawing ligands into the ligand shell of a thiolate-protected au25 nanoparticle, The Journal of Physical Chemistry C 114 (18) (2010) 8276–8281.

[149] S. Li, D. A. Dixon, Molecular structures and energetics of the (zro2) n and (hfo2) n (n= 1- 4) clusters and their anions, The Journal of Physical Chemistry A 114 (7) (2010) 2665–2683.

[150] S. Nayak, P. Jena, Equilibrium geometry, stability, and magnetic properties of small mno clusters, Journal of the American Chemical Society 121 (4) (1999) 644–652.

[151] F. Jensen, Introduction to computational chemistry, John wiley & sons, 2017.

[152] A. B. Rahane, P. A. Murkute, M. D. Deshpande, V. Kumar, Density functional calculations of the structural and electronic properties of (y2o3) n 0,±1 clusters with n= 1–10, The Journal of Physical Chemistry A 117 (26) (2013) 5542–5550.

[153] U. Kurien, Z. Hu, H. Lee, A. P. Dastoor, P. A. Ariya, Radiation enhanced uptake of hg 0 (g) on iron (oxyhydr) oxide nanoparticles, RSC advances 7 (71) (2017) 45010–45021.

[154] S. Ibragimov, A. Lyalin, S. Kumar, Y. Ono, T. Taketsugu, M. Bobrowski, Theoretical design of nanocatalysts based on (fe2o3) n clusters for hydrogen production from ammonia, The Journal of Chemical Physics 162 (5).

[155] A. Hellman, K. Honkala, I. Remediakis, A. Logadottir, A. Carlsson, S. Dahl, C. H. Christensen, J. K. Nørskov, Ammonia synthesis and decomposition on a ru-based catalyst modeled by first-principles, Surface Science 603 (10-12) (2009) 1731–1739.

[156] H. Shiroishi, T. Oda, I. Hamada, N. Fujima, Structure and magnetism on iron oxide clusters fenom (n= 1-5): calculation from first principles, The European Physical Journal D-Atomic, Molecular, Optical and Plasma Physics 24 (2003) 85–88.

[157] N. Jones, B. Reddy, F. Rasouli, S. N. Khanna, Structural growth in iron oxide clusters: Rings, towers, and hollow drums, Physical Review B 72 (16) (2005) 165411.

[158] A. Erlebach, C. Hühn, R. Jana, M. Sierka, Structure and magnetic properties of (fe2o3)n clusters (n= 1–5), Physical Chemistry Chemical Physics 16 (48) (2014) 26421–26426.

[159] Y. Zhao, D. G. Truhlar, The m06 suite of density functionals for main group thermochemistry, thermochemical kinetics, noncovalent interactions, excited states, and transition elements: two new functionals and systematic testing of four m06-class functionals and 12 other functionals, Theoretical chemistry accounts 120 (2008) 215–241.

[160] N. Mardirossian, M. Head-Gordon, ωb97x-v: A 10-parameter, range-separated hybrid, generalized gradient approximation density functional with nonlocal correlation, designed by a survival-of-the-fittest strategy, Physical Chemistry Chemical Physics 16 (21) (2014) 9904–9924.

[161] S. Zhou, S. Lin, H. Guo, First-principles insights into ammonia decomposition catalyzed by ru clusters anchored on carbon nanotubes: size dependence and interfacial effects, The Journal of Physical Chemistry C 122 (16) (2018) 9091–9100.

[162] C. Zhang, M. Lynch, P. Hu, A density functional theory study of stepwise addition reactions in ammonia synthesis on ru (0001), Surface science 496 (3) (2002) 221–230.

[163] W. Huang, L. Wang, L. Dong, H. Hu, D. Ren, Density functional study on adsorption of nh3 and nox on the γ-fe2o3 (111) surface, Molecules 28 (5) (2023) 2371.

[164] C.-y. Zou, W. Ji, Z. Shen, Q. Tang, M. Fan, Nh3 molecule adsorption on spinel-type znfe2o4 surface: A dft and experimental comparison study, Applied Surface Science 442 (2018) 778–786.

[165] C. Xie, Y. Sun, B. Zhu, W. Song, M. Xu, Adsorption mechanism of nh3, no, and o2 molecules over the fexoy/ac catalyst surface: a dft-d3 study, New Journal of Chemistry 45 (6) (2021) 3169–3180.

[166] D. Ren, K. Gui, Study of the adsorption of nh3 and nox on the nano-γfe2o3 (001) surface with density functional theory, Applied Surface Science 487 (2019) 171–179.

[167] M. Gao, A. Lyalin, S. Maeda, T. Taketsugu, Application of automated reaction path search methods to a systematic search of single-bond activation pathways catalyzed by small metal clusters: A case study on h–h activation by gold, Journal of Chemical Theory and Computation 10 (4) (2014) 1623–1630.

[168] E. Erdtman, M. Andersson, A. L. Spetz, L. Ojamäe, Simulations of the thermodynamics and kinetics of nh3 at the ruo2 (110) surface, Surface Science 656 (2017) 77–85.